DISSERTATION

THEORETICAL AND EXPERIMENTAL INVESTIGATIONS IN PLANETARY DUST ADHESION

Submitted by

Howard A. Perko

Department of Civil Engineering

In partial fulfillment of the requirements

for the Degree of Doctor of Philosophy

Colorado State University

Fort Collins, Colorado

Spring 2002

UMI Number: 3053440

ProQuest Information and Learning Company
300 North Zeeb Road
P.O. Box 1346
Ann Arbor, MI 48106-1346

COLORADO STATE UNIVERSITY

March 29, 2002

We hereby recommend that the dissertation prepared under our supervision by Howard A. Perko entitled *Theoretical and Experimental Investigations in Planetary Dust Adhesion* be accepted as fulfilling in part the requirements for the degree of Doctor of Philosophy.

Committee on Graduate Work

Dr. Mark Bradley, Physics Dept., Committee Member

Dr. Marvin Criswell, Civil Eng. Dept., Committee Member

Dr. Jacklyn R. Green, JPL, Affiliate Co-Advisor

Dr. John D. Nelson, Civil Eng. Dept., Advisor

Dr. Sandra Woods, Department Head

ABSTRACT OF DISSERTATION

THEORETICAL AND EXPERIMENTAL INVESTIGATIONS IN PLANETARY DUST ADHESION

An investigation was conducted to evaluate the effect of different planetary environmental conditions on mineral dust adhesion. In planetary exploration, dust contamination affects radiator, solar cell, optical lens, and mirror performance. An improved understanding of the fundamental mechanisms by which surfaces attract dust is important for the development of dust mitigation techniques that will increase the duration and success of future planetary science exploration initiatives. Dust mechanics and adhesion research also has applications in semiconductor, xerography, paint, air-pollution, pesticide, sand paper, oil recovery, and pharmaceutical manufacturing industries.

Since Mars and comet exploration is on the forefront of current NASA mission planning, a review of Martian and cometary dust properties is presented. The present state of knowledge regarding dust adhesion is summarized. A model for determining dust adhesion is derived that incorporates capillary, van der Waals, and electrostatic forces. The model accounts for elastic particle deformation and the potential of an adsorbed layer of gas separating the particles. Dust adhesion was measured in laboratory using a vibrating

cantilever beam apparatus under different environmental conditions. Results from the experiments, as well as laboratory measurements previously taken by others, match model predictions relatively well. The model is extended to predict dust adhesion on Mars and comets.

Howard A. Perko
Civil Engineering Department
Colorado State University
Fort Collins, CO 80523
Spring 2002

ACKNOWLEDGMENTS

The advice and suggestions offered by Dr. John Nelson during this research are appreciated. His assistance was invaluable, especially in the design of the experiment and during critical points in the development of the theoretical model. His encouragement kept the project focused on the primary objectives and on schedule. I also appreciate that despite serious health concerns that arose during the preparation of this work, Dr. Nelson's support as the primary advisor was unfailing.

The friendship and counseling offered by Dr. Jacklyn Green, "Jackie", of the Jet Propulsion Laboratory during the project are appreciated. Funding for the project likely would not have been obtained without her assistance with the preparation of the NASA GSRP fellowship proposal. I will always be grateful to her and her husband Roger for making available the 2nd floor apartment above their house in California and to her for allowing me the opportunity to work in her laboratory at JPL. I also appreciate her nurture of my planetary science interests and for teaching an engineer to become a better experimental scientist.

Dr. Marvin Criswell and Dr. Mark Bradley are appreciated for serving as committee members. In our meetings, they produced ideas and constructive criticism that significantly added to the project. Dr. Criswell's support through the NASA Space Grant, during the

incubator period prior to the project, is gratefully acknowledged. Dr. Bradley's level headed approach kept me from straying into areas that were beyond my skill level.

The Jet Propulsion Laboratory (JPL) is recognized and appreciated for providing access to facilities, equipment, and personnel during the program. Some of the outstanding personnel that assisted me while at JPL include Dr. Martin Buehler, Dr. Steve Fuerstenau, Lindsey Bruche, Ryan Oaks, and Greg Peters. Finally, support for this research project by the NASA Graduate Student Research Program is acknowledged.

TABLE OF CONTENTS

TABLE OF CONTENTS (CONT.)

LIST OF FIGURES

LIST OF FIGURES (CONT.)

LIST OF FIGURES (CONT.)

LIST OF TABLES

NOMENCLATURE

a	elastic contact radius
a_o	initial equilibrium contact radius
a_f	final contact radius at separation
B	capillary parabola height
c_{SC}	surface cleanliness cohesion
d	distance between points or surfaces
D	amplitude of vibrations
e	fundamental unit of charge
E	Young Modulus
E^*	effective elasticity
F	external force on a particle
F_c	capillary force
F_{VDW}	van der Waals force
F_{ELEC}	electrostatic force
F_a	adhesion force
F_l	removal force plus adhesion force
F_0	applied removal force
F_{cmp}	total compressive stress
G	free energy
G_{AB}	Lewis-acid Lewis-base energy
h	capillary parabola dimension
j	position of dust removal front
K	elastic mismatch parameter
l	length of vibrating beam
L	capillary parabola width
m	mass of particle
P	pressure
P_o	saturation vapor pressure of gas
P_g	partial pressure of ambient gas
p_m	mean mechanical contact pressure
Q_n	net charge of particle n
r_m	mean radius of curvature
r_c	major azimuthal capillary radius
r_s	minor capillary radius
R	Ideal Gas Constant
R_n	radius of particle n

NOMENCLATURE (CONT.)

R^*	mean particle radius
S	surface cleanliness parameter
s_n	surface charge density of particle n
T	temperature
t	adsorbate thickness
U_T	total energy of system
U_{VDW}	van der Waals energy
U_{ELEC}	Coulomb electrostatic energy
U_c	capillary energy
U_I	electrostatic image energy
U_M	mechanical work
U_e	stored elastic energy
U_a	adhesion energy
u_z	vertical displacement of solid surface
u_{zh}	Hertz surface displacement
u_{zp}	cylindrical punch displacement
V	volume of liquid pendular ring
V_{SP}	volume of solid particle within ring
V_n	voltage amplitude measurement for beam n
v	velocity of particle relative to surface
X	compressive and tensile transition
x	capillary radial dimension
z	vertical dimension
z_o	minimum distance between surfaces
z_h	surface asperity height
α	removal force ratio
α_o	initial equilibrium force ratio
α_f	final removal force ratio
α_ω	particle acceleration
α_p	molecular polarizability
γ^+	surface energy of Lewis-acid
γ^-	surface energy of Lewis-base
γ_{LV}	liquid-vapor surface energy
γ_{SV}	solid-vapor surface energy
γ_{SL}	solid-liquid surface energy
δ	distance of approach of surfaces

NOMENCLATURE (CONT.)

δ_o	distance of approach at equilibrium
δ_f	distance of approach at removal
ϵ	relative dielectric permittivity
ϵ_o	dielectric permittivity of free space
ζ	surface cleanliness energy parameter
η	number of particle contacts per area
θ	liquid-solid contact angle
λ	differential cylinder diameter
μ_n	chemical potential of medium n
μ_T	Tabor Parameter
ν	Poisson Ratio
π_{eSV}	solid-vapor disjoining pressure
π_{eLV}	liquid-vapor disjoining pressure
ρ	radial dimension
ρ_m	molecular density
ρ_e	electrostatic charge density
σ_y	plastic yield strength
σ_h	standard deviation of asperities
σ_{zh}	Hertz contact stress
σ_{zp}	cylindrical punch contact stress
σ_{zt}	total contact stress of superposition
ς_n	surface cleanliness coefficients
ϕ_{SC}	surface cleanliness angle of friction
Ψ	surface asperity height distribution
Ω	diameter of oxygen ion
ω	cyclic frequency of vibrations

Vast is the kingdom of dust! Unlike terrestrial kingdoms, it knows no limits. No ocean marks its boundaries. No mountains hem it in. No parallels of latitude and longitude define its boundless areas, nor can the farthermost stars in the infinitudes of space serve other than as a twinkling outpost of a realm as vast as the universe itself.

-J. Gordon Ogden, *The Kingdom of Dust*

1.0 INTRODUCTION

The broad subject of this dissertation is adhesion, the force between surfaces and particles. Adhesion is an important component in the general study of surface lubrication and tribology. The general goal of this investigation is to better understand the fundamental mechanisms of mineral dust adhesion, so that better predictions regarding dust and soil behavior in different planetary environments can be made. Particular emphasis was placed on the effect of planetary environmental conditions including temperature, pressure, humidity, and ambient gas composition.

In comet, asteroid, and planetary near-surface and surface exploration, understanding the effect of dust on spacecraft, lander, and rover performance is an important part of mission design. Dust particles can accumulate on surfaces causing obscuration of lenses and mirrors, decreased solar panel efficiency, and altered thermal radiator efficiency. Dust particles can clog filters, abrade mechanical equipment, and damage electronics. An understanding of the

mechanism by which surfaces attract dust will aid in developing mitigation techniques that increase the duration and success of future planetary science exploration initiatives.

Dust mechanics and adhesion research also has applications in semiconductor, xerography, paint, air-pollution, pesticide, sand paper, tertiary oil recovery, and pharmaceutical manufacturing industries. There is a trend toward nano-technologies in mechanical and electrical systems engineering. As the scale of devices decreases, the importance of dust increases. Dust contamination affects the reliability of magnetic storage devices (Cooper, Wolfe, and Miller, 1988) and the performance of optical devices.

1.1 Classification and Transport

In the field of planetary science, particles with diameters smaller than about 100 μm are generally termed dust. The size range for typical dust particles is given in Table 1.1. The wavelength of electromagnetic radiation, soil gradation based on the Unified Soil Classification System, and size of common atmospheric dispersoids are provided for comparison. Ordinary gravitational settling rate for spherical dust particles in Earth-like conditions are shown at the bottom of the table. Settling rates are based on a dust grain specific gravity of 2.0, which is typical for glass. The settling rates shown should be multiplied by a factor of 1.7 for dust grains with a specific gravity of 2.7, which is approximately representative of olivine, quartz, and many philosilicates.

There are several modes of transport that cause a dust particle to be deposited on a surface including a.) diffusion, b.) sedimentation, c.) impact, d.) turbulent eddying, and e.) electromagnetic attraction. Diffusion affects transport of particles with diameters less than

Table 1.1 Dust Particle Characteristics (adapted from Mitchell, 1993)

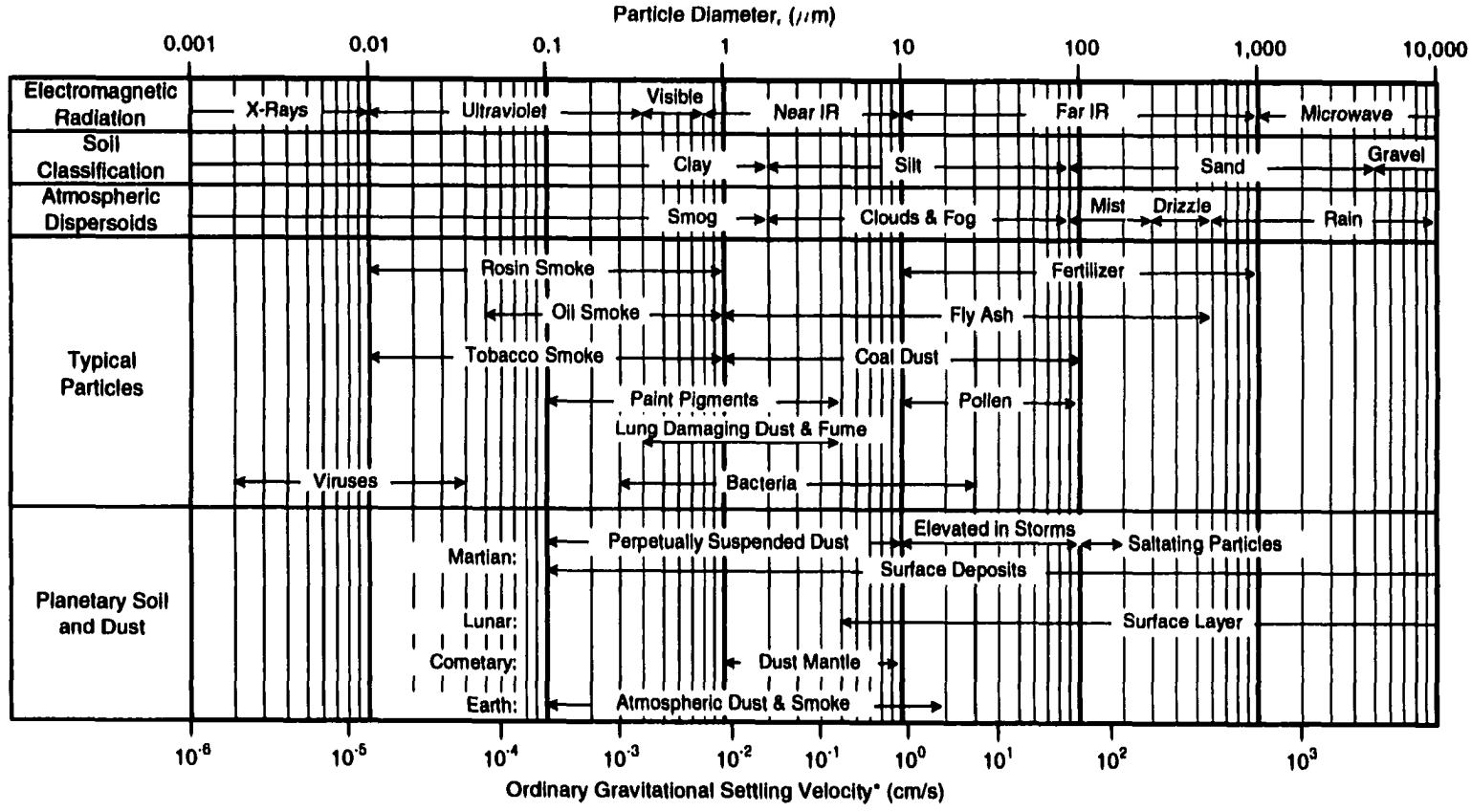

Spherical Particles with a Specific Gravity of 2.0, in Air, 20 deg C, 760 torr, 1 g

0.1 μm. Sedimentation is usually due to gravity and often follows Stoke's theorem. The gravity-induced velocity of 1 μm diameter dust particles in terrestrial air is 0.003 cm/s (Hoenig, 1988). Dust particle impact is due to wind-induced saltation or artificial disturbance. Smaller dust particles can be left behind by the impact of larger sand grain particles on surfaces. The other modes of transport are self-explanatory. (Khilnani, 1988)

1.2 Surface Mineralogy

Most planetary dusts are composed of silicate minerals such as quartz, olivine, or pyroxene. The silicon-oxygen bond in silicate minerals is 51% covalent and 49% ionic. Covalent characteristics contribute to the set angle of the silicon tetrahedron. The ionic characteristic results in a +0.96 e charge on the silicon atom at the center of the tetrahedron. Thus, the silicon atoms repel each other and tetrahedra share corners rather than edges. Examples of the molecular structure of some common silicate minerals are shown in the figure below. (DeVore,1963)

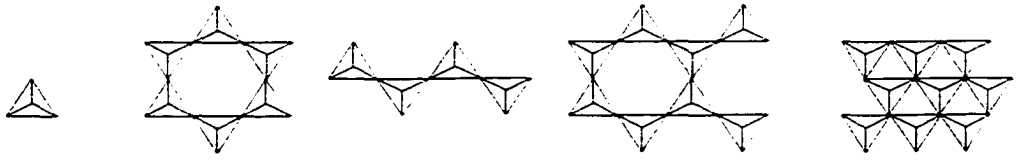

Olivine Beryl Pyroxenes Amphiboles Micas

Fig. 1.2 Examples of Silicate Minerals (Johnson & Greiner, 1965)

Various chemical reactions and crystal growth can change the mineralogical properties of dust particles at their surfaces. Examples of chemical associations are shown in Fig. 1.3. Quartz and feldspar can be transformed into pyroxene. Pyroxene can be changed to mica, and mica can be changed to amphibole. Amphibole is less reactive and typically in equilibrium with most planetary environments. (DeVore, 1963)

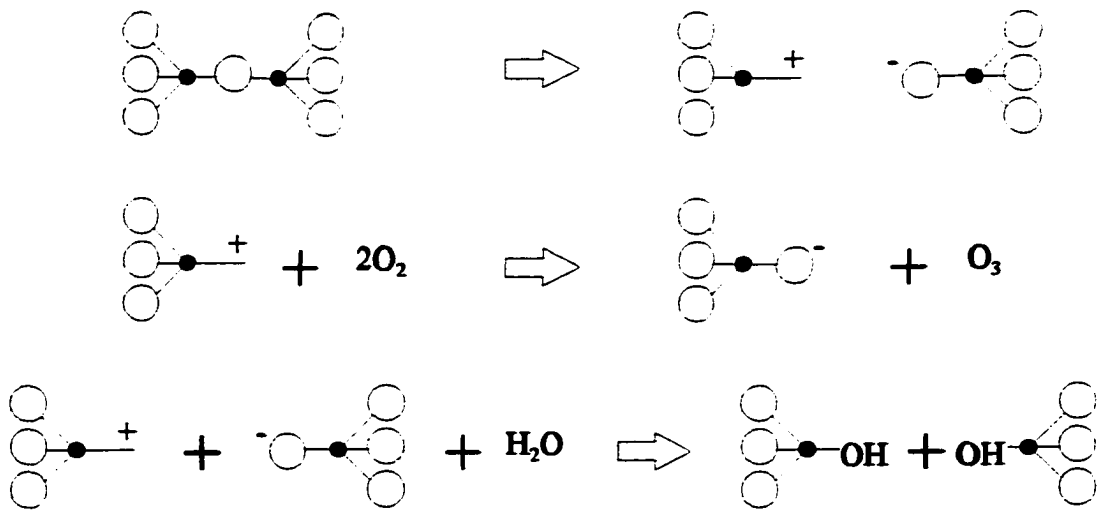

Fig. 1.3 Examples of Chemical Associations (DeVore, 1963)

1.3 Adhesion Overview

In a historical overview of the forces that cause adhesion, Israelachvili and Ninham (1977) describe a dichotomy of different views of intermolecular force: short range and long range. In the short range view, dust particles and surfaces are either in contact or are separate and adhesion is addressed through consideration of surface energies, hydrophobic/hydrophilic interactions, and hydrogen bonding. In the alternative long range view, dust particles and surfaces are separated by a certain distance. This distance governs the magnitude of adhesion

which is found through Hamaker, Derjaguin, and Lifshitz treatments of van der Waals interactions and Coulomb-type electrostatics. Ninham and others have shown that long range views of intermolecular force yield equivalent results as compared to short range views of the same interfacial phenomenon.

When the energy of gas adsorption is greater than the adhesion energy of the dust particle to a surface, the dust particle and surface will be separated by a layer of adsorbed gas. The thickness of adsorbed gas controls the spacing between a particle and a surface and is a function of ambient environmental conditions. Thus, different planetary environments produce different thicknesses of adsorbed gas. In order to account for the effect of different planetary environments on dust adhesion, it is necessary to take the long range view of intermolecular force.

There exist a number of models and techniques for evaluating capillary adhesion, van der Waals and electrostatic attraction, and accounting for the effects of elastic particle deformation. One model works well for predicting the adhesion of small, hard dust particles in dry environments. Another model provides accurate predictions of particle contact deformations and appears to correctly determine the adhesion of large, soft dust particles in dry environments. Capillary adhesion models match laboratory measurements in organic vapors, however capillary adhesion in water vapor is less well characterized. None of the current models predict increases in adhesion due to high vacuum, as was measured in many pre-Apollo laboratory experiments. Recent numerical and fracture mechanics solutions have been presented to evaluate particle adhesion. These solutions are cumbersome to extend beyond the specific cases for which they were developed. A more unified and versatile theory

of dust adhesion is needed to describe the behavior of different planetary dusts in the diverse environments present in the Solar System. There is also a need for dust adhesion research in cryogenic environments in order to predict dust behavior on comets, Europa, and other cold regions of space.

In the chapters that follow, a review of Martian and cometary dust properties is presented. The present state of knowledge regarding the physics and chemistry of dust adhesion is summarized. A new method of predicting the thickness of adsorbate between closely spaced solid surfaces is derived. The geometric relationship between the minor and major radii of a capillary pendular ring is revised to account for particle deformation and the presence of an adsorbed layer between the particles. A different behavior of a capillary pendular ring is explained. The mechanics of elastic particle contact are derived based on a superposition of Hertz compression and cylindrical indentor tensile contact solutions. All of the aforementioned activities and results are combined to derive a closed-form solution for determining dust adhesion. Laboratory measurements of mineral dust adhesion, conducted using a vibrating cantilever beam apparatus under different environmental conditions, are summarized. Experimental results are shown to match model predictions relatively well. The theoretical model is also successfully compared with prior laboratory research by others. The model is extended to predict dust adhesion on Mars and on comets.

2.0 PLANETARY DUST REVIEW

2.1 Comets

Astronomers believe that the early solar system consisted of dispersed ice and dust particles, some of which eventually grouped together to form the planets, much of the rest gathered into comet nuclei (Newcott, 1997). In many respects, a comet is a time capsule which has been frozen for billions of years; the study of comets may provide a glimpse into the origins of the solar system. Partly for this reason, NASA has formulated the Comet Nucleus Sample Return Mission. A spacecraft is tentatively planned for launch on a Delta-class launch vehicle in 2008 (Stetson, 1999). It will attempt to land on, drill into, sample and analyze a comet's surface. Subsurface exploration may extend to depths from 10 to 100 m. Approximately 200 g of comet nucleus material may be returned to Earth (Gulkis, Stetson and Stofan, 1998). The Comet Nucleus Sample Return Mission (CNSR) has been selected by NASA as the next highest-priority, large-scale, outer Solar System, exploratory mission (Green, 1999a).

In 1985, the International Comet Explorer (ICE) spacecraft flew through the tail of the Comet Giacobini-Zinner and obtained information on the plasma structure. In 1986, the European Space Agency Giotto instrument package and Soviet VEGA probes flew-by and photographed the nucleus of Comet Halley. Japanese spacecraft Sakigake and Suisei

observed Halley from a distance using UV cameras. (Huebner, 1990) The present knowledge base concerning comet composition and material properties is small. In order to develop mission technologies such as the landing, roving and sampling systems on CNSR, it is essential to estimate the composition and properties of cometary materials and to simulate those materials for systems testing. Determination of the mechanical properties of comet materials has been identified as a key technology need (Green, 1999a).

The surfaces of comets are believed to be covered by a thin, dry, dust-mantle overlying a harder core of dust and ice (Kochan, et al., 1989a, Thiel, et al., 1990, and Green, 1999b). It is further believed that between 20 and 70% by weight of comets is mineral dust primarily composed of olivine, montmorillonite, and carbon compounds (Roessler, et al., 1990 and Seidensticker and Kochan, 1992). Results of degassing comet simulants in an artificial space environment indicate that the dust mantle is held together by cohesive forces that exceed gravitational forces, and that these forces may be of van der Waals type (Lammerzahl, 1995). Additional investigation into the properties of the comet dust mantle is paramount to the success of the CNSR Mission and the understanding of comets in general.

2.2 Cometary Environment

The Solar System is surrounded by a spherical cloud of over 200 billion comet nuclei extending to a distance of approximately 100,000 AU from the Sun (Oort, 1950). Comets remain in the Oort Cloud until ejected into the inner Solar System by a gravitational "tug" perhaps caused by passage of a comparatively nearby star. Another possibility is that comets are ejected by collisions (Hartmann, 1989).

For many years, it was believed that comets consisted of a loosely packed structure of very angular dust particles with adsorbed gases. This theory is referred to as the "sand bank" model (Levin, 1943, and Lyttleton, 1953, Opik, 1966). In 1965, Comet Ikeya-Seki grazed the Sun at a distance of 0.005 AU, yet survived. In 1992, Comet Shoemaker-Levy 9 broke apart into 21 large fragments as it ventured into the strong gravitational field of the planet Jupiter. These events could not be explained by the "sand bank" model. In addition, thermodynamic models predict that an insufficient quantity of gas is released by desorption to account for the coma about comets (Huebner, 1990).

An alternative model proposed by Whipple (1950), known as the icy conglomerate model or "dirty snowball", was accepted for a long period as the correct interpretation of comet structure. This model describes comets as consisting of an aggregation of ice and dust covered by a mantle of dust. The mantle of dust is formed by repeated entry into the inner Solar System. Radiation from the Sun causes ice sublimation. Escaping gases lift-off particles of dust forming the comets coma and tail. Since gas molecules have smaller mass and higher thermal energy, much of the gas is lost into space, whereas, a considerable amount of the dust returns and settles back onto the Comet nucleus along the exit leg of its trajectory. The formation of a dust mantle over an aggregation of ice and dust has been simulated in laboratory (Grun, et al., 1991, Grun, 1991, Grun, et al., 1989, Kochan, et al., 1989a, and Kochan, et al., 1989b). The Whipple model explains repeated coma formation, gradual decrease in reflectance, survival of Sun grazing comets, splitting of cometary nuclei, and the cohesion of particles by non-gravitational forces (Gombosi, et al., 1986). More recently, Weissman (1996) presented a slightly different model, known as the "rubble pile" model. It

was explained that comet formation, splitting of cometary nuclei, rock abundance, and coma formation are better modeled by a porous aggregate of dust, ice, and rock.

Photographs of the nucleus of Comet Halley show two large jets of dust and gas venting from the sunlit side of the cometary surface. Although gas and dust are initially ejected toward the Sun, the solar wind redirects the gas and dust in the opposite direction, causing a shock front. The majority of the tail of a comet is always pointed away from the Sun. Ejected gas is subsequently ionized by the Sun's radiation, often resulting in a blue ion tail. In contrast, the dust coma reflects a yellowish hue. Erosion of the dust mantle and subsequent increases in sublimation explains increased post perihelion cometary activity. It has been suggested that the pressure of venting gases can also produce winds across the surface of a comet causing topographic alterations (Huebner and Boice, 1989).

Short period comets, like Encke, Tempel 1, Tempel 2, Kopff, Wild 2, and Wirtanen, have orbits about the size of that of Jupiter with periods of 3 to 9 years. Long period comets, like Temple-Tuttle, Halley, and Swift-Tuttle, have orbits on the order of that of Neptune with periods of tens to hundreds of years. Very long period comets, like Hale-Bopp, Donati and Hyakutake, have periods of thousands of years, and some, like Comet Levy, can leave the Solar System indefinitely.

It has been proposed that short period comets were formed at temperatures of approximately 40 deg K in the extended dust shell known as the Kuiper Belt, whereas, long period comets were formed in the Uranus-Neptune region at temperatures of approximately 80 deg K (Duncan, et al., 1988, Weismann, 1986, and Delsemme, 1988).

The structure of water ice depends on the temperature during formation. At very low temperatures, water ice has an amorphous structure. At 138.6 deg K, amorphous ice changes to crystalline cubic ice in an exothermic reaction yielding 67 J/g of energy (Klinger, 1982). At 160 deg K, cubic ice transforms to hexagonal ice in a thermoneutral process. At around 180 deg K, clathrate hydrates evaporate, resulting in the release of trapped gases. Hydrogen gas is trapped at temperatures below 50 deg K. (Bar-nun, et al., 1989) In comets, hydrogen is depleted three times less than the Solar System abundance (Gombosi, et al., 1986).

Although the temperature at the surface of a comet can be as much as 500 deg K at perihelion, the dust mantle provides an insulating barrier so that only a thin layer immediately below the dust mantle exists as crystalline ice. The interiors of active comets should contain a preserved mixture of amorphous ice and dust. With continued passes through the inner Solar System, dust mantle and crystalline ice layer thicknesses increase until there is sufficient insulation so that heat generated by the release of energy during transition from amorphous to crystalline ice causes the entire interior to change phase (Klinger, 1982). It is believed that comets have a finite life span after which there is insufficient gas to cause detectible coma development (Huebner, 1990).

The temperature during aggregation of protoplanetary nebula dust also determines whether a comet or asteroid will be formed. Generally, comets are formed at temperatures between 20 and 100 deg K resulting in amorphous silica and the preservation of all volatiles. At higher temperatures, crystalline silica is more likely to form, resulting in asteroids and meteorites with the preservation of some volatiles. (Greenberg, 1989).

Comets have nuclei on the order of a few kilometers in diameter and thus have negligible gravity. Comets contain micron-sized, silicate dust and organic refractory particles at an approximately 2:1 mass ratio, respectively (Greenberg, 1989). The silicate component is mostly neosilicates (i.e. olivine). A small percentage of phyllosilicates (i.e. montmorillonite and kaolinite) have been detected. Soot has been used to simulate the organic component in cometary simulants. Water is the major gas component in comets. Other more volatile species such as carbon monoxide, methane, ammonia, and carbon dioxide have been identified in small quantities. The mass ratio of dust to ice is approximately 2:1, respectively. Typically, cometary-simulant specimens are prepared in laboratory by spraying a dust/water suspension into liquid nitrogen. (Grun, 1991) The porosity of Comet Halley was found to be 0.8 by infrared observations (Greenberg, et al. 1995).

A possible target for the CNSR mission is the comet Temple 1. At perihelion, the temperature at the surface of Temple 1 is expected to be 235 to 268 deg K. Thermal modeling indicates a temperature of 176 to 187 deg K for ice just below the dust mantle, which is expected to be on the order of centimeters to meters thick. Water ice will have a crystalline structure to a depth of 40 to 240 m. Massive amorphous, gas-rich, ice is expected below that depth. Depending on surface topography, amorphous ice may outcrop at the bottom of active craters. (Bar-nun, et al., 1989).

2.3 Mars

Sources of dust transport and deposition on the surface of Mars include ordinary atmospheric settling, dust storms, dust devils, near surface saltation, and artificial

manned/robotic disturbance of the soil. Saltation occurs most prevalently for particles between 50 and 100 μm diameter at wind velocities over 15 m/s. The saltating boundary layer is expected to be up to 10 to 20 cm above the ground surface. Sand dunes and other geologic evidence indicates that aeolian processes are predominant in Mars geomorphology, however, wind velocities conducive to saltation have not been measured during previous missions (Sullivan, et al., 2000). It has been suggested that dust agglomeration due to triboelectric charging may result in a reduction in the saltation wind velocity threshold (Leach, 1991). Saltation is also expected during annual local dust storms, when wind velocities up to 32 m/s can be reached (Gaier, et al., 1990). The amount of dust loading during a Martian dust devil has been estimated to be 700 times that of ambient background conditions (Metzger, 1999).

A fairly steady rate of dust deposition on the solar panels equal to 0.3% light obscuration per sol day was measured during the first 25 sols of the Pathfinder mission (Landis and Jenkins, 1997). The density of dust in the atmosphere is approximately equal to 1.5×10^6 times the optical depth (Landis, 1996). The optical depth of the atmosphere in the vicinity of the rover during these measurements was approximately 0.5, which is typical of calm conditions at the landing site. Steady state dust opacity is a function of latitude and ground surface elevation (Clancy and Lee, 1991).

The chemical composition of the Martian regolith varies as much within a few meters as it does between the Viking and Pathfinder lander sites. This fact combined with global dust storm occurrences, indicates that there is a universal Martian dust unit of consistent average composition. The material is likely from a mafic igneous source (Clark, et al., 1982). Despite

the acceptance of a universal dust unit, there exists some debate as to its composition. The Viking model for the Mars surface deposits consisted of a mixture of iron rich clays, palagonite, and nanophase hematite. Aqueous weathering of SNC meteorites produces such an iron rich clay-like material (Gooding, 1991). Disc shaped particles with an aspect ratio of 1/10 explain dust settling rates after storms (Banin, 1989). Other atmospheric settling models showed that particles in the shape of oblate disks with aspect ratios from 1/1 to 1/4 also work well (Pitman, 2000). The best model for atmosphere-borne dust from Viking imagery is fine-grained magnetite based on refractive index. The Magnetic Properties Experiments on Pathfinder indicated that the dust is not pure hematite or magnetite. Rather, the results suggested that the dust is a composite material with some non-magnetic component such as a silicate mixed with a few percent of magnetic mineral. A preferred model is a smectite clay with nanophase maghemite or an iron-titanium spinal (Madsen, et al., 1999). Pathfinder APXS and IMP measurements do not match solutions based on alterations of SNC meteorites. Rather the measurements are indicative of a palagonitic altered Martian basalt rock plus minor locally derived andesitic rock fragments and nanophase geothite, akaganeite, schwermannite, and maghemite. (Bell, III, et al., 2000)

The existence of occasional global dust storms and daily dust devils on Mars has been well documented. Planet encompassing dust storms, such as the one occurring presently on Mars, are expected about every 3 to 30 years and can result in an optical depth of approximately 3 to 4 as measured by Mariner 9 (Gierasch and Goody, 1973). In addition to global dust storms, approximately 100 local dust storms occur annually on Mars. The majority of dust storms occur during the season surrounding the Southern Summer Solstice

at perihelion (Appelbaum, et al., 1993).

The extremely dry surface conditions and the fine particles which compose the Martian soil are conducive to charge buildup. Terrestrial dust storms can produce electric fields of 5-15 kV/m due to dust triboelectric charging. Laboratory experiments suggest that 5 kV/m electric fields may be produced in a dusty, turbulent Martian environment (Sentman, 1991). The Wheel Abrasion Experiment on the Pathfinder Sojourner Rover indicated that considerable electrostatic charge accumulated on the rover wheels during traverses over Mars soils. Earth-based tests in a simulated Mars environment resulted in a potential difference between the wheels and tracks of up to 300 V. The minimum of the Paschen discharge curve for carbon dioxide occurs at Mars atmospheric pressure and is equal to 100 V (Ferguson, et al. 1999). Thus, electric fields greater than 100 V are subject to glow discharge (Leach, 1991). Dust particles striking metallic, insulator and semi-insulator surfaces of any equipment used in future Mars missions may create electrostatic charges large enough to produce electrical discharges in the Martian atmosphere.

CHAPTER 3.0 DUST ADHESION REVIEW

Adhesion is the force between surfaces of different chemical composition, whereas, cohesion (also referred to as auto-adhesion by Zimon, 1969) is the force between surfaces of the same composition. Principles that govern adhesion are equally applicable to cohesion (auto-adhesion). The focus of this study is the adhesion of dust particles to different surfaces. However, it should be understood that all of the material presented can be applied to cohesion by using the same chemical parameters to describe both of the interacting media.

3.1 Adhesion Forces

Adhesion is caused by many different mechanisms. Sources of dust adhesion include a.) cold welding, b.) Lewis acid-Lewis base reactions, c.) cementation, d.) ice bridges, e.) capillary forces, f.) van der Waals forces, and g.) electrostatic forces.

Cold Welding

Cold welding ("sintering") is the covalent bonding of dust particles and surfaces at temperatures significantly below their melting points. A covalent bond is a type of chemical bond that involves the sharing of electrons. Moeller and Noland (1967) identified ten properties that influence cold welding: surface contamination, crystal structure, work

hardening, purity, hardness, elastic modulus, melting point, recrystallization temperature, atomic radius, and surface energy. The temperature at which cold welding can occur decreases with vacuum and particle size. In terrestrial air, cold welding can occur at 60% of the melting temperature. Hehn and Kimzey (1968) reported that cold welding of a variety of lunar soil simulant mineral powders occurred at room temperature in lunar-like vacuum after 3 to 4 days of vacuum pumping. Covalent bonding forces are very short range. A dust particle must be in intimate contact with a surface for these forces to be manifest. Surface contamination, adsorbed layers, and oxides must be removed in vacuum or penetrated by application of mechanical pressure in order to cause cold welding (Smith and Gussenhoven, 1965).

Lewis Acid-Lewis Base Reactions

A Lewis-base is an electron-donating or proton-accepting structure. A Lewis-acid is an electron-accepting or proton-donating structure. A bipolar substance can be either a Lewis-acid or a Lewis-base. A monopolar substance is always either a Lewis-acid or a Lewis-base. An apolar substance exhibits neither acidic or basic properties. The surface free energies for a Lewis-acid and a Lewis-base are defined as $\gamma+$ and $\gamma-$, respectively. Water is an example of a bipolar substance. For water, $\gamma+$ and $\gamma-$ are equal in magnitude (approximately 25.5 mJ/m^3, Good, 1993). The energy of Lewis-acid and Lewis-base reactions can be computed by

$$\Delta G_{AB} = -2(\sqrt{(\gamma_i^+ \gamma_j^-)} + \sqrt{(\gamma_j^+ \gamma_i^-)})$$

Hydrogen bonding and hydrophobic-hydrophillic interactions are examples of Lewis acid-Lewis base reactions (Good, 1993). Hydrophilic behavior can be manifested by either Lewis-acid, Lewis-base, or bipolar substances. Hydrophobic behavior is only exhibited by predominantly apolar substances with a Lifshitz-Van der Waals character that results in repulsion of water. Podczeck (1999) measured the adhesion of 32 to 45 μm diameter pharmaceutical particles to stainless steel surfaces with different types of surface treatment and found that adhesion force generally obeyed "Bruyne's Rule" which indicates that adhesion is strongest for particles on Lewis-base surfaces.

Cementation

Particle cementation is a process that involves the precipitation of dissolved substances at the contact between a dust particle and a surface thereby forming a bridge that can bind contact asperities together. About 1% of common dusts contain soluble components which greatly increase adhesion after humidity cycling. Deliquescence is the condensation of atmospheric moisture on water soluble material causing dissolution. Critical relative humidity for deliquescence of common salts range from 15% to 97%. (Williams and Nosker, 1988)

Ice Bridges

At a temperature below the freezing point of a gas, solid bridges can form between a dust particle and a surface. Water ice bridges are expected to contribute significantly to the adhesion and cohesion of dust particles on comets.

Greenberg, et al. (1995) presented a model to determine the tensile strength of the massive, dust and amorphous-ice conglomerate that comprises the interior of cometary nuclei. The model is based on a two-dimensional, homogeneous distribution of uniform-spherical, ice-covered, dust particles. Ice at the particle interfaces is presumed to control the cohesion. The author surmised that, due to impurities, the cohesive strength of an icey dust conglomerate is much less than the mean energy for hydrogen or dipole-dipole van der Waals forces. In order to obtain a tensile strength consistent with astronomical observations, it was assumed that the particles interact over a distance of 5 Å and that only the fraction of molecules at a distance less than 3 Å from the separation will contribute to the tensile strength at particle interfaces. A simple summation of intermolecular forces based on the r^{-6} dependence of van der Waals forces was used in the model.

Kochan, et al. (1990) presented a model to determine the bonding strength between dust particles at the surface of the comet mantle. The model again consisted of a two-dimensional face centered packing of uniform spherical particles. It was assumed by Kochan that cylindrical ice bridges develop between particle interfaces. Each particle is assumed to be held in place by interaction between two adjacent particles. The ice cylinders were given dimensions consistent with thermodynamic deposition of gas on curved surfaces. The strength of the ice was set equal to 1 MPa. A parametric analysis was performed by Kochan to estimate the diameter of ice cylinders based on the anticipated bond strength. It was shown that for even very small cylindrical bridges, the bond strength is too strong to account for ejection of dust by gas sublimation pressures. Possible mechanisms of bond failure were suggested, including the erosion of ice bridges by gas flow and fatigue fracture.

Ratke, et al. (1991) presented a model to explain the strength of ice particle contacts in a cometary crust. This model is based on the development of sintered necks by iterative sublimation and condensation. Sintering is defined as any process leading to the rearrangement of ice which is solely driven by curvature dependent gradients of chemical potential. If ice particles touch, a sintered neck will spontaneously develop as the ambient gasses condense to minimize the free surface energy of the agglomerate. Laboratory experiments were conducted using cometary simulant and a spherical indentor. Strength increases of nearly 30 kPa were measured for a freshly deposited particulate ice sample over the duration of 200 minutes.

The properties of water ice bridges depend on pressure, temperature, and ion concentration. About ten different phases of ice have been discovered. Most of these phases occur at high pressure. In vacuum, the three phases of ice are hexagonal, cubic, and amorphous. The only natural ice on Earth is hexagonal ice. Hexagonal and cubic ice have similar properties. (Warren, 1984)

The dielectric properties of ice depend significantly on the presence of dissolved ions. The relative permittivity of 30% ammonia ice is about 50% higher than pure water ice (Lorenz, 1998), whereas, the relative permittivity of 0.5% saline ice is about 90% less than pure water ice (Evans, 1965).

Capillary Force

In the presence of gaseous condensates, a liquid pendular ring can form. A pendular ring is a small amount of liquid held about the point of contact between two solid surfaces

with an axially symmetric meniscus (Orr, Scriven, and Rivas, 1974). The capillary force arising due to a pendular ring can be either attractive or repulsive depending on the chemical properties of the liquid and solid surfaces.

The interface between liquids, solids, and vapors have a specific energy per unit surface area, γ, that corresponds to the difference in chemical potential across the interface. Energy per area has units of force per unit length. Consequently, surface energy γ is often thought of as surface tension, especially for liquid-gas interfaces. The Young equation, which relates surface energies for a liquid in contact with a solid, is given by

$$\gamma_{SV} = \gamma_{SL} + \gamma_{LV} \cos \theta$$

where θ is the angle that the liquid makes with the surface and γ_{SV}, γ_{SL}, and γ_{LV} are the surface energy of the solid-vapor interface, solid-liquid interface, and liquid-solid interface, respectively. The Young equation can be derived based on conservation of energy, but is more simply obtained by static analysis of the free body diagram shown in Fig. 3.1.

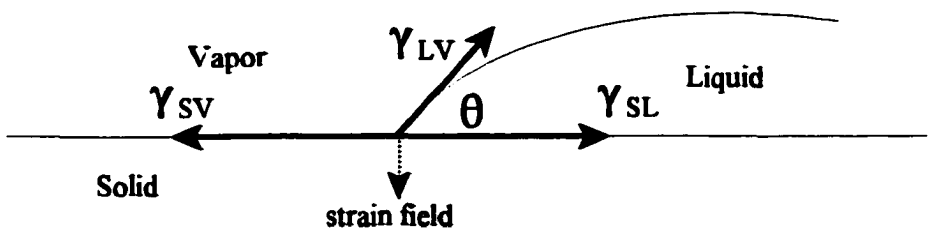

Fig. 3.1 Solid-Liquid Interface

Several measurements of surface free energy and contact angle are given in Chaudhury and Whitesides (1996). The contact angle between a liquid and a solid surface depends on a number of factors. A significant hysteresis is typically observed between advancing and

retreating contact angles. Surface roughness can appreciably affect contact angle. In a vacuum, solid and liquid surfaces have higher energy given by γ_S and γ_L The difference in surface energy between that observed in a vacuum environment and that observed within a vapor is called the equilibrium spreading pressure or the equilibrium film pressure, π_e, and is attributed energy expended in the formation of adsorbed gas films. (Good, 1993)

$$\gamma_S - \gamma_{SV} = \pi_{e\,SV}$$

$$\gamma_L - \gamma_{LV} = \pi_{e\,LV}$$

The spreading pressure, π_e, can be estimated using adsorption isotherms. According to Good (1993) the equilibrium film pressure is typically negligible for an apolar substance.

The geometry of a dust particle resting on a surface with a pendular ring is shown in Fig. 3.2. The well known Laplace equation that relates the pressure differential across a liquid-gas interface to the mean radius of curvature, r_m, is given by (Adamson, 1990)

$$\Delta P = \frac{\gamma_{LV}}{r_m}$$

The mean radius of curvature, r_m, is defined as

$$\frac{1}{r_m} = \frac{1}{r_c} + \frac{1}{r_s}$$

where r_c and r_s are the azimuthal radius and the capillary radius as defined in the figure. The well-known Kelvin equation for the free energy of an ideal gas is (Adamson, 1990)

$$\Delta G = RT \ln(\frac{P_o}{P_g})$$

where R is the Ideal Gas Constant, T is temperature, and P_o/P_g is the inverse of relative

humidity. From the definition of work, the change in free energy is

$$\Delta G = \int P \, dV$$

By combining the Laplace pressure, Kelvin equation, and the definition of work, the mean radius can be related to environmental properties of temperature and pressure as given by (Israelachvili, 1992, Orr, Scriven, and Rivas, 1974)

$$r_m = \frac{\gamma_{LV} V_L}{RT \ln(P_o/P_g)}$$

where V_L is molar volume. Similarly, the Laplace pressure, ΔP, can be shown to equal γ_{LV}/r_m..

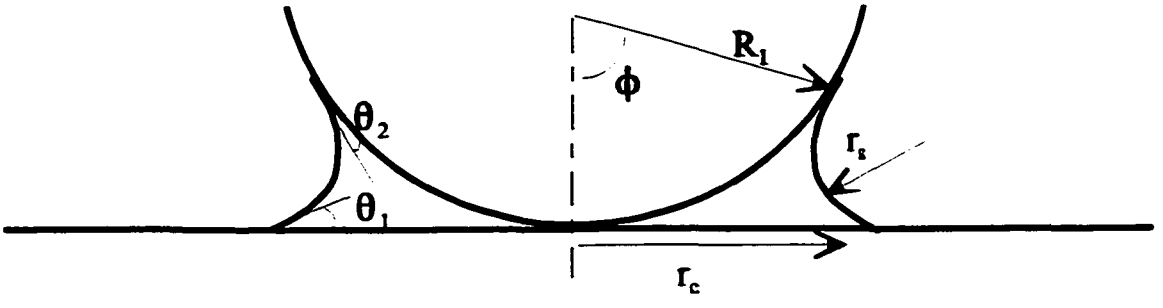

Fig. 3.2 Capillary Geometry (Ando and Ino, 1998)

From the geometry shown in Fig. 3.2, the azimuthal radius, r_c, can be related to the capillary radius, r_s, as follows (Ando and Ino, 1998)

$$r_c = (2 R_1 r_s (\cos \theta_1 + \cos \theta_2))^{1/2}$$

where R_1 is particle radius and θ_1 and θ_2 are liquid contact angles with the surface and dust particle. When ϕ is small, r_m is approximately equal to r_s. By substitution of the foregoing equation into the Laplace pressure equation and subsequent multiplication by pendular ring

area, the adhesion force of capillary tension can be shown to equal (Ando and Ino, 1998)

$$F_c = 2\pi R_1 \gamma_{LV} (\cos\theta_1 + \cos\theta_2)$$

when $\theta=\theta_1=\theta_2$, capillary tension reduces to (Fisher and Israelachvili, 1981)

$$F_c = 4\pi R_1 \gamma_{LV} \cos\theta$$

Orr, Scriven, and Rivas (1974) derived a more general equation for capillarity and explained that the capillary tension derived above is the limit as ϕ approaches zero of the general equation. If the azimuthal radius is considered, the capillary tension arising from this curvature of the meniscus is called the resolved surface tension and is given by (Fisher and Israelachvili, 1981)

$$F_{c2} = 2\pi R_1 \gamma_{LV} \sin\phi \sin(\theta+\phi)$$

Hence, where ϕ is not small, the curvature of the meniscus given by r_s must also be taken into account. For many liquids on surfaces including water, θ is a small angle. When azimuthal radius, r_c, is much smaller than the radius of the particle, ϕ is also a small angle. Thus, the sine of a small angle multiplied by the sine of another small angle is a very small quantity which indicates that F_{W2} can usually be neglected. The above derivation of capillary force has several shortcomings. Derjaguin has explained that calculations of capillary pressure must take into account the effect of long range forces due to nearby solid surfaces for small pendular rings. It will be shown later that the geometric relationship between azimuthal and capillary radii is incorrect if the particle is deformed or is not in direct contact with the surface.

Kordecki and Orr (1960) performed centrifuge dust-removal experiments and examined the effect of humidity on adhesion. Tests were performed at 10, 50, and 90%

relative humidity. Their results indicate that adhesion force is affected by humidity. However, the nature of the effect differed between materials. High humidity appeared to be indicative of low adhesion for spherical glass particles on aluminum, teflon, and enamel surfaces and for sand particles on glass surfaces. The opposite relationship was found for glass particles on brass and glass surfaces. They conclude that capillary forces depend on the hydrophobic/hydrophilic nature of the dust and the surface, and that capillary forces contribute little to dust adhesion when one surface is hydrophobic. In another investigation, Larsen (1958) showed that ten times more air pressure was required to remove dust particles from filter media at 40% relative humidity compared to that at 22% relative humidity. Podczeck, Newton, and James (1997) performed experiments at different levels of humidity using pharmaceutical powders. They discovered that force of capillary condensation between particles and surfaces depends not only on the composition of the materials but also their physical form. Lactos monohydrate particles exhibited a distinct strengthening in adhesion on a compacted salmeterol xinafoate surface with increased humidity. However, salmeterol xinafoate particles exhibited little change in adhesion on a compacted lactos monohydrate surface at different levels of humidity.

Using interferometry and diffraction patterns to look at microscopic crossed mica cylinders, Fisher and Israelachvili (1981) showed that the shape of the periphery of the contact zone immediately prior to removal by application of a direct pull-off force is a function of relative humidity. At low, medium, and high humidity, the periphery becomes sharper, more rounded, and completely rounded as removal force is applied. They also noticed that the spacing between mica cylinders was less than 10 Å even in water vapor at

99% humidity. After initial cylinder contact, trapped liquids flow out of the contact zone over a period of 1 to 10 seconds, until approximately a monolayer of fluid exists. The trapped fluid had an appearance resembling that shown in Fig. 3.3.

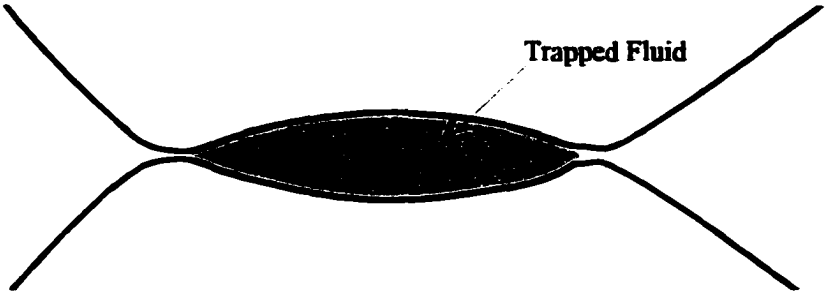

Fig. 3.3 Appearance of Trapped Fluid between Deformable Particles

Fisher and Israelachvili (1981) showed that the Young-Laplace equation correctly predicts capillary adhesion force for relative humidities of inert organic liquids as low as 10%. Furthermore, the Young-Laplace equation was shown to be inaccurate for water at relative humidities below 90%. It was found later by Christensen (1987) that the results of Fisher and Israelachvili are flawed in that the single spring used in their apparatus results in rolling and shearing instead of direct pull-off of a particle from a surface. His results, obtained using a double spring apparatus, do not match current capillary force models. He states that the capillary force at intermediate vapor pressures is the result of a complex interplay of adsorption-modified adhesion, surface deformations, and changes in capillary condensation. In an earlier investigation, Christensen (1985) measured an increase in the refractive index of water as vapor pressure decreases. This measurement indicates that the chemical properties of water condensate may be a function of the size of the pendular ring.

Capillary force can be repulsive particularly when ϕ is large or when θ_1 or θ_2 is greater than $\pi/2$ and especially when $\theta_1 + \theta_2$ is greater than π (Orr, Scriven, and Rivas, 1974). Capillary condensation only affects dust particle adhesion when the surface energy of the liquid is greater than the surface energy of the solid. Surface roughness typically has a negligible effect on capillary force (Fisher and Israelachvili, 1981).

Electrostatic Force

The electrostatic interaction between dust particles and surfaces can be modeled using the point charge approximation wherein all bound charge is treated as a single point charge at the center of a dust particle. Coulomb energy, U_{ELEC}, between two point charges, Q_1 and Q_2, is given by (Israelachvili, 1992)

$$U_c = \frac{Q_1 Q_2}{4\pi \epsilon_o \epsilon d}$$

where ϵ_0 is the dielectric permittivity of free space, ϵ is relative permittivity, and d is the distance between point charges. Interaction energy, U_I, between a single point charge, Q, and a neutral solid surface due to electrostatic polarization can be found through the method of images and is given by (Griffiths, 1999)

$$U_I = \frac{Q^2}{16\pi \epsilon_o \epsilon d}$$

where d in this equation is equal to the distance between the point charge and the surface. The closest distance of approach, d, of two dust particles is the sum of their radii and of a dust particle and a surface is the dust particle radius. Since force is the derivative of energy

with respect to distance, Coulomb and polarization electrostatic forces based on the point charge approximation vary quadratically with distance between surfaces, d, and hence with dust particle radius (Mullins, et al. 1992). The point charge analogy is appropriate for dust particles separated by large distances. When the dust particle is in direct contact with a surface, it is more appropriate to consider higher order multipoles (Fowlkes and Robinson, 1988).

Maximum dust particle surface electrostatic charge density is limited by Paschen discharge, charge spreading on the surface, and electric field build-up that prevents further charging (Poppe, Blum, and Henning, 2000). Paschen discharge is the breakdown of gasses surrounding the particle and surface. Discharging is less likely in narrow gaps where the breakdown voltage is raised in accordance with the Paschen curve (Feng and Hays, 2000). The maximum surface charge density in vacuum according to theory is 10^{-4} C m^{-2} or 625×10^{12} e m^{-2} (Horn, Smith, and Grabbe, 1993). However, electrostatic surface charge density as high as 5.4 C m^{-2} have been measured experimentally in vacuum (Lowell, 1986). Toner particles with 10 μm diameter that are used in xerography typically have an electrostatic charge of 8 fC (Rimai and Busnaina, 1995).

In electrophotography, toner particles are intentionally charged by collisions and triboelectric interactions with carrier beads. Mizes, et al. (2000) showed that electrostatic fields necessary for charged particle removal are generally an order of magnitude higher than predicted by theory if the charge is assumed to be uniform around the particle. Mizes proposed that the difference may be due to non-uniform charge distribution caused by the nature of particle impacts and triboelectric charging. Feng and Hays (2000) explained that

a non-uniform charge distribution in the shape of a dumbbell can cause approximately 2 times greater electrostatic adhesion compared with uniform charge distribution. The dumbell shaped charge distribution is shown in Fig. 3.4.

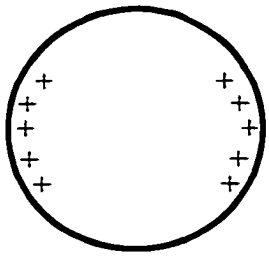

Fig. 3.4 Non-Uniform Electrostatic Charge Distribution

There are numerous processes that result in electrostatic forces between a dust particle and surface including a.) ion implantation, b.) photoionization, c.) triboelectrification, and d.) isomorphic substitution. These phenomena are described below.

a.) Ion Implantation

Solar and interstellar winds contain a flux of hydrogen ions (protons), electrons, and other ions. The magnetosphere prevents this plasma from reaching the surface of the Earth. On comets, asteroids, the Moon, Mars and other planetary bodies that lack such protection, ion implantation from solar and interstellar winds can be a significant source of dust particle electrostatic charge. A total electrostatic potential of 20 - 40 V was expected for lunar soils based on pre-Apollo ion implantation experiments (Johnson and Greiner, 1965).

b.) Photoionization

The photoelectric effect is the release of electrons from a solid surface due to illumination by electromagnetic radiation. Photoionization occurs only when photons have an energy greater than the work function of a surface. Work function is the amount of energy required to remove a single electron and is on the order of the ionization energy of the solid. The rate of ionization depends on the intensity of incident light.

In the solar radiation field at Saturn-like distances, dust charge from ion implantation and photoionization was found to cause a total electrostatic potential that varied from 0.21 to 0.38 V (Havnes, 1984). In a recent study by Sickafoose, et al. (2000), photoionization of dust was found to be only slightly significant compared to triboelectrification.

c.) Triboelectrification

Triboelectrification is the transfer of electrons between surfaces when rubbed or pressed together. Electrons typically move from a surface with low work function to a surface with higher work function in general accordance with the triboelectric series. A variety of studies have been performed in the past to investigate the triboelectric behavior of mineral particles in contact with surfaces (Tse-San, 1963, Balabanov, 1953, and Glazanov, 1950, Li, et al. 1999, Buehler, et al. 2000). The results of these studies were combined with the Triboelectricity Series of Polymers and Other Materials from Henniker (1962) and used to construct a draft triboelectric series for minerals, as shown in Table 3.1. Placement of minerals within the same cell or in the same line on the table indicate that available information was insufficient to identify their respective order in the series. A given minerals

Positive

(Low Work Function)

Fluorite, Cuprous Oxide, Barium Oxide	Forsterite
Microline	
Calcite, Barites	
Gypsum, Muscovite	
Copper	
Window Glass	
Lucite (Polymethylmethacrylate)	
Magnasite, Zinc Oxide, Nickel Oxide	Zircon
	Rock Salt
	Wool
Borosilicate Glass, Pyrex Glass, Fiberglass	
Cupperic Oxide, Aluminum Oxide, Hematite	Bauxite, Apatite, Magnetite, Chalcopyrite
Ilmenite	
Lexan (Polycarbonate)	
Marble, Garnet	Albite
	Augite
Hornblende	
Quartz	
Mars Fine Simulant	
Biotite, Ebonite	
Sulfur	
Selenium	
Teflon, Rulon J (Polytetraflouroethylene)	

(High Work Function)

Negative

Table 3.1. Baseline Triboelectric Series for Common Minerals and Surfaces

from Table 3.1 is expected to gain electrons when placed in contact with or rubbed against another mineral which is located higher in the triboelectric series.

Poppe, Blum, and Henning (2000) measured the electrostatic charge acquired by 0.5 and 1.2 μm diameter silica spheres impacting polished silica targets and found that the larger dust generally acquired a charge one order of magnitude higher than the smaller dust. They also found that 84% of the collisions resulted in the dust particles acquiring a net negative charge. A linear regression of the data on a logarithmic plot of acquired charge as a function of dust particle impact energy resulted in the following correlation between the absolute value of charge, Q, and the kinetic energy

$$| Q | = (1/2\ m\ v^2 \times 10^{15})^{0.03}$$

where m is particle mass and v is particle velocity relative to the surface.

Sickafoose, et al. (2001) measured triboelectrification of different types of dust falling through a pin hole in a box. Glass, silicon-carbide, JSC-1 lunar soil simulant, and JSC Mars-1 martian soil simulant dust particles were examined. The mean triboelectric charge was slightly positive for the glass and martian soil simulant dusts and was neutral for the other dust samples. Maximum positive triboelectrification ranged from +12 to +52 x 10^4 elementary charges, and maximum negative triboelectrification ranged from -20 to -52 x 10^4 elementary charges. Martian soil simulant exhibited the highest triboelectric charge.

d.) Isomorphic Substitution

All real materials contain impurities within the molecular lattice. These impurities cause the material to possess an inherent electric potential. As an example of this

phenomenon, the unit cell of gibbsite consists of an aluminum octahedron (aluminum atom centered among 6 oxygen atoms). If an insufficient quantity of aluminum is present during geologic formation of the mineral, another nearby atom may substitute. An illustrative candidate is magnesium. Since magnesium has one fewer valance electron than aluminum, a charge of +1 e will be imposed. Isomorphic substitution is the name given this process when it occurs naturally. The same process, when influenced by human intervention, is referred to as doping.

Van der Waals Forces

Van der Waals forces include dipole-dipole, dipole-induced dipole, and induced dipole-induced dipole (polarization) interactions. Van der Waals forces are always present between materials but have a very small range. Hamaker integrated the van der Waals force between a sphere and a surface by pair-wise summation and found that the result contained a coefficient that was a function of material properties. This coefficient is referred to as the Hamaker Coefficient and is represented by A_v. According to Hamaker, the van der Waals energy between a sphere and a solid surface is given by (Israelachvili, 1992)

$$U_{VDW_{sphere-surface}} = - \frac{A_V R_1}{6 d}$$

Derjaguin (1934) integrated van der Waals forces between two spheres and found the energy of interaction is given by (Israelachvili, 1992)

$$U_{VDW_{Sphere-Sphere}} = - \frac{A_V}{6 d} \left(\frac{R_1 R_2}{R_1 + R_2}\right)$$

where R_1 and R_2 are the radii of the interacting particles. Van der Waals adhesion force at distance d is the integral of work required to bring a particle from an infinite distance from the surface to the distance d away from the surface.

Lifshitz (1956) re-derived the Hamaker constant based on bulk physical properties of a solid using a quantum mechanical approach. He showed that the coefficient A_V is equal to

$$A_V = A_{v=0} + A_{v>0}$$

where $A_{v=0}$ is the orientation and induction component of van der Waals force and $A_{v>0}$ is the dispersion component of van der Waals force. A more thorough review of van der Waals forces and approximations for the Lifshitz components are given by Israelachvili (1992).

Laboratory investigations have validated, on numerous occasions, that van der Waals forces vary directly with particle radius. Due to their short range, van der Waals forces are substantially affected by dust particle shape and surface roughness.

3.2 Adhesion Force Measurement

There are a number of different methods that can be used to cause particle removal. These include vibration, centrifuge, impact, electrostatic repulsion, liquid or air flow, and direct pull-off using an atomic force microscope. The ratio of the number of particles remaining on a surface upon application of a removal method to the number of particles initially deposited on the surface is called the adhesion number. Dust adhesion force is typically measured at an adhesion number of 0.50, which is the point in an experiment where 50% of the dust particles have been removed (Visser, 1976).

A removal curve is a plot of adhesion number as a function of removal force. Several examples are shown in Fig. 3.5. The slope of a removal curve is often due to dust particle size range or gradation (Mullins, et al. 1992). A staged curve, as shown in the second example, is indicative of multilayer dust deposition where removal force is different for each layer.

Depending on the methods used in a dust removal experiment, there are a number of modes of particle detachment including lift-off, sliding, and rolling. Sliding and rolling usually require less force than direct lift-off. Furthermore, Soltani and Ahmadi (1994) calculated that rolling requires approximately half as much force as sliding.

Fig. 3.5 Examples of Dust Removal Curves

According to Khilnani (1988), electrostatic repulsion requires electromagnetic fields that are larger than the Pashen breakdown curves in air and, therefore, are impractical. However, this is contradicted by the fact that Mizes, et al. (2000) successfully used electrostatic fields to remove charged dust particles in laboratory experiments.

In vibrational experiments, adhesion force is determined from dust particle acceleration, α_ω, which is given by

$$\alpha_\omega = 4\pi^2 \omega^2 D$$

where ω is frequency in Hertz and D is amplitude of a sinusoidal displacement. Qi and Brereton (1995) present the results of ultrasonic particle removal experiments. They showed that high frequency waves most effectively remove particles in media with properties like water due to enhanced sound-particle interactions.

Particle detachment due to liquid or air flow is accomplished by either hydrodynamic drag or lift. The velocity of flow required to induce particle removal is called the entrainment threshold. Ziskind, Fichman, and Gutfinger (1997) studied dust particle detachment in turbulent air and water flow and found entrainment threshold to be a function of flow field and the force of adhesion. They also found that hydrodynamic lift was theoretically too small to overcome adhesion and that large particles required smaller wind velocities to be suspended compared to small particles. Shao and Lu (2000) found that entrainment threshold decreases with particle size to a minimum for approximately 100 μm and then increases with particle size. In tangential and normal gas jet experiments, entrainment threshold is strongly affected by gas jet duration (Phrases, Smedley, and Flagen, 2000). It has been found that blowing particle laden air over a surface can be an effective dust removal tool. The use of dry ice snow mixed with air may be a practical application of this method for the surface of Mars. Blowing dry ice laden air over semiconductor surfaces has been shown to remove dust particles as small as 0.5 μm (Hoenig, 1988).

3.3 Factors and Effects

Several factors affect dust particle adhesion, including particle deformation, duration of contact, gas adsorption, temperature, surface roughness, surface preparation, and number of neighboring particles. These effects are described below.

Particle Deformation

Surface deformation is an unavoidable for macroscopic particles (Cristensen, 1996). In 1881, Hertz derived an expression for the elastic deformation of two spherical particles in contact under an applied load F. The contact geometry was assumed to be elliptical. The vertical displacement of the surface of each sphere within the area of contact is given by

$$u_z = \frac{1-\nu^2}{E}\frac{3}{2} p_m \frac{\pi}{4a}(2a^2-\rho^2) \qquad \rho \le a$$

where ν is Poisson Ratio, E is Modulus of Elasticity, a is contact radius, ρ is distance from the axis of symmetry, and p_m is the mean contact pressure given by (Fischer-Cripps, 2000)

$$p_m = \frac{F}{\pi a^2}$$

The contact radius, a, is given by

$$a^3 = \frac{4}{3}\frac{K F R^*}{E}$$

where R* is the mean particle radius given by

$$\frac{1}{R^*} = \frac{1}{R_1} + \frac{1}{R_2}$$

and K is the elastic mismatch factor given by

$$K = \frac{9}{16}[(1-\nu_1^2) + \frac{E_1}{E_2}(1-\nu_2^2)]$$

where the subscripts 1 and 2 designate the elastic properties of the two materials (Fischer-Cripps, 2000). According to Hertz analysis, the contact area under zero applied load is zero. However, long range adhesion forces cause an area of contact to be established (Fuller and Tabor, 1975). Fisher and Israelachvili (1981) measured changes in dust particle contact area due to capillary forces.

In 1958, Johnson presented a model for determination of particle contact area based on the superposition of compressive Hertz deformation with the Boussinesq solution for a cylindrical punch in tension. The result produces tension along the periphery of the contact and compression within the center region. In this manner, an elastic contact area can be developed under zero applied load. The integral of contact stress over the contact area is equal to zero unless an external load is applied.

There exists some debate as to the effect of elastic deformation on dust particle adhesion. From one viewpoint, elastic deformation should not affect adhesion force because the force available to restore a particle's shape is always sufficient to counteract the additional attraction (Berbner and Loffler, 1994). Derjaguin, Muller, and Toporov (1975) theoretically calculated that deformation does not increase dust adhesion force. In their model, van der Waals forces cause deformation, but adhesion force is equal to that which would be determined if deformation where ignored. However, in experiments on lunar dust simulants in vacuum, Hehn and Kimzey (1968) found that the adhesive force decreased as material hardness increased. Podczeck (1999) also found that the adhesion of pharmaceutical dusts

to stainless steel could be reduced by the application of hard coatings such as chromium carbide and plasma chromium.

Rimai and Busnaina (1995) suggested a dependence of adhesion force on the Modulus of Elasticity and stated that compliant materials are more adhesive than less compliant materials. Krishnan, et al. (1994) explained that when adhesion pressures exceed the yield point of a material, plastic deformation occurs which may affect adhesion force. Maugus and Pullock (1995) presented an adhesion model for fully plastic deformation and found the adhesion energy is given by

$$U_a = 3/2\ a^2\ \sigma_y$$

where U_a is the work of adhesion, a is the contact radius, and σ_y is the plastic yield strength. Plastic yield strength was typically taken as 1/3 the material hardness.

Busnaina (1995) computed that there exists a minimum velocity of a particle impacting a surface in order for plastic deformation to occur. Dominik and Tielens (1997) described a hierarchy of kinetic energies associated with the behavior of dust aggregates impacting on surfaces. Different energies have been proposed for certain behaviors as shown in Table 3.2. These velocities are for micron size particles.

Broom (1979) showed particle rebound was a function of surface roughness. Wall (1990) found that rebound was not a function of surface material composition at velocities greater than 40 m/s. Brownian dust motion is associated with velocities on the order of 0.01 m/s (Blum, 2000). Poppe, Blum, and Henning (2000) found a distinct capture limit between 1.2 to 2.5 m/s for spherical particles, whereas non-spherical grains had 10% sticking at all velocities.

There also exists some disagreement as to the relationship between contact radius and the radius of dust particles. For elastic deformation, the contact radius is believed to be a function of the particle radius to the 2/3 power, while for plastic deformation the contact radius is a function of the square root of the particle radius (Maugus and Pullock, 1995). Using scanning electron microscopy, Drishnan, et al. (1994) found contact radius was a function of the square root of particle radius. Rimai and Busnaina (1995) performed nanoindentor experiments and microscopic examinations and showed that the contact radius was a function of the particle radius to the 2/3 power for soda glass dust on a polymer surface, the radius to the 3/4 power for larger glass particles on polyurethane substrates, and the radius to the1/2 power for glass particles on a silicon substrate.

	Particle Velocity (m/s)	
	Dominik & Tielens	*Blum*
E1	*0.05*	*0.2*
E2	*0.16*	*0.7*
E3	*0.14*	*1.0*
E4	*0.26*	*1.9*

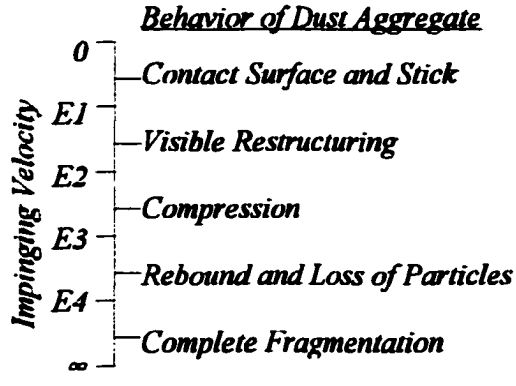

Table 3.2 Effect of Impact Velocity on Dust Particle Behavior

Duration of Contact

Dust particle adhesion is highly dependent on resident time of the dust on some materials. Typically longer resident times cause stronger adhesion due to increases in contact area with time dependent deformation or creep (viscoelasticity). Adhesion strength increases

have been measured to occur for polystyrene spheres on silicon substrate for up to 72 hours (Krishnan, et al., 1994). Using a SEM micrograph, Rimai and Busaina (1995) showed that viscoelastic creep for micrometer sized polystyrene particles on a copolymer surface occurred for more than 2 weeks. However, the authors explain that deformations measured in the first hour correlate reasonably well with model predictions. Deformation with time is approximately similar to that which would be predicted by consideration of creep. Over time, plastic deformation approaches elastic deformation for viscoelastic materials (Berbner and Loffler, 1994).

Bowen (1991) found adhesion strength increased over the period of only a few minutes for glass spheres interacting with polyurethane substrate. Polk (1971) conducted dust adhesion tests over a period of 100 minutes and found that adhesion depends on time mostly at high temperatures. Adhesion force was on the order of 100 times stronger after 100 minutes than initial adhesion at 400 deg C. Schoddert showed cold welding adhesion increased with time up to 500 minutes (Berbner and Loffler, 1994). The contact radius between rubber spheres on Perspex surfaces with different degrees of roughness was also found to be time-dependent. This time dependence was on the order of 5 minutes and was a function of surface roughness. Equilibrium contact areas were obtained almost immediately for smooth surfaces (Fuller and Tabor, 1975).

Gas Adsorption

Adsorbent is a solid surface. Adsorbate are adsorbed gas molecules, and adsorptive are the free gas molecules in equilibrium with the system. Sir William Hardy (1936) theorized

that solid surfaces are separated by layers of adsorbed gas. Temperature, pressure, and atmospheric composition control adsorbate thickness. Hence, different planetary environments may produce variations in adsorbate and adhesion. Bowden and Tabor (1950) showed in vacuum experiments that adsorbed water can reduce contact area and adhesion. Derjaguin (1961) explained that adsorbed gas layers are drawn between surfaces in order to satisfy electric double layer energy requirements and called the phenomenon disjoining pressure. Perko, Nelson, and Sadeh (2001) and Perko (1998) applied these theories in an attempt to model dust particles separated by pressurized layers of adsorbed gas. They used the adsorbed gas thickness to represent the distance over which interparticle forces act. Their method of predicting this thickness were based on the Polyani theory (Adamson, 1990). However, adsorption energy fields used in the method were computed using a simple Hamaker summation involving free gas molecules and did not account for interference, successive polarization, or electric double layers. The model was predominantly developed for ultrahigh vacuum environments, and it is expected to be inaccurate in areas with higher pressure. A new method for determining adsorbate thickness between dust particles is needed.

All material surfaces are characterized by heterogeneties in adsorption potential. Lateral spreading of adsorbate is governed by variations in the adsorption potential. In general, if the fluctuations in adsorption potential are much less than kT, where k is the Boltzmann Constant and T is temperature, then free lateral movement can occur and adsorbed phases are mobile. The partition function contains an additional term for lateral degrees of freedom in this case, whereas, if the fluctuations in adsorption potential are much greater than

kT, lateral movement is hindered and adsorbate may be localized. (Rudzinski and Everett, 1992)

If the adsorption potential of a surface is considerably greater than kT, there may exist a separate adsorbed phase identified by a sharp transition in density at adsorbent surface. If the adsorption potential is on the order of kT, no abrupt change in density is expected and the adsorbate can be treated as a bulk fluid in a potential field.

Temperature

Hehn and Kimzey (1968) exposed various materials to lunar dust simulants in simulated lunar conditions and found that adhesion to polymeric materials was affected by temperature. Less dust adhered at colder temperatures, whereas, no detectable effect of temperature was found for dust adhering to metals, ceramics, and glass.

Surface Roughness

Surface roughness can reduce adhesion by decreasing the radius of curvature of contacting asperities. For very small roughness, adhesion is largely unchanged. In atomic force microscope investigations, Ando and Ino (1998) found no effect of microsurface roughness on adhesion. When the scale of surface roughness is at or near the size of dust particles, then the particles can occupy positions on the crests of surface asperities or within the depressions in between asperities. Adhesion is anticipated to be stronger within depressions as compared to that atop crests. Mizes (1995) showed that the DMT model (to be presented in the next section) approximates the effect of adhesion at the particle crests.

Surface roughness may be characterized by the height, spatial distribution, and curvature of asperities (Ziskind, Fichman, and Gutfinger, 1997). Johnson (1971) quantified surface roughness in a single parameter termed the asperity height distribution, which was defined as follows

$$\Psi(z_h) = \frac{1}{\sqrt{(2\pi)}} \exp(-\frac{z_h^2}{2\sigma_h^2})$$

where z_h is the height of the asperities and σ_h is the standard deviation in height. Johnson explained that, for roughness on the scale of the contact area between a dust grain and a surface, higher asperities are deformed and act to separate the surfaces, whereas, lower asperities act to pull surfaces together. Rabinovich, et al. (2000) derived a model for the adhesion force of a dust particle separated from a surface by a smaller hemispherical asperity. Ziskind, Fichman, and Gutfinger (1997) presented a similar model that accounts for multiple asperities.

Gane, Pfaeizer, and Tabor (1974) used hard solids (titanium, sapphire, and diamond) in 10^{-10} Torr vacuum and found adhesion was 100 to 1,000 times smaller than predicted by the DMT model. They concluded that surface roughness was the source of the discrepancy. Mizes, et al. (2000) reported that the presence of aerosols can reduce adhesion in the same way that particle roughness affects adhesion. Aerosols, which are on the order of 1,000 times smaller than the larger dust particles that they adhere to, can reduce adhesion by a factor of 4 to 5.

Surface Preparation

A variety of techniques have been used to clean surfaces for dust adhesion testing. Braaten (1994) used ammonium hydroxide to clean glass slides for wind tunnel dust-deposition experiments. Blum (2000) used a hydrophobic coating to treat surfaces in dust impact tests. Kordecki and Orr (1960) and Mullins, et al. (1992) used polonium and/or radium to neutralize electrostatic charges on surfaces. Bead blasting has been used to modify surface roughness (Fuller and Tabor, 1975). Hill and Cakmak (1965) used acid etching in a 0.2 M HCL bath and an oxide inhibitor to prepare samples for vacuum experiments. They also used 200 to 300 deg C temperatures in ultrahigh vacuum to remove adsorbed water.

In general, acid washes remove trace metals and ions from surfaces. Use of a degreasing solution removes organic contaminants. The ASTM standard method for cleaning semiconductor surfaces, known as the RCA Clean method, consists of the following steps: 1.) remove organics by oxidation, 2.) remove trace metals and chemisorbed ions by solubilization, and 3.) an optional hydrofluoric acid etch to remove oxides. (Khilnani, 1988)

Neighboring Particles

Calculations for arrays of uniformly charged dust particles arranged in a monolayer indicate that electric fields from neighboring particles may increase adhesion by a factor of 5 or greater. However, centrifugal experiments by Mizes, et al. (2000) show that the adhesion of particles is independent of the number of neighboring particles. The degree of particle coverage used by Mizes was limited to 40% of a monolayer.

3.4 Adhesion Models

One of the earliest theoretical models for dust adhesion was by Wintercorn (1910). The Wintercorn model relates contact area to dust particle radius through simple geometry and the chord law. The energy required to compress a sphere was used to derive the contact pressure. A random distribution of Si-O and O-O bonds was used to determine surface adhesion energy. An equilibrium contact area and subsequent adhesion force was determined by equating elastic energy and surface adhesion energy. (Johnson and Greiner, 1965)

The two most referenced methods of dust adhesion force computation are the JKR theory (Johnson, Kendel, and Roberts, 1971) and the DMT theory (Derjaguin, Muller, and Toporov, 1975). Johnson, Kendel, and Roberts derived their theory of adhesion by equating the contact surface energy with stored elastic energy in a manner similar to that used by Wintercorn, except that a more sophisticated analysis of elastic stress and a better definition of surface adhesion energy were used. Contact radius was set equal to that found by Hertz. Stresses and displacements caused by a cylindrical indentor with a radius equal to that of the Hertz contact were superimposed following the procedure established by Johnson (1958). A load-displacement relationship, given by

$$\delta = \frac{9}{32} \frac{F}{E_1 K a}$$

was found. From this, the authors were able to derive a new expression for stored elastic energy of the contact given by

$$U_E = \frac{9}{16 K^{2/3} R^{*1/3}} \left[\frac{1}{15} F_1^{5/3} + \frac{1}{3} F_0^2 F_1^{-1/3} \right]$$

where F_1 is applied external load plus adhesion force and F_0 is applied external load. Surface adhesion energy was expressed as

$$U_a = -\gamma_{SV} \pi a^2$$

and mechanical work as

$$U_m = -P_0 \delta$$

Total energy of the systems was found by summing stored elastic energy, surface adhesion energy, and mechanical work. Contact area at separation was determined by taking the derivative of total energy with respect to area and setting the result equal to zero in order to find the minimum. The solution for adhesion force was computed by input of the final contact area into the equation for adhesion force which yields

$$F_a = 3\pi R^* \gamma_{SV}$$

The contact radius at the instant of separation of the dust particle from a surface is equal to $(1/4)^{1/3}$ or 0.63 times the contact radius at zero load.

In subsequent experimentation by others, the JKR theory was found to correctly predict equilibrium and final contact areas of elastic particles. Computed adhesion force was generally most accurate for soft, elastic, or high energy surfaces. The JKR theory is the only theory developed to date that correctly describes surface stresses at the particle contact. It predicts the integral of surface stresses is equal to zero when no external load is applied to the particle. Shortcomings of the model include infinite stress at the periphery of the contact and failure to account for adhesive forces outside the contact area.

Derjaguin, Muller, and Toporov derived their theory of adhesion by first determining the geometric shape of a particle outside the contact area. Using Hertz theory, Lifshitz and

Landau elastic deformation, and simple geometry, they found the spacing, z, between two spherical particles or between a spherical particle and a curved asperity as a function of distance from the center of contact, ρ, given by

$$d = \frac{1}{\pi R^*}[a(\rho^2-a^2)^{1/2} - (2a^2-\rho^2)\, atan(\frac{\rho^2}{a^2} - 1)^{1/2}] + z_o$$

where z_o is the equilibrium spacing between the surfaces at the contact (which is usually taken to be 4 Å where Lennard-Jones potential is assumed to intersect van der Waals force).

Based on definitions of elastic energy and force, surface energy, geometry, Hertz elastic repulsion, and Hamaker type attraction, Derjaguin, Muller, and Toporov derived an equation for the adhesion and found it to be a maximum at the singular point of contact before elastic deformation or after elastic rebound when the contact area is zero. The maximum force of adhesion is given by

$$F_a = 4\pi R^* \gamma_{SV}$$

Through extensive experimentation by others, the DMT theory was found to more correctly predict adhesion force as compared to the JKR theory. The success of the DMT theory in predicting adhesion force is due to the fact that it accounts for long range forces that act outside of the contact area. The equilibrium contact area under zero load is approximately half of that predicted by the JKR theory and does not appear to match experiments very well. The distribution of stresses at the particle contact are incorrect. Integration of these stresses does not yield zero under no externally applied load. In order for static equilibrium to exist, adhesion forces must apply tension to the surface equal to the compression applied at the interior of the contact.

There has been a long debate regarding the appropriateness and application of the JKR and DMT models and many laboratory investigations to verify each of them. Rimai and Busnaina (1995) experimentally showed that the radius of the contact at particle separation was approximately 0.7 times the contact radius under zero load in accordance with the JKR theory. Horn, Israelachvili, and Pribac (1987) performed experiments using mica covered crossed-cylinders, which are geometrically similar to the interaction of a sphere and a surface, and found that the equilibrium contact radius was larger than that predicted by the JKR theory, and the pull-off radius was finite with a value of approximately 0.63 times the equilibrium contact radius. The deformation profile matched that predicted by the JKR theory except at the perimeter of the contact area where it sloped 25 degrees independent of load. According to Fisher and Israelachvili (1981), the JKR theory most correctly approximates the shape of deformable particles in contact with surfaces, whereas conclusive evidence shows that the DMT model best describes the adhesion force.

According to Tabor (1977), the DMT theory can not be correct because laboratory experiments almost always suggest that contact area is twice that predicted by the theory. Tabor also pointed out that dust particles are unstable according to the DMT theory, because the adhesion is not a maximum at rest. Tabor is critical of the JKR theory because of the discontinuities in the stress distribution shown in Fig. 3.6.

Tabor defined a parameter, μ_T, to describe particles with respect to their surface energy and elasticity.

$$\mu_T \equiv \left[\frac{R^* \gamma_{SV}^2}{E^2 z_o^3}\right]^{1/3}$$

A large Tabor parameter indicates large particle deformations and a small Tabor parameter indicates small deformations.

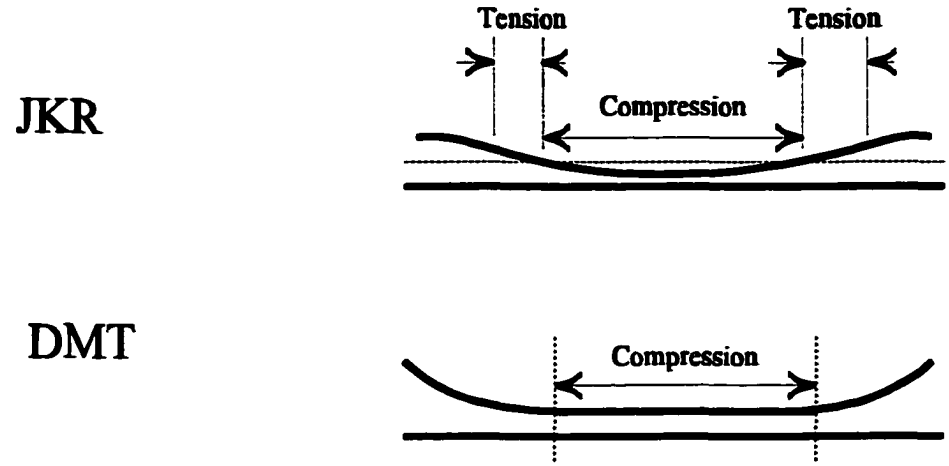

Fig. 3.6 Contact Stresses (Modified from Tabor, 1977)

Muller, Yushchenko, and Derjaguin (1983) attempted to correct some of the shortcomings of the earlier DMT theory by accounting for Lennard-Jones repulsion within the contact between dust particles and surfaces. A series of non-dimensional integrals were presented that better represent surface contact stress and satisfy static equilibrium. Closed form solutions to the integrals were not obtained, however some insight as to the behavior of particles at extremum was revealed. Specifically, they showed that their model approached the JKR theory when the Tabor parameter was large and approached the DMT theory when the Tabor parameter was small.

Maugis (1992) presented a crack propagation model for a rigid indentor interacting with an infinite half-space. A numerical solution was found using a Dugdale model. It was determined that as the ratio of crack length to crack radius approaches infinity the solution

approaches the DMT model, and as the ratio of crack length to crack radius approaches zero the solution approaches the JKR model. The Maugis model predicts a finite adhesion value and contact area at separation. The model also indicates a removal force for particle rolling on the order of 1.5 times that predicted by the JKR theory. Griffith (1996), Barenblatt (1996), Lawn (1995), and Chen (1997) also presented models for dust particle adhesion based on fracture mechanics.

Each different dust adhesion theory addresses the force from outside the contact area differently. The following table summarizes those treatments.

Table 3.3 Adhesion Forces from Outside Particle Contact Area (Maugis, 1991)

Theory	Adhesion Force Contribution from Outside Contact Area	
	at Zero Load	at Point of Seperation
JKR	0	0
DMT	$\pi U_a R^*$	$2\pi U_a R^*$
Muller	$>2\pi U_a R^*$	$2\pi U_a R^*$
Maugis	$2\pi U_a R^*$	$2\pi U_a R^*$

Feng (2000) presented a computational study of particle adhesion and deformations and theoretically showed that dust particles exhibit different behaviors in accordance with the Tabor parameter. A hysteresis in the load-approach curve was found that indicates a "jumping-on" and "jumping-off" behavior when the Tabor parameter is large.

Fogden and White (1990) developed a model for the adhesion of dust particles in the presence of capillary condensation. The development of the model followed that of the JKR theory except that capillary force was added to derive the net adhesion force. However, they did not compute the increase in contact area which should arise from addition of capillary force. Muller, Yushchenko, and Derjaguin (1983) were critical of Fogden and White for following the JKR theory and omitting adhesion forces from outside the contact area.

Derjaguin (1961) derived an expression for the influence of capillary force and adsorbed films on particle adhesion. The model accounts for the possibility that dust particles are separated from surfaces by pressurized layers of adsorbed gas. The pressure in the adsorbed layer is shown to be the result of colloidal repulsion due to electric double layers. However, the model does not take into account effects of particle and surface deformation.

A theoretical model relating environmental parameters with the friction and cohesion of granular materials was developed at Colorado State University (Perko, Nelson, and Sadeh, 1996). The model consists of three components, namely A.) a set of equations for estimating adsorbate thickness on dust particles as a function of material and gas chemistry, ambient pressure, and temperature, B.) an equation for calculating the van der Waals intersurface force between grains of dust, and C.) equations for the friction and cohesion of an aggregation of dust particles. A brief overview of model development and basis is presented herein. More detail is contained in Perko (1996) and Perko, Nelson, and Sadeh (2001).

In conjunction with the development of the model, a new parameter, termed *surface cleanliness*, S, was introduced as a convenient parameter to quantitatively describe dust particle surfaces with different adsorbate thicknesses. Specifically, the parameter is defined

as the nondimensional inverse of adsorbate thickness given by

$$S = \frac{\Omega}{t}$$

where t is adsorbate thickness and Ω is the diameter of an oxygen ion (1.32×10^{-10} m, 1.32 Å). The value of Ω was selected as the characteristic dimension, because it is approximately equal to the radius of a dust molecule composed of any one of a number of possible oxides. According to the way in which it is calculated, t is the distance from the center of the outermost mineral molecule to the center of the outermost adsorbate molecule. The convenience of defining surface cleanliness in this way is that adsorbate t varies from Ω to an infinitely approaching distance, and thus surface cleanliness varies from 0 for a "saturated" surface to 1 for a "clean" surface. Furthermore, S is approximately equal to the inverse of the number of atomic gas layers.

Adsorbate thickness can be estimated using the Polanyi potential energy treatment (Adamson, 1990), which states that adsorbed gas occupies the space around a dust particle within which the intermolecular potential energy is sufficient to cause condensation. Setting the intermolecular energy between a dust particle and a gas molecule equal to the energy of condensation yields an adsorbate thickness given by

$$t = \frac{3s_1\zeta^{--}}{3s_1\zeta^{2/3} - s_-}$$

$$\zeta = \frac{1}{2s_1}\left[s_3 + \frac{1}{9}\sqrt{12s_2^3s_1^{-1} + 81s_3^2}\right]$$

where t is adsorbate thickness and s_1, s_2, and s_3 are surface cleanliness coefficients that depend on van der Waals forces, electrostatic charge, molecular density, temperature, and

pressure. The spacing between dust particles is equal to 2t.

The van der Waals force between surfaces can be determined based on the bulk solid state properties of materials and the intermediate medium using the Hamaker summation method in conjunction with the Lifshitz theory (Adamson, 1990). Since van der Waals energy fields are additive, they can be pair-wise integrated over the volume of dust particles to determine interparticle force. For simplicity, dust was modeled as spheres of equal radii that are deformed at their contact and separated by pressurized layers of adsorbate. The reduction in adsorbate thickness due to mechanical pressure necessary to cause deformation was accounted for.

To facilitate integration, the spherical dust grains are treated as a series of cylinders with wall thicknesses, $d\lambda$, as shown in Fig. 3.7. Deformation of the particles is assumed to result in a circular plane at their contact, which is represented by the end of the center cylinder having a diameter of $2\lambda_o$. The yield stress at the particle contact was determined by elastic theory using the Modulus of Elasticity for quartz. The total interparticle force is the sum of the forces between all the cylinders, given by

$$F = \frac{A_V}{6\pi\sigma_y d^3}N + \frac{A_V R^*}{12d^2}$$

where A_V is the Hamaker coefficient, N is normal force, σ_y is yield stress, d is particle spacing, and R* is mean particle radius.

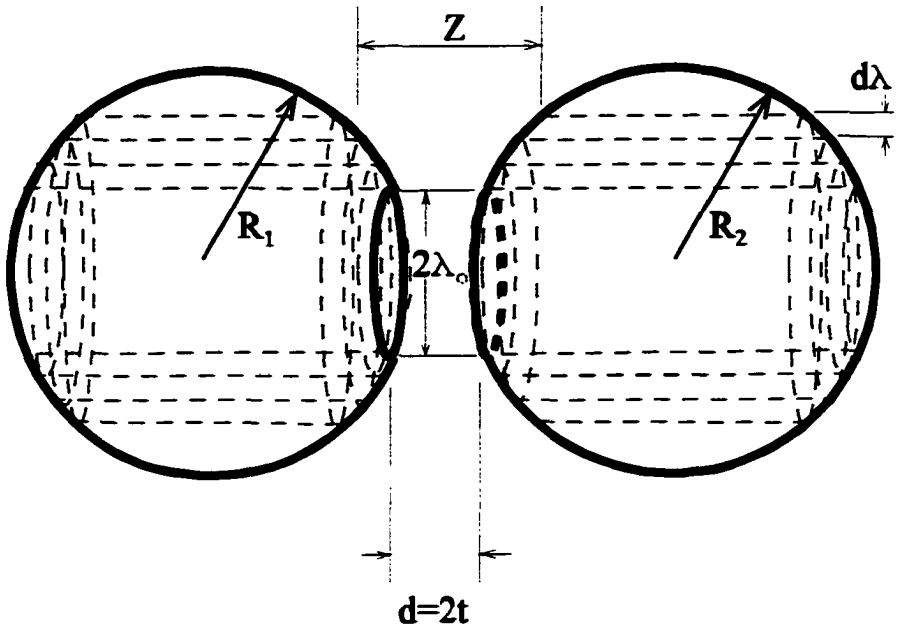

Fig. 3.7 Deformed Dust Particles

Forces preventing the movement of a particle within an bulk soil are the result of gravity, interlocking, and mineral surface friction with the surrounding particles. The additional friction and cohesion caused by surface cleanliness and the interparticle force were determined by summing moments about the contact a particle contact. Incipient motion of particles occurs when the externally applied forces balance the internal resistance. Moment equilibrium analysis resulted in two terms; one was independent of stress, while the other was linearly dependent on confining stress. Thus, the solution could be separated into a friction component given by

$$\tan \phi_{SC} = \frac{A_V}{6\pi \sigma_v d^3}$$

and a cohesion component given by

$$c_{sc} = \frac{A_V \eta R^*}{12d^2}$$

where ϕ_{sc} is the angle of friction, c_{sc} is cohesion, and η is number of particle contacts per unit area. All other parameters have been defined previously.

Predicted increases in shear strength based on the surface cleanliness model compare well with the results of ultrahigh vacuum experiments previously conducted at IIT Research Institute using granular obsidian, quartz, and enstatite (Nelson and Vey, 1968). For example, the increase in shear strength at ultrahigh vacuum as measured by a direct shear test using enstatite is shown in Fig. 3.8. Smaller strength increases were measured in vacuum experiments using olivine powder. The model over predicted the strength increases for olivine, as shown in Fig. 3.9.

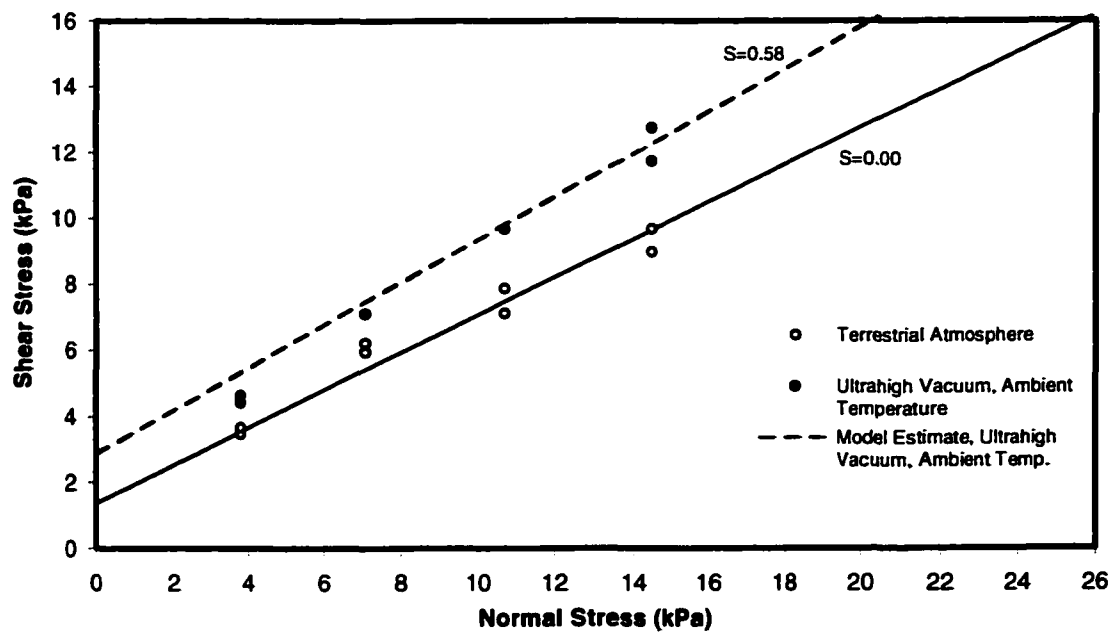

Fig. 3.8 Shear Strength Increases for Enstatite Powder

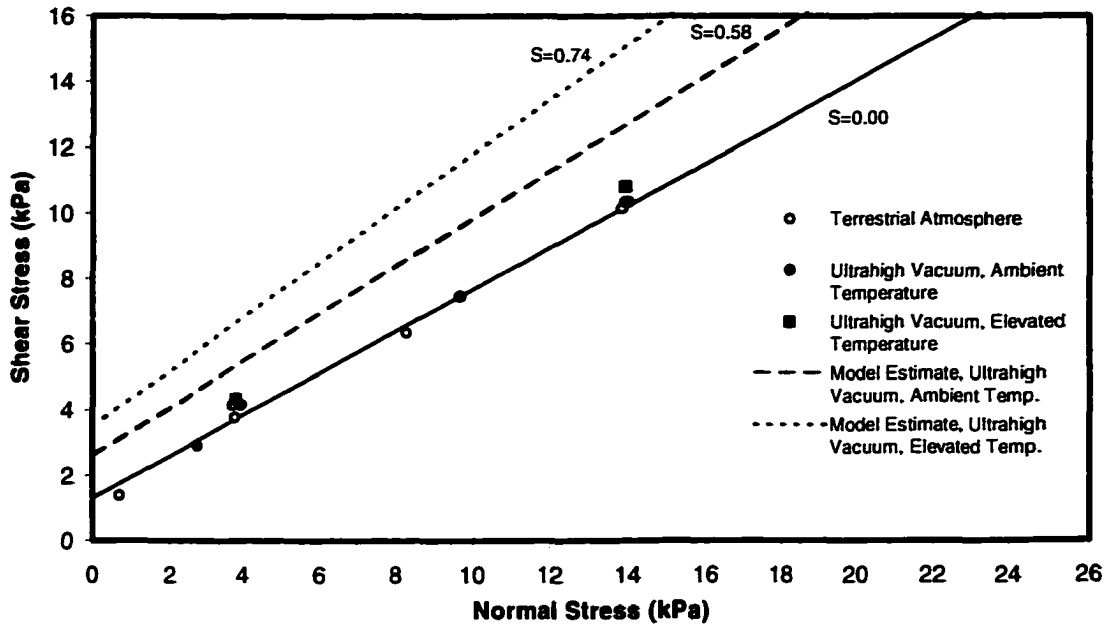

Fig. 3.9 Shear Strength Increases for Olivine Powder

In the surface cleanliness model comparisons, many of the physical-chemical properties of minerals had to be assumed. Additional theoretical study into the solid state chemistry of olivine may result in better correspondence between measured and predicted values.

In the forgoing model for friction and cohesion of particles separated by layers of adsorbed gas, particle deformation was computed based on Hertz theory. However, elastic stresses were omitted in the final static equilibrium analysis. A more correct derivation would be to use the plastic yield stress of the particles.

Based on premises similar those described above, a model for determining dust adhesion to surfaces on any planetary body was presented by Perko (1998). Dust adhesion is governed by phenomena similar to that of surface friction and cohesion, except that both

electrostatic and van der Waals intersurface forces may be important between a dust particle and a nearby surface.

A dust particle clinging to a surface is separated by two layers of adsorbate as shown in Fig. 3.10. The thickness of one layer of adsorbate is governed by the intermolecular potential energy field emitted by the dust particle, and the other is controlled by that of the surface.

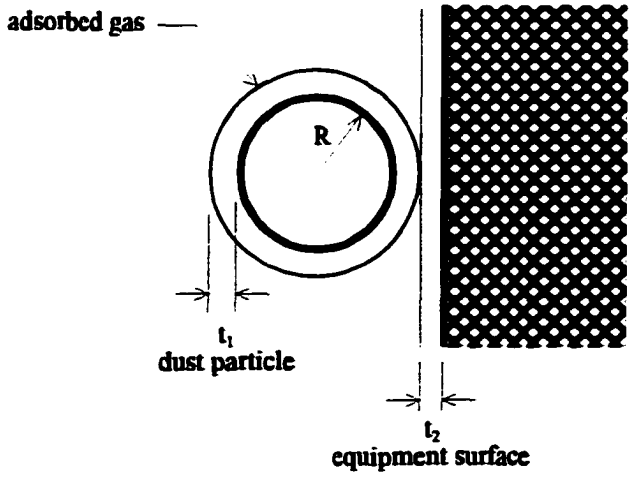

Fig. 3.10 Prior Dust Adhesion Model (Perko, 1998)

In the development of the model it was necessary to slightly redefine surface cleanliness to account for the different compositions of the dust and interacting surface. Like materials, such as a dust particle clinging to a rock, have equal adsorbate thicknesses and their interaction can be described by a single surface cleanliness value. Unlike materials, such as a dust particle attached to a spacesuit, have different adsorbate thicknesses and two surface cleanliness values. The *effective* surface cleanliness that describes their interaction is defined

as the nondimensional inverse of the average adsorbate thickness, given by

$$\bar{S} = \frac{2\Omega}{t_1 + t_2}$$

where t_1 and t_2 are the thicknesses of the adsorbed gas on dust particles and on an interacting solid surface, respectively. On Earth, dust particles have comparatively thick layers of adsorbed gas, low surface cleanliness, and slight adhesion. On comets, the ultrahigh vacuum environment is anticipated to cause higher surface cleanliness and greater dust adhesion.

Van der Waals forces can be accounted for by the Hamaker summation method, which gives the intersurface force between a spherical particle and an infinite half space as (Isrealachvili, 1992)

$$F_{VDW} = \frac{A_V R^*}{6 d^2}$$

where d is the thickness of adsorbate between the dust particle and the surface.

Dust particles may be electrostatically charged, but surfaces such as spacesuits and equipment are typically uncharged. Therefore, Coulomb interactions were assumed to be absent. Electrostatic force resulting from charge-induced dipole interactions are present and may contribute to dust adhesion. This force was volumetrically integrated to obtain the total electrostatic force between an entire dust particle and a material surface. Assuming that the material surface is an infinite half space, the dust particle is spherical, and the radius of the dust particle is much greater than the thickness of adsorbate, the integral is given by

$$F_{ELEC} = \frac{\alpha_p \rho_m \rho_e e^{-\kappa}}{12\pi\epsilon^2\epsilon^2} \left[\ln\left(\frac{2R^*}{d}\right) - 2\right]$$

where α_p is polarizability of the material surface molecule, e is fundamental electron charge and ρ_m and ρ_e are the molecular density of the material surface and the charge density of the dust particle, respectively.

Dust adhesion was determined by the sum of van der Waals and electrostatic interaction. Examination of these equations indicates that dust adhesion increases in direct proportion with dust particle radius. However, mass increases with the cube of particle radius so that large particles are removed easier than small particles by gravity or other accelerations.

Determining surface cleanliness requires knowledge of the environmental properties of a planetary body, as well as the physical-chemical properties of the prevailing dust and engaging surfaces. For atmospheres consisting of a mixture of gasses, the gas component that produces the lowest surface cleanliness governs dust-surface spacing and subsequent adhesive force. Gas types which are adsorbed most easily are water vapor, carbon dioxide, and ammonia. For comets, it is anticipated that water vapor will govern surface cleanliness. Helium adsorption is insignificant even at cold temperatures, because it is a noble gas of low polarizability. Therefore, helium is a suitable gas for use in laboratory experiments where surface cleanliness must be maintained.

Environmental conditions on Mercury and the Moon are conducive to very high surface cleanliness. Greater atmospheric pressure and the presence of water vapor result in the lowest surface cleanliness for Earth. The surface cleanliness on Mars is near that of Earth because of the presence of carbon dioxide and small amounts of water vapor. Venusian

surface cleanliness was comparatively intermediate. Since cometary surfaces are characterized by very low temperatures and considerable water in the form of ice and vapor, surface cleanliness is anticipated to be more similar to Earth than other planetary bodies in the Solar System.

The model was used to determine the adhesive force between dust of various particle diameters and rock, aluminum, titanium, glass, and nylon surfaces. Physical-chemical properties of rock were assumed to be similar to those of dust. A relative permittivity, ϵ, of 80 corresponding to water vapor adsorbate (Israelachvili, 1992) was used to determine electrostatic intersurface force. For clean surfaces (S = 1.0), dust adhesion to a rock surface varied from 3×10^{-7} to 3×10^{-5} N for 5 to 500 μm diameter dust particles, respectively. Dust adhesion forces were approximately 0.3, 0.4, 0.8, and 2.2 times that of rock for glass, nylon, aluminum, and titanium surfaces, respectively. For all materials, electrostatic intersurface forces were insignificant except at very low surface cleanliness values for very large particles compared to the contributions of van der Waals intersurface forces.

The vibrational acceleration required to temporarily detach dust from surfaces was calculated using the relationship force required to overcome adhesion equals dust particle mass times vibrational acceleration (F=ma). Dust particle mass was determined assuming the particles are spherical and using a specific gravity of 3.1 (Johnson, Chua, and Burns, 1995). Peak acceleration required to remove dust of various diameters from a rock surface as a function of surface cleanliness is shown in Fig. 3.11. The acceleration required for removal of dust from glass, nylon, aluminum, and titanium can be approximately determined by multiplying that for rock by 0.3, 0.4, 0.8, and 2.2, respectively.

The approximate effective surface cleanliness values between dust and various surfaces in the environments of several planets are labeled in Fig. 3.11. Dust adhesion on comets is expected to be closest to that of the Earth due to cold temperatures and the presence of water vapor. Examination of the results indicates that the gravitational acceleration of the Earth is sufficient to remove dust particles with diameter greater than about 100 μm in terrestrial atmosphere. Dust smaller than this diameter can not be discerned by the unaided human eye.

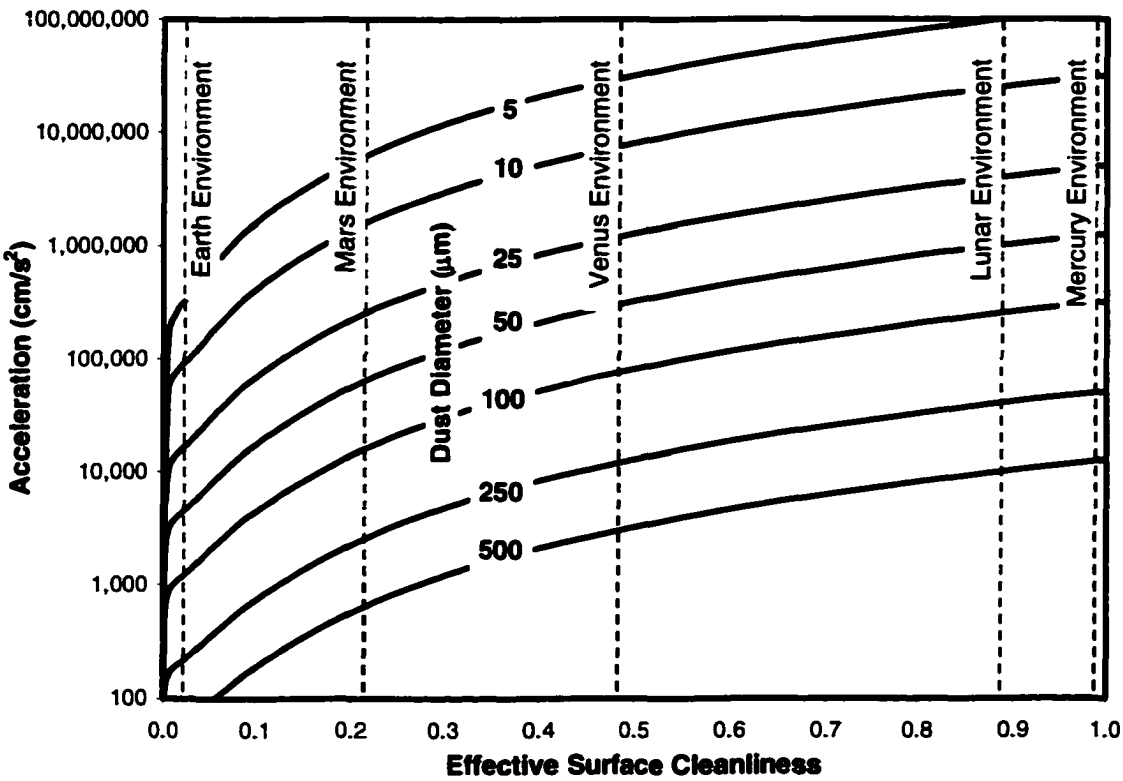

Note: Multiply acceleration by 0.3, 0.4, 0.8, and 2.2 to obtain that required to remove dust from glass, nylon, aluminum, and titanium surfaces, respectively.

Fig. 3.11 Surface Cleanliness Based Dust Adhesion Model (Perko, 1998)

The surface cleanliness based dust adhesion model fails to account for particle and surface deformations. Electrostatic force was derived by a simplistic summation and could be more rigorously derived using modern theories. Effects of capillary condensation was omitted in both of the prior Colorado State University models. To date, a universal theory of dust adhesion that accounts for electrostatic, van der Waals, and capillary forces, deformation of at the contact, the presence of adsorbed layers, mechanical pressure of the adsorbate, and disjoining pressure of dielectric media has not been derived. The development of such a model is necessary to correctly describe dust adhesion in Earth's various environments and in the environments of other planetary bodies in the Solar System.

CHAPTER 4.0 THEORETICAL MODEL

The objective of the theoretical investigation is to develop a model for dust adhesion that incorporates van der Waals, electrostatic, and capillary forces and accounts for elastic particle deformation. Development of the model includes new methods for predicting the thickness of adsorbed gas and the minor radius of a capillary pendular ring between two closely-spaced solid surfaces. Elastic particle contact mechanics are derived based on a superposition of Hertz and Boussinesq penetrator solutions in a procedure similar to that used by Johnson, Kendal, and Roberts (1971). Formulas for computing initial and final contact area and particle indentation depths are provided. The geometric relationship between minor and major radii of a capillary pendular ring for deformed particles separated by adsorbed gas is given. Capillary force is derived. Van der Waals forces are computed using methods similar to Derjaguin, Muller, and Toperov (1975) and electrostatic forces are found using traditional techniques. All of these components are combined into a single closed-form solution for estimating dust adhesion in different planetary environments.

4.1 Adsorption Thermodynamics

Various models have been developed for determining the amount of adsorbed gas on a free solid surface. These include the Langmuir, BET, and Gibbs adsorption isotherms (see

Adamson, 1990 for a review). These models are inappropriate for determination of the thickness of adsorbed gas at and near the contact between a dust particle and a surface or between two dust particles. In these cases, the closeness of the surfaces and their combined influences must be taken into account. The geometry of an adsorbed layer between two closely-spaced solid surfaces is shown in Fig. 4.1. From the viewpoint of a single gas molecule, the opposing surfaces appear to be nearly infinite in extent. Adsorption energy fields have very short range, hence a mathematical model for gas adsorption need only account for solid surfaces immediately surrounding the adsorbed gas. Overall shape of the dust particle outside the contact region is unimportant.

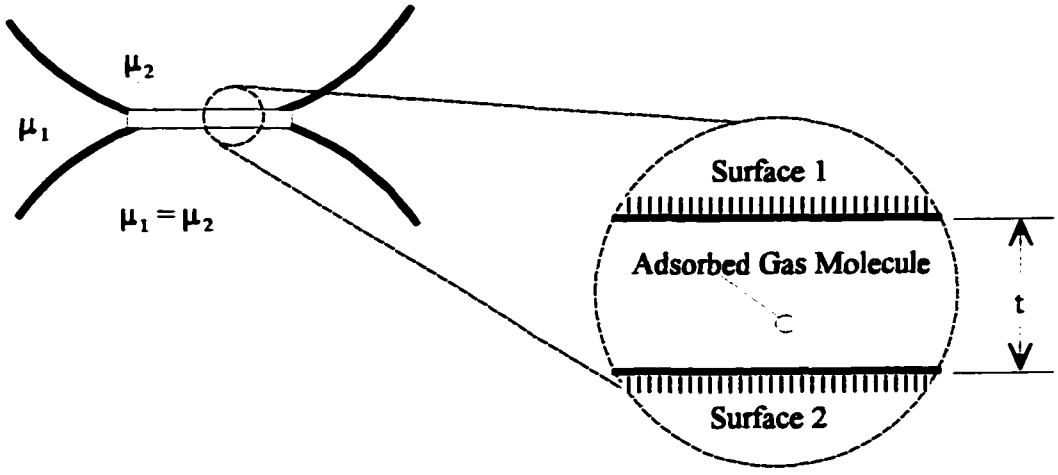

Fig. 4.1 Adsorbed Gas at a Particle Contact

For diffusive thermodynamic equilibrium, the chemical potential everywhere inside a liquid pendular ring must equal that of the ambient gas. Internal chemical potential, μ_1, of a unit volume of ideal gas is given by

$$\mu_1 \frac{t}{V_L} dA = \mu_o \frac{t}{V_L} dA + \frac{RT}{V_L} \ln(\frac{P_o}{P_g}) t dA \quad (1)$$

where μ_o is the chemical potential per mole of the gas in liquid state, R is the Ideal Gas Constant, T is temperature, V_L is specific volume of liquid adsorbate, P_o is vapor pressure, P_g is partial pressure, and t is height of a differential element of adsorbed gas that is being compared to the same quantity of ambient gas (adsorbate thickness between solid surfaces).

Gas adsorbed between solid surfaces has an internal chemical potential equal to μ_o plus an external chemical potential caused by the intermolecular attraction to the adsorbent. Most theoretical models address adsorption energy by examining the interaction of an individual gas molecule with a solid surface. Such considerations do not account for the effect of successive polarization, geometry of the adsorbent, and interference or magnification of adsorption fields between closely-spaced, opposing, solid surfaces. Instead, it is considered here that the change in interaction energy of two solid surfaces with each other due to the presence of adsorbed gas is equal to the energy required to condense and keep the gas between those surfaces.

The interaction energy between solid surfaces involves a combination of van der Waals and electrostatic forces. Opposing solid surfaces exhibit a van der Waals interaction energy per differential area given by (Israelachvili, 1992)

$$U_{vdw} = \frac{A_V}{12\pi t^2} dA \quad (2)$$

where A_v is the Hamaker Coefficient and t is the spacing between surfaces (the adsorbate thickness in this case). The Hamaker Coefficient is a function of the composition of the

adsorbed medium between the surfaces. When the surfaces interact across vacuum or air, the Hamaker Coefficient, A_v, is relatively large and positive indicating strong attraction. When the surfaces interact across a liquid such as adsorbed water, the Hamaker coefficient, A_L, is significantly smaller and can be negative. Hence, the presence of an adsorbed gas layer results in a reduction in van der Waals interaction energy between the two surfaces given by

$$\Delta U_{vdw} = \frac{(A_V - A_L)}{12\pi t^2} dA \tag{3}$$

This energy difference contributes directly to the external chemical potential of the adsorbed gas held between the surfaces.

If the surfaces of the solids are electrostatically charged, then the electric potential also must be taken into account. The geometry of the surfaces and adsorbed layer shown in Fig. 4.1 resembles that of a capacitor. The energy of a capacitor per differential area is given by (Griffiths, 1999)

$$U_{elct} = -\frac{s_1 s_2}{2 \epsilon_o \epsilon} t dA \tag{4}$$

where s_1 and s_2 are the surface charge densities, ϵ_o is the dielectric permittivity of free space, ϵ is relative permittivity, and t is the thickness of the intermediate dielectric (the adsorbate in this case). Relative permittivity of vacuum or dry air is much smaller than the relative permittivity of liquid adsorbate. If it is assumed to be negligible in comparison, then the energy difference of the electrostatic interaction due to the presence of adsorbed gas is approximately equal to the quantity given in Eq. (4).

Adamson (1990) stated that chemical potential of adsorbed films between surfaces

must also include the effect of external stresses and resulting mechanical pressure. Perko, Nelson, and Sadeh (2001) and Perko (1996) showed that adsorption potential of water vapor on mineral particles is sufficiently strong, so that adsorbed water continues to separate solid surfaces even during elastic deformation. According to the definition of work, the energy per differential volume of adsorbate, due to mechanical pressure, is given by

$$U_{pm} = -P_M \, t dA \tag{5}$$

where P_M is mechanical pressure.

Total chemical potential, μ_2, of an adsorbed gas between two surfaces is given by the sum of the internal chemical potential, μ_o, and the external chemical potential given by Eqs. (3), (4), and (5).

$$\mu_2 \frac{t}{V_L} dA = \mu_o \frac{t}{V_L} dA + \frac{(A_V - A_L)}{12\pi t^2} dA - \frac{s_1 s_2}{2\epsilon_o \epsilon} t dA - P_M \, t dA \tag{6}$$

Equilibrium adsorbate thickness can be found by setting Eq. (1) equal to Eq. (6) and solving for t. The solution has three roots of t, two imaginary and one real. The real root is given in Eq. (8).

$$\frac{RT}{V_L} \ln\left(\frac{P_o}{P_g}\right) t = \frac{(A_V - A_L)}{12\pi t^2} - \frac{s_1 s_2}{2\epsilon_o \epsilon} t - P_M \, t \tag{7}$$

$$t = \left[\frac{\dfrac{(A_V - A_L)}{12\pi}}{\dfrac{RT}{V_L} \ln\left(\dfrac{P_o}{P_g}\right) + \dfrac{s_1 s_2}{2\epsilon_o \epsilon} + P_M}\right]^{1/3} \tag{8}$$

Adsorbed water thickness was computed between two closely spaced electrostatically neutral, quartz surfaces using Eq. (8). The computation assumed standard room temperature. Results are shown in Fig. 4.2. The upper solid curve was computed with no external mechanical pressure acting on the adsorbate ($P_M = 0$). The lower dashed curve was computed by setting the mechanical pressure equal to 444 MPa, which is the Brinell hardness of quartz. As can be seen in the figure, the effect of mechanical pressure is a reduction in the thickness of adsorbed water between surfaces. The computation indicates that a mechanical pressure equal to the hardness of quartz is sufficient to reduce the thickness of adsorbed gas to less than a monolayer of water (1.4 Å) at about 1% humidity, whereas, an unpressurized adsorbate can exist above monolayer thickness at low to moderate vacuum conditions.

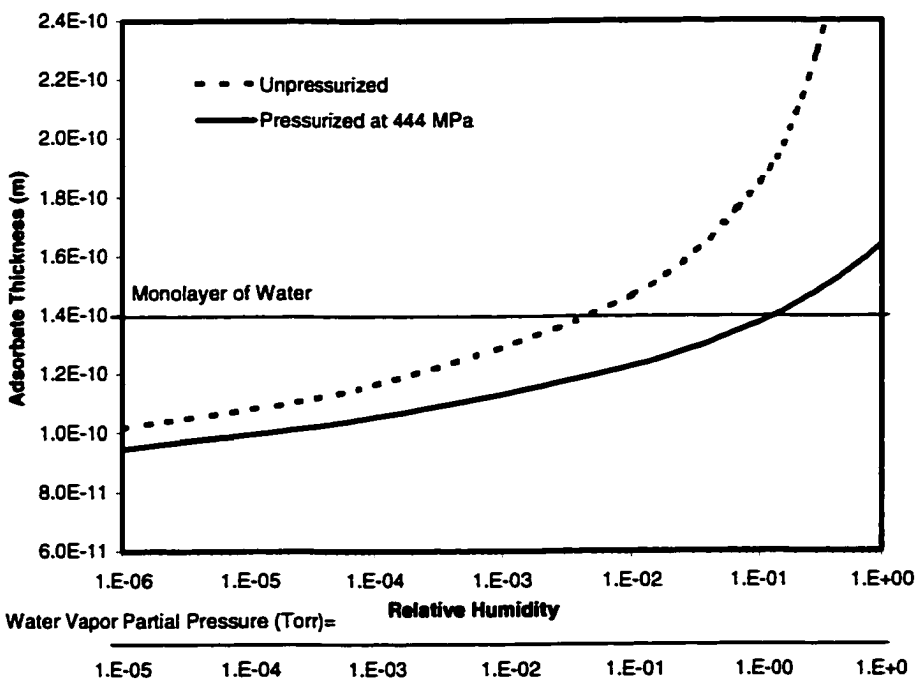

Fig. 4.2 Example Adsorbed Gas Thickness Computation

An examination of the limits of Eq. (8) indicates that the proposed formula for adsorbate thickness determination generally matches other more well-known theories. Setting mechanical pressure to zero and taking the limit of Eq. (8) as relative humidity approaches saturation ($P_g \rightarrow P_o$) results in Eq. (9), which closely resembles DLVO colloid theory for aqueous suspensions of particles where van der Waals attraction is balanced by electric double-layer repulsion (Derjaguin and Landau, 1948 and Verwey and Overbeek, 1948).

$$\frac{s_1 s_2}{2\epsilon_o \epsilon} t = \frac{(A_V - A_L)}{12\pi t^2} \tag{9}$$

Setting electrostatic surface charge density equal to zero and taking the limit of Eq. (8) as t becomes large relative to the range of van der Waals forces results in Eq. (10), which is the familiar Kelvin equation for capillary pressure, as given by

$$\frac{RT}{V_L} \ln\left(\frac{P_o}{P_g}\right) = - P_M \tag{10}$$

where the negative sign indicates tension within the adsorbed layer.

Substitution of the Young-Laplace relationship ($P_M = - \gamma_{LV}/r_s$), which relates mechanical pressure across a liquid-vapor interface with the surface tension and radius of curvature of a liquid, into Eq. (10) provides an approximate means for computing the curvature of a liquid pendular ring as a function of relative humidity (P_g/P_o) and temperature. Particles and surfaces in environments with low humidity are separated by small pendular rings with very small radii of curvature. Under these conditions, the curvature of the pendular ring should be affected by the same energy fields that cause adsorption. Derjaguin (1936) introduced and termed this effect the disjoining pressure, Π, and suggested that it is due to

van der Waals energy fields, electric double layers, adsorbed ions, and alteration of liquids between surfaces.

A new method for determining the minor radius of curvature, r_s, of a small pendular ring between two particles that accounts for van der Waals and electric double layer components of disjoining pressure can be developed from the condition of diffusive equilibrium and equality of chemical potentials, as in Eqs. (7) and (8). Moreover, if mechanical pressure is replaced by the negative of liquid-vapor surface energy, γ_{LV}, divided by capillary radius, r_s, in accordance with the aforementioned Young-Laplace relationship, and if the pendular ring is small compared to dust particle and solid surface asperities, then the spacing between surfaces, t, is approximately equal to the minor diameter of the capillary, $2r_s$. Making these substitutions in Eq. (8) and solving for r_s yields four roots. The minor radius of curvature is the real, non-zero root given by

$$r_s = \frac{H_3 + 64\,\gamma_{LV}^2\,H_3^{-1} + 4\,\gamma_{LV}}{12\,H_1} \tag{11}$$

where

$$H_1 = \frac{R\,T}{V_L}\ln\left(\frac{P_o}{P}\right) + \frac{S_1\,S_2}{2\,\epsilon_o\epsilon} \tag{12}$$

$$H_2 = \frac{9\,(A_V - A_L)}{4\,\pi}\,H_1^2 \tag{14}$$

$$H_3 = \left[\,4\,H_2 + 64\,\gamma^3 + 12\left(\frac{A_V - A_L}{4\,\pi}(H_2 + 32\gamma_{LV}^3)\right)^{1/2} H_1\,\right]^{1/3} \tag{13}$$

The coefficients H_1, H_2, and H_3 are named the linear, quadratic, and polynomial gap potentials due to their respective dependence on chemical potential of gasses in the ambient

environment.

By accounting for van der Waals and electric double layer potentials between opposing closely-spaced surfaces, a capillary pendular ring is more stable at lower pressure and lower relative humidity than is predicted using only the Young-Laplace and Kelvin Equations. An example comparison between the two methods is shown in Fig. 4.3 for a meniscus of pure water between electrostatically neutral quartz surfaces at standard room temperature. At high humidity, the two methods yield essentially the same results, while, at low humidity, the two methods diverge. The smallest possible radius of curvature of a water capillary meniscus at very low humidity is the radius of a single water molecule (0.7 Å). The new model, Eqs. (11) through (14), indicates that a water meniscus of this radius is viable at moderate to high vacuum, whereas, the Young-Laplace and Kelvin Equations, without consideration of disjoining pressure, preclude a monomolecular water meniscus except above about 0.1% relative humidity.

When the solid surfaces bounding a capillary pendular ring are similarly charged (electrostatic repulsion), the radius of curvature predicted by the new model is less than that predicted by the Young-Laplace and Kelvin Equations at high humidity, as shown in Fig. 4.4. The new model also predicts a finite capillary radius at the limit where the partial pressure approaches the vapor pressure (100% relative humidity). The Young-Laplace and Kelvin Equations predict an infinite capillary radius at this limit.

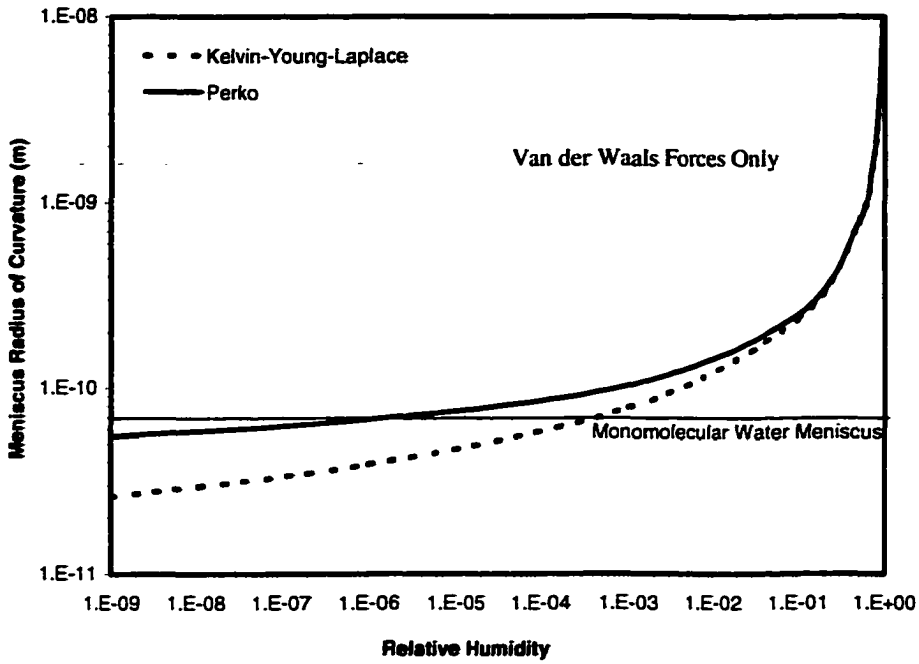

Fig. 4.3 Capillary Radius Between Quartz Plates at Low Humidity

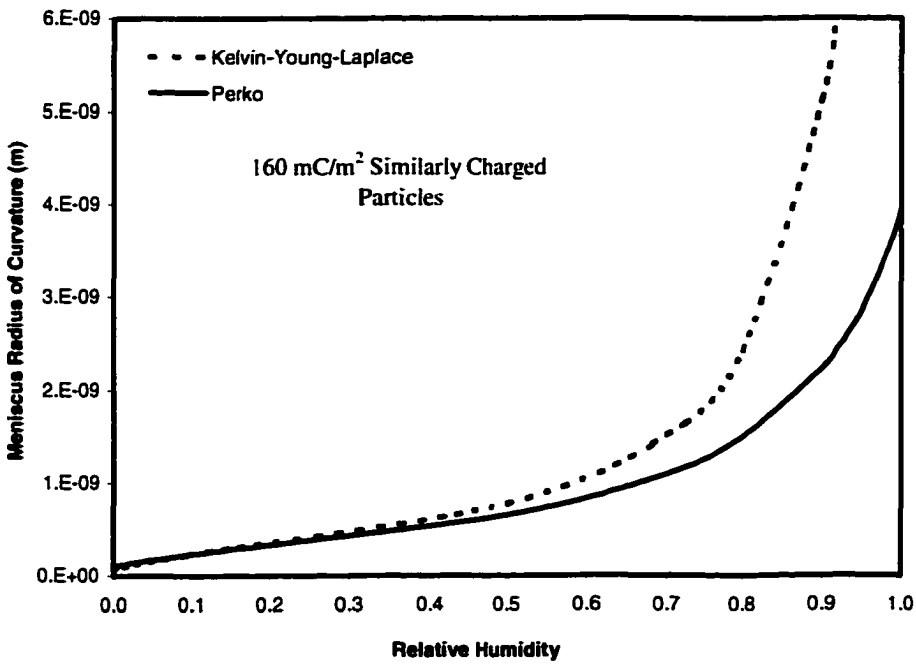

Fig. 4.4 Capillary Radius Between Equally Charged Particles

When the solid surfaces bounding the capillary pendular ring are oppositely charged (electrostatic attraction), an interesting phenomenon is predicted by the new model as shown in Fig. 4.5. As can be seen in the figure, the new model predicts that the radius of curvature is discontinuous at a certain degree of humidity. Furthermore, the sign of the radius of curvature depends on whether that point is approached from the saturation side or the dry side. A surface charge density of 160 mC m^{-2} was used to construct both Figs. 4.4 and 4.5. This is the surface charge density reportedly associated with montmorillonite clay particles (Yong and Warkentin, 1966).

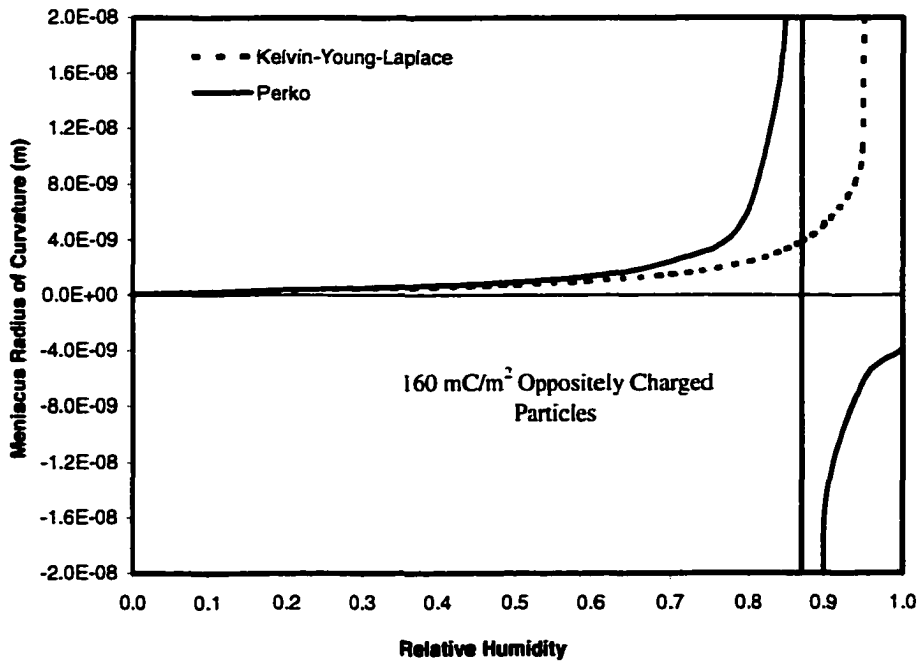

Fig. 4.5 Capillary Radius Between Oppositely Charged Particles

4.2 Particle Mechanics

In the DMT adhesion model, van der Waals force is treated as a body force that is balanced by classical Hertz deformation in order to predict contact area. Integration of surface stresses over area yields a finite resultant force. At a distance from the contact, it appears that some external force is being applied to the surface as if the particle were being pushed against it. This treatment of surface stress is incorrect. It is more realistic to treat van der Waals forces as tensile surface stresses and to superimpose them with Hertz contact stresses. In this manner, compressive and tensile stresses, although applied at different locations, cancel, and integration of stress over surface area is equal to zero at equilibrium when the particle is at rest. In other words, the particle is pulling and pushing on a surface in equal amounts so that, at a distance, no net external force is being applied. In mathematical terms, the DMT model violates the Gauss Law which states that the integral of surface stress over the entire area of a sphere, drawn at a sufficient distance from the particle contact so that all inter-body forces are contained within the sphere, must equal zero if no net external force is being applied.

$$\oint \sigma \, dA = 0 \qquad or \qquad \nabla \cdot \sigma = 0 \tag{15}$$

The JKR model uses a superposition of cylindrical punch-type tensile stresses (originally derived by Boussinesq, 1885) and spherical penetrator-type compressive stresses (originally derived by Hertz, 1881). This superposition is a more correct interpretation of particle mechanics and satisfies the Gauss Law. The JKR model has been criticized because it predicts infinite tensile stress at the periphery of the contact area. Fisher-Cripps (2000) explains that plastic yielding maintains stresses within finite limits. The JKR model also has

been criticized because it fails to account for long range van der Waals forces acting outside of the contact area. Since van der Waals forces are of negligible strength at small distances from the contact, a stress distribution that has very high tensile stresses along the periphery of the contact is a close approximation. In this section, the governing equations for elastic deformation of two curved surfaces in contact are derived following a similar strategy to that used in the JKR model. Methods of determining equilibrium contact radius, contact radius at the instant of particle removal, distance of approach of the surfaces due to elastic deformation, and total stored elastic energy are provided. In a later section, the energy of long range interparticle forces outside, but near the perimeter, of the contact area and the energy of a capillary pendular ring are incorporated to find adhesion.

The proposed model consists of two curved surfaces with a liquid pendular ring surrounding their contact, as shown in Fig. 4.6. Since van der Waals forces are considerably decreased by the presence of liquid in the pendular ring, they are strongest just outside of its perimeter. According to the free body diagram for a liquid-solid-gas interface provided in Chapter 3, capillary forces are strongest along the perimeter of the pendular ring as well. Capillary and van der Waals tensile stresses cause a Hertzian contact area to develop within the center of the pendular ring.

In the following derivation, -F is defined as the total van der Waals and capillary tensile force in the Boussinesq cylindrical punch solution. The radius of the cylindrical punch is set equal to the azimuthal radius of the pendular ring so that the highest concentration of tensile stress is along the perimeter of the pendular ring. The total compressive force in the Hertz spherical punch solution is set equal to αF where α is defined as the ratio of tensile to

compressive force. By this notation, the stresses are in equilibrium when $\alpha = 1$. Boussinesq and Hertz solutions are superimposed to find the final state of surface stress. Thus, the proposed model differs from the JKR model, since major tensile stresses are applied outside the contact area rather than within it.

The distribution of Hertz-type compressive surface stress within the contact region between two curved surfaces being forced together is given by (Fisher-Cripps, 2000)

$$\sigma_{zh} = \frac{3}{2} \frac{\alpha F \sqrt{1-\frac{\rho^2}{a^2}}}{\pi a^2} \tag{16}$$

where ρ is the radial coordinate of distance from the central axis of the contact and a is the contact radius. The distribution of Boussinesq-type tensile surface stress within the pendular ring is given by (Fischer-Cripps, 2000)

$$\sigma_{zp} = -\frac{1}{2} \frac{F}{\pi r_c^2 \sqrt{1-\frac{\rho^2}{r_c^2}}} \tag{17}$$

Superposition of these two stress distributions results in

$$\sigma_z = \frac{1}{2} F \frac{3 \alpha \sqrt{(a^2-\rho^2)(r_c^2-\rho^2)} - a^3/r_c}{\pi a^3 \sqrt{r_c^2-\rho^2}} \qquad \rho \le a \tag{18}$$

$$\sigma_z = -\frac{1}{2} \frac{F}{\pi r_c^2 \sqrt{1-\frac{\rho^2}{r_c^2}}} \qquad r_c \ge \rho > a \tag{19}$$

As external force is applied to remove the particle from the curved surface, the ratio

of compressive stress to tensile stress will decrease. At some ratio, α_f, the net compressive stress will equal zero and the integral of all tensile stresses over the entire area will exactly balance the removal force. At this point the surfaces should spontaneously separate or "jump" apart. The critical force ratio, α_f, at the instant the particle is removed was found by integrating compressive stresses over the surface, setting the resulting net compressive force equal to zero, and solving for α.

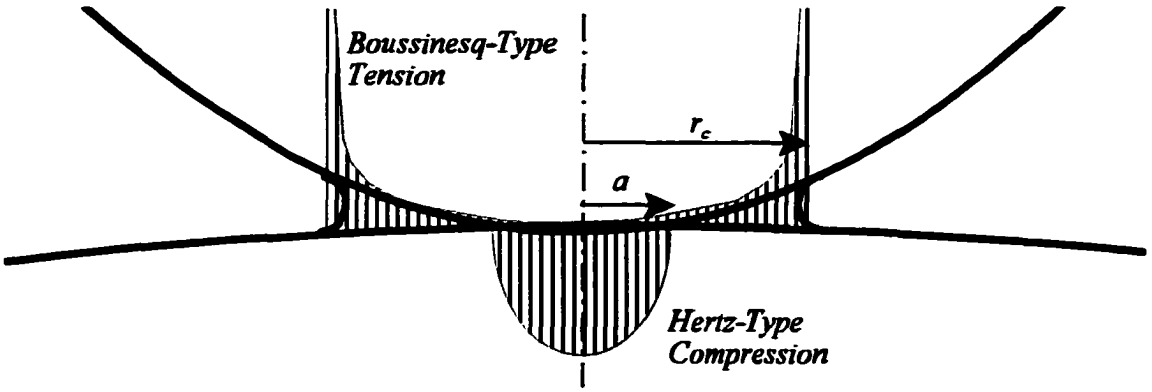

Fig. 4.6 Distribution of Surface Stress at a Particle Contact

In order to integrate compressive stresses, the distance from the central axis of the particle contact, ρ, to the point where compressive stresses transition to tensile stresses, X, must be found. Since Boussinesq-type tensile stresses are small but not zero within the contact area, the distance X is slightly less than the contact radius, a. The solution for X can be determined by solving for ρ where the superimposed surface stress, Eq. (18), is equal to zero. This calculation results in four roots. All roots are the same magnitude but have different signs. The correct transition point is either of the positive roots given by

$$X = \left(\frac{3a^2\alpha^2r_c^2 + 3\alpha^2r_c^4 + \sqrt{\alpha^2r_c^2\,(9a^4\alpha^2r_c^2 - 18a^2\alpha^2r_c^4 + 9\alpha^2r_c^6 + 4a^6)}}{6\alpha^2r_c^2}\right)^{1/2} \quad (20)$$

The total compressive force, F_{cmp}, experienced by the surface and the particle is the integral of Eq. (18) over the entire area from the central axis to the transition point, X, given by

$$F_{cmp} = \int_0^X 2\,\pi\,\sigma_z\,\rho\,d\rho =$$

$$\alpha F - F - \frac{\sqrt{6}}{36}F\alpha\left(\frac{3a^2\alpha^2r_c^2 - 3r_c^4\alpha^2 - \sqrt{\alpha^2r_c^2(9a^4\alpha^2r_c^2 - 18a^2\alpha^2r_c^4 + 9r_c^6\alpha^2 + 4a^6)}}{a^2\alpha^2r_c^2}\right)^{3/2} + \quad (21)$$

$$\frac{\sqrt{6}}{6}F\left(\frac{-3a^2\alpha^2r_c^2 + 3r_c^4\alpha^2 - \sqrt{\alpha^2r_c^2(9a^4\alpha^2r_c^2 - 18a^2\alpha^2r_c^4 + 9r_c^6\alpha^2 + 4a^6)}}{\alpha^2r_c^4}\right)^{1/2}$$

The critical force ratio, α_f, is the ratio, α, that results in a total compressive force, F_{cmp}, equal to zero. The resultant critical ratio is given by Eq. (22). Conveniently, the majority of terms cancel from the equation including the tensile force, -F.

$$\alpha_f = \frac{1}{3}\left(\frac{a}{r_c}\right)^2 \quad (22)$$

Within the contact area, Hertz type compressive deformation of the particle is given by (Fischer-Cripps, 2000)

$$u_{zhl} = \frac{3}{8}\frac{(1-\nu_1^2)\,\alpha\,F\,(2a^2 - \rho^2)}{a^3\,E_1} \quad (23)$$

where E_1 is the Young Modulus and ν_1 is the Poisson Ratio of the particle. Similarly, within the contact area, Hertz deformation of the curved surface upon which the particle rests is given by (Fischer-Cripps, 2000)

$$u_{zh2} = \frac{3(1-\nu_2^2)\,\alpha\,F\,(2a^2 - \rho^2)}{8\,a^3\,E_2} \tag{24}$$

where E_2 is the Young Modulus and ν_2 is the Poisson Ratio of the surface.

Within the pendular ring, Boussinesq-type tensile deformation of the particle is given by (Fischer-Cripps, 2000)

$$u_{zp1} = -\frac{1}{2}\frac{(1-\nu_1^2)\,F}{r_c\,E_1} \tag{25}$$

and that of the surface is given by (Fisher-Cripps, 2000)

$$u_{zp2} = -\frac{1}{2}\frac{(1-\nu_2^2)\,F}{r_c\,E_2} \tag{26}$$

If a particle and a surface are linearly elastic, then surface deformations can be superimposed. Examples of the equilibrium deformed shapes of spherical particles in contact with a flat surface ($R_2 = \infty$) for different ratios of r_c/a in accordance with this superposition are shown in Fig. 4.7. It can be seen in this figure that the model allows for simulation of deformed particle shapes similar to that measured using interferometry by Fisher and Israelachvili (1981a and 1981b). Since surface deformation due to the cylindrical punch solution is uniform everywhere within the pendular ring, superposition of Eqs. (23) and (25) does not change the Hertz contact radius, given by (Johnson, 1985)

$$a = \frac{1}{2}\left(\frac{6\,\alpha\,F\,R^*}{E^*}\right)^{1/3} \tag{27}$$

The effective radius of curvature, R*, is defined as

$$R^* \equiv \frac{R_1 R_2}{R_1 + R_2} \tag{28}$$

where R_1 and R_2 are the radii of curvature of the particle and surface, respectively. The effective elastic constant, E*, is defined as

$$E^* \equiv \frac{1}{\frac{1-\nu_1^2}{E_1} + \frac{1-\nu_2^2}{E_2}} \tag{29}$$

Net movement, δ, of a dust particle toward a fixed surface or of two particles toward each other due to combined particle and surface deformations can be obtained by adding Eqs. (23) through (26) and evaluating their sum at the central point of contact where ρ=0. The end result is given by

$$\delta = \frac{F\,(2\,a - 3\,\alpha\,r_c)}{4\,E^*\,a\,r_c} \tag{30}$$

Dry Environment, $r_s/a = 1$

Wet Environment, $r_s/a >> 1$

Fig. 4.7 Shape of a Particle and Surface Contact

With the superimposed stresses and deformations, it is possible to determine the stored elastic energy, U_e, of the contact by integrating the product of surface stress and surface deformation over the pendular ring area for both interacting solids, as given below. It is necessary to perform the integration over separate intervals from 0 to a and from a to r_c. Surface deformations due to the Hertz solution outside the contact area were assumed to be negligible compared to those due to the Boussinesq solution. Also, surface deformations outside the capillary pendular ring due to the Boussinesq solution were assumed to be negligible since they are counteracted, in large part, by deformations in the opposite direction due to the Hertz solution. The end result of the integration is given by

$$U_e = \int_0^a 2\pi\ \sigma_z\ u_{z1}\ \rho d\rho + \int_0^a 2\pi\ \sigma_z\ u_{z2}\ \rho d\rho + \int_a^{r_c} 2\pi\ \sigma_z\ u_{zp1}\rho d\rho + \int_a^{r_c} 2\pi\ \sigma_z\ u_{zp2}\rho d\rho = F^2\ \frac{-30\alpha r_c a^2+24\alpha^2 a^2 r_c+25\alpha a^2\sqrt{r_c^2-a^2}+20a^3-10r_c^2\alpha\sqrt{r_c^2-a^2}-20a^3\alpha+10r_c^3\alpha}{40E^* r_c a^3} \quad (31)$$

where u_{z1} and u_{z2} are the superimposed deformations due to Hertz and Boussinesq solutions for each surface, as given in Eqs. (23) through (26).

The equation for contact radius, Eq. (27), can be solved for F in terms of a. Substitution of the result into Eq. (31) gives the stored elastic energy in terms of independent variables a, α, and E* only. Furthermore, final contact radius can be written in terms of the critical force ratio, α_f, in order to yield the stored elastic energy at the instant of particle removal given by

$$U_{ef} = \frac{r_{cf}^5 E^*}{R^{*2}}\ \frac{2\sqrt{3\alpha_f}}{15}\ (\sqrt{1-3\alpha_f}(75\alpha_f-10)\ +72\alpha_f^2\ -90\alpha_f\ +10\ +60\sqrt{3}(\alpha_f^{1/2}-\alpha_f^{3/2}) \quad (32)$$

In order to simplify Eq. (32), the portion of the equation, which is strictly a function of α_f, is plotted in Fig. 4.8. From geometric constraints and Eq. (22), the critical force ratio, α_f, varies from 0 to 1/3. A simpler expression that approximates the portion of Eq. (32) that is a function of α_f is graphically represented by the dashed line in Fig. 4.8.

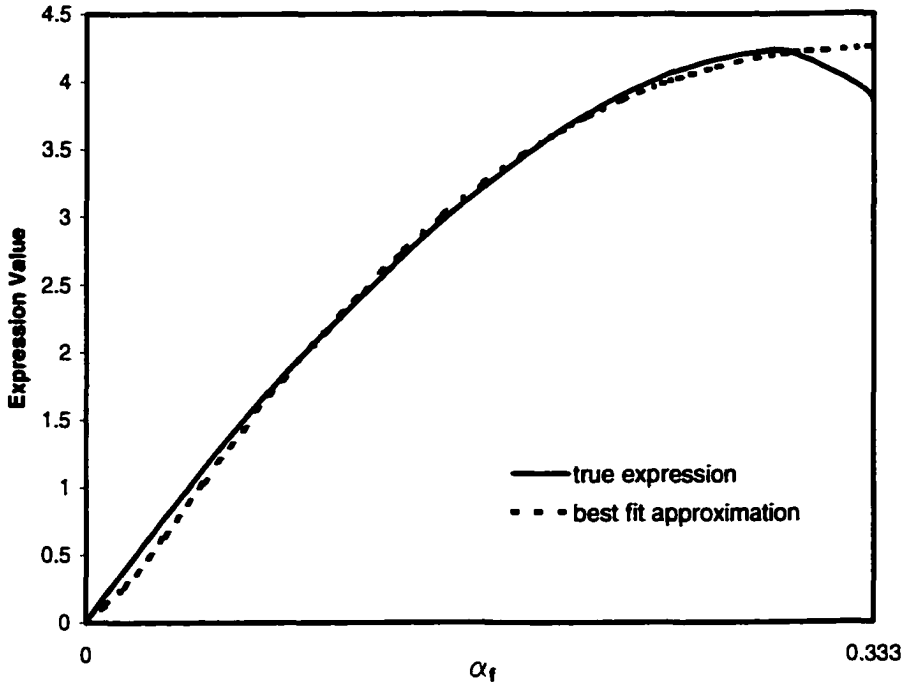

Fig. 4.8 Stored Elastic Energy Approximation

Insertion of the simpler expression into Eq. (32) results in an approximate stored elastic energy given by

$$U_{ef} \approx -\frac{r_{ef}^5 E^*}{R^{*2}} \frac{17}{4}(3\alpha_f - \sqrt{12\alpha_f})^3 \qquad (33)$$

By combining contact mechanics Eqs. (22), (27), and (30), the distance of approach can be expressed in terms of α_f, as given by

$$\delta_f = \frac{r_{cf}^2}{R^*}(3\alpha_f - \sqrt{12\alpha_f}) \tag{34}$$

Substitution of Eq. (34) into Eq. (33) results in

$$U_{cf} \approx -\frac{17\,R^*\,E^*}{4\,r_{cf}}\,\delta_f^3 \tag{35}$$

4.3 Capillary Force

All real surfaces exhibit some degree of roughness and local curvature. Hence, they typically interact through a series of discrete contacts. Each contact can be mathematically modeled as two opposing parabaloids of different focal lengths where each focal length is equal to one-half the radius of local curvature. Since adhesion forces are short range, the parabaloid model is a good approximation for interactions involving spherical particles. A spherical particle resting on a smooth flat plane can be modeled by setting the focal length of one of the parabaloids equal to infinity, and a spherical particle resting in a depression on a surface can be modeled using a negative focal length for the surface. The parabaloid approximation was used by Hertz in the development of the contact mechanics equations referenced in §4.2 and by Derjaguin in the derivation of van der Waals force between spheres which is discussed in §4.4. The same approximation is used herein to examine the geometry of a capillary pendular ring between two opposing curved surfaces and to compute the capillary adhesion force.

The geometry of a liquid capillary pendular ring between two curved parabaloid surfaces is shown in Fig. 4.9. To date, formulas relating the azimuthal radius, r_c, of a pendular

ring with the minor capillary radius, r_s, have not been developed for the case where the curved surfaces are elastically deformed and separated by a layer of adsorbed gas. An approximate relationship can be derived based on the simple geometry shown in the figure.

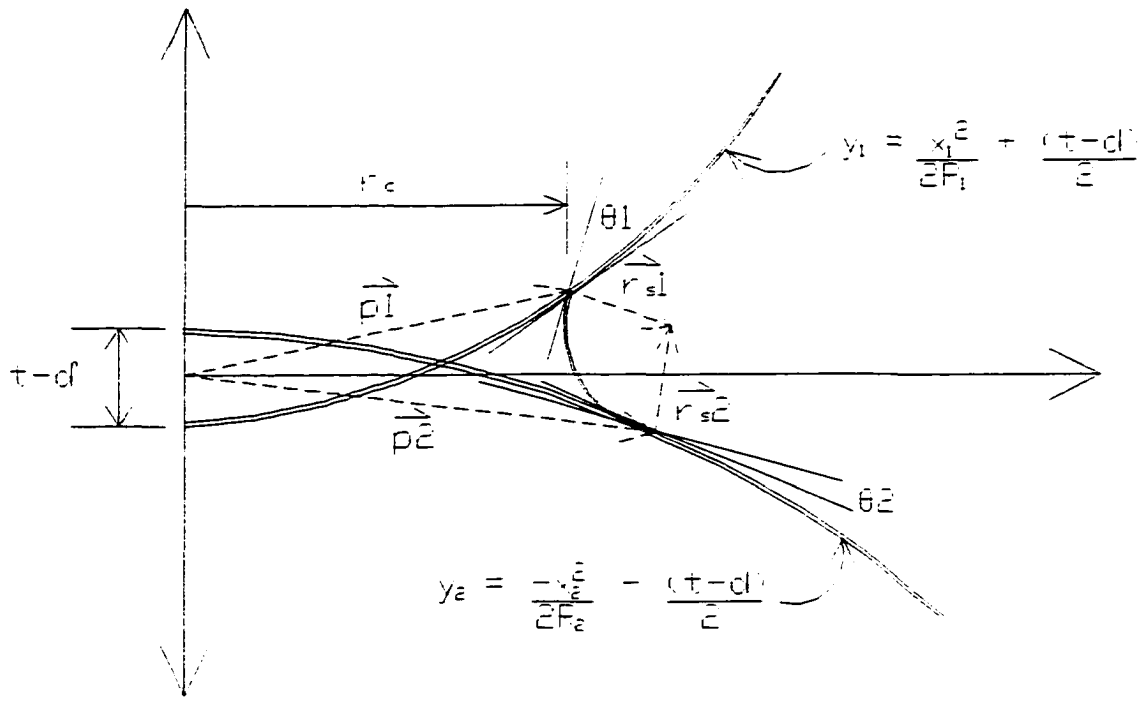

Fig. 4.9 Capillary Pendular Ring Geometry

The separation between the parabaloids in Fig. 4.9 is equal to the adsorbate thickness, t, minus the distance of approach, δ. For particles in adhesive contact, the later distance is positive and is typically greater than the adsorbate thickness. Thus, at equilibrium, the parabaloids overlap as shown in the figure. The vector, **p1**, from the origin of the axis to the point at which the meniscus intercepts the upper surface is given by

$$\boldsymbol{p1} = x_1\,\hat{x} + \left(\frac{x_1^2}{2\,R_1} + \frac{(t-\delta)}{2}\right)\hat{y} \qquad (36)$$

Similarly, the vector, **p2**, from the origin to the lower surface is given by

$$p2 = x_2\,\hat{x} - \left(\frac{x_2^2}{2R_2} + \frac{(t-\delta)}{2}\right)\hat{y} \tag{37}$$

Slopes of the upper and lower parabaloids at the intersections with the meniscus are found by taking the derivative of the equations for the surfaces, y_1 and y_2, with respect to x and evaluating the solutions at the points x_1 and x_2, respectively.

$$m1 = \frac{d}{dx_{x=x_1}}\left(\frac{x^2}{2R_1} + \frac{(t-\delta)}{2}\right) = \frac{x_1}{R_1} \tag{38}$$

$$m2 = \frac{d}{dx_{x=x_2}}\left(-\frac{x^2}{2R_2} - \frac{(t-\delta)}{2}\right) = -\frac{x_2}{R_2} \tag{39}$$

The contact angle of water with metal, glass, and most mineral surfaces is small. By assuming that the contact angles, as shown by $\theta 1$ and $\theta 2$ in the figure, are equal to 0, expressions for the vectors from the surface-meniscus intersection points to the center of minor curvature, defined as $\mathbf{r_s1}$ and $\mathbf{r_s2}$ in the figure, are easily determined. With zero contact angle, the slopes of $\mathbf{r_s1}$ and $\mathbf{r_s2}$ are equal to negative reciprocals of Eqs. (38) and (39). By considering that their lengths are equal to the minor radius of the capillary, r_s, vectors $\mathbf{r_s1}$ and $\mathbf{r_s2}$ are then given by

$$\mathbf{r_s1} = \frac{r_s x_1}{(R_1^2 + x_1^2)^{1/2}}\,\hat{x} - \frac{r_s R_1}{(R_1^2 + x_1^2)^{1/2}}\,\hat{y} \tag{40}$$

$$\mathbf{r_s2} = \frac{r_s x_2}{(R_2^2 + x_2^2)^{1/2}}\,\hat{x} + \frac{r_s R_2}{(R_2^2 + x_2^2)^{1/2}}\,\hat{y} \tag{41}$$

Provided the pendular ring is small in comparison with the size of the particle, the squares of

the radial dimensions of the capillary pendular ring, x_1^2 and x_2^2, are much smaller than the squares of the radii of curvature of the particle and the surface, R_1^2 and R_2^2. With this assumption, Eqs. (40) and (41) can be simplified as follows.

$$\mathbf{r_s1} = \frac{r_s x_1}{R_1}\hat{x} - r_s\hat{y} \tag{42}$$

$$\mathbf{r_s2} = \frac{r_s x_2}{R_2}\hat{x} + r_s\hat{y} \tag{43}$$

The position coordinates of the meniscus intersection with the upper and lower surfaces can be obtained by setting the sum of vectors **p1** and $\mathbf{r_s1}$ equal to the sum of vectors **p2** and $\mathbf{r_s2}$. If the vectors are separated into x and y components, then their summation is given by

$$\sum_x: \quad x_1 + \frac{r_s x_1}{R_1} = x_2 + \frac{r_s x_2}{R_2} \tag{44}$$

$$\sum_y: \quad \frac{x_1^2}{2R_1} + \frac{t-\delta}{2} - r_s = -\frac{x_2^2}{2R_2} - \frac{t-\delta}{2} + r_s \tag{45}$$

By assuming the minor capillary radius, r_s, is much smaller than the radii of curvature of the particle and the surface, R_1 and R_2, then Eq. (44) can be simplified to yield the following approximate relationship.

$$x_1 \approx x_2 \tag{46}$$

Hence, the radial extents of the pendular ring, x_1 and x_2, can be represented by a single parameter, namely the azimuthal radius, r_c. Making this substitution in Eq. (45) results in

$$\frac{1}{2} r_c^2 \left(\frac{1}{R_1} + \frac{1}{R_2}\right) = 2r_s + \delta - t \tag{47}$$

Incorporating the definition of effective radius of curvature of the surfaces, R*, given by Eq. (28), and solving for r_c in Eq. (47) yields the sought after geometric relationship between r_s and r_c for elastically deformed curved surfaces interacting across a layer of adsorbed gas given by

$$r_c = (2 R^* (2 r_s + \delta - t))^{1/2} \quad (48)$$

The above relationship is valid provided $2r_s$ is greater than $t - \delta$. Examination of contact mechanics Eqs. (27) and (30) reveals that upon application of an external removal force (α decreases), the value of δ transitions from a positive quantity at equilibrium ($\alpha=1$) to a negative quantity at the critical point of surface separation ($\alpha_f=1/3(a/r_c)^2$). The diagram in Fig. 4.10 depicts the case where parabaloids are being pulled apart and δ is a negative number. The pendular ring drawn outside the contact area has a capillary radius, r_c, of sufficient size that it satisfies the criteria that $2r_s$ is greater than $t - \delta$. Hence, Eq. (48) is valid for this case. The edge of the particle contact, which is at a distance a from the central axis of the parabaloids, marks the transition point where the distance that separates the two curved surfaces, $2r_s$, ceases to be greater than $t - \delta$. This geometric constraint imparts an important boundary condition that the azimuthal radius of the pendular ring must be greater than or equal to the contact radius.

$$r_c \geq a \quad (49)$$

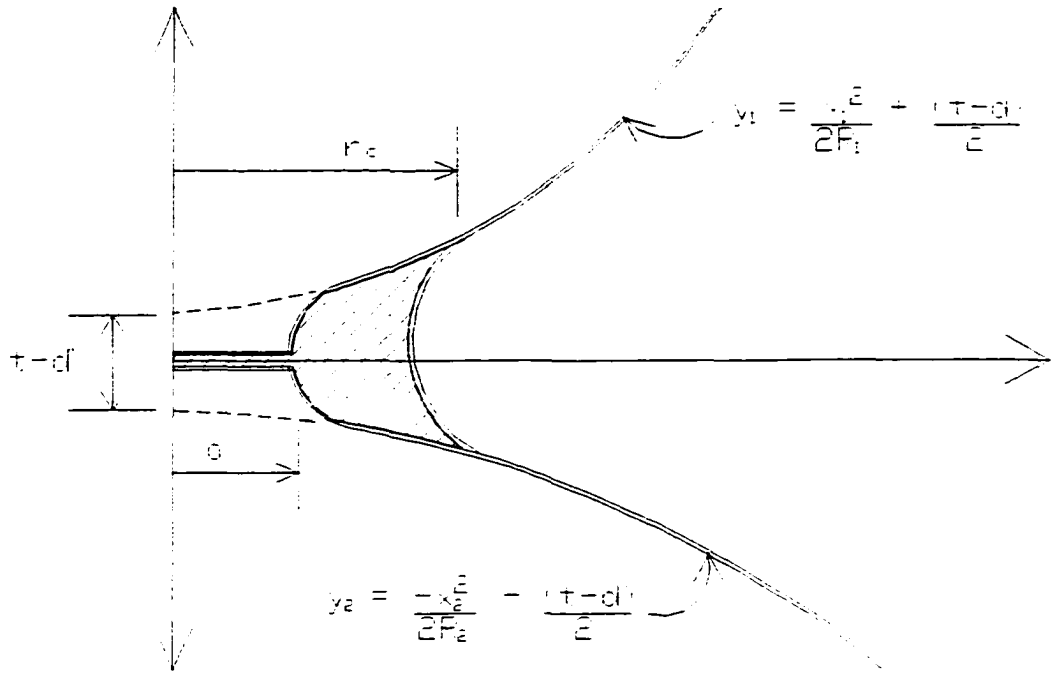

Fig. 4.10 Pendular Ring between Parabaloid Surfaces under Tension

In order to evaluate the influence of a liquid capillary on the elastic contact between two curved surfaces and on particle adhesion, the surface energy (or surface tension) of the pendular ring must be considered. When surfaces are being pulled apart, it is typically assumed that diffusion is slow and that the volume of the capillary ring remains constant. Past models for predicting capillary tension between particles also assume that r_c changes in a manner that maintains a constant mean radius of curvature in accordance with the Laplace Equation. This process is indicative of the pendular ring contracting inwardly as the surfaces are pulled apart, as shown in Fig. 4.11a. In this way, solid-vapor surface interface area is increased and liquid-vapor surface interface and solid-liquid surface interface areas are reduced. The capillary adhesion force derived from assuming this behavior, hereafter Type A

behavior, is given by (Israelachvili, 1992)

$$F_c = 4\pi R^* \gamma_{LV} \cos\theta \qquad (50)$$

Despite wide acceptance of Eq. (50), it often fails to match physical observations. A set of simple experiments was conducted using macroscopic objects with liquid pendular rings. The objective of the experiments was to observe if, in fact, the pendular ring could be seen to contract in the manner described by previous models. In some of the experiments, contradictions were observed in that the azimuthal radii of the pendular rings remained relatively constant as the surfaces were pulled apart. Elongation of the pendular ring occurred as the perimeter of the capillary pendular ring changed from a semi-circular shape to that of an inwardly extending semi-ellipse, as shown in Fig. 4.11b. This behavior is hereafter termed Type B behavior.

These observations can be explained by virtue of the fact that if the solid-vapor interface energy is sufficiently large so that the azimuthal radius of the pendular ring is maintained, then the fluid inside the pendular ring will be placed in mechanical tension beyond that of Laplace pressure. In order for static equilibrium to exist, the mechanical tensile pressure at the narrow central neck of the pendular ring must be greater than that at wider cross-sections. Hence, the radius of curvature in the middle of the pendular ring should be less than that at the radial extremities. An ellipse also can be used to exactly match the initial circular shape of the meniscus by setting the major axis equal to the semi-major axis.

A new model based on Type B behavior of a capillary pendular ring (i.e. Fig. 4.11b) was derived by maintaining a constant azimuthal radius and allowing the perimeter of the liquid to assume an semi-elliptical shape. In the derivation, the width and extent of the

parabola are respectively defined as L and B, as shown in Fig. 4.12. Equations defining an ellipse with these dimensions are

$$y = \frac{L}{2}\cos(\theta) \tag{51}$$

$$x = B\sin(\theta) \tag{52}$$

Fig. 4.11 Alternate Behavior of a Capillary Pendular Ring

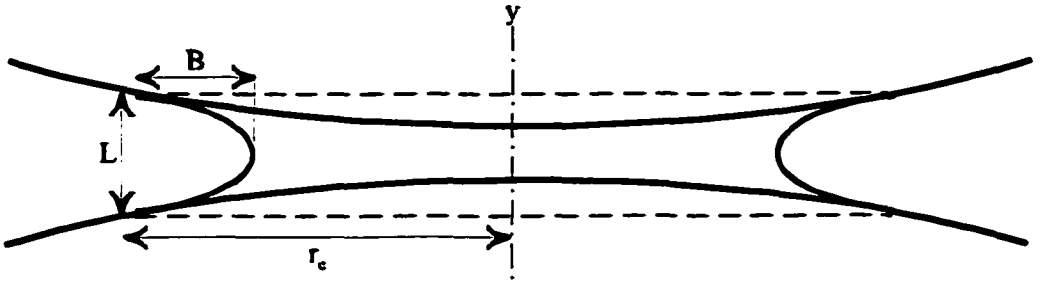

Fig. 4.12 Geometry of a Pendular Ring Exhibiting Type B Behavior

Using cylindrical coordinates, the distance, ρ, from the central axis of the pendular ring to any point along the parabola is simply equal to r_c+x. The volume of the pendular ring and the portion of the solid particles that extend into the ring can be found by integrating circular disks of differential thickness, dy, over the distance L. In terms of θ, this integral is

given by

$$V = \int_{\pi}^{2\pi} \pi\rho^2 \frac{dy}{d\theta}\, d\theta = \pi \left[L\, r_c^2 - \frac{\pi}{2} L\, B\, r_c + \frac{2}{3} L\, B^2 \right] \tag{53}$$

In order to impose the condition of constant volume, the partial derivative of V with respect to a change in L must be equal to zero. In taking this differential, the change in volume of the solid particles that extend into the pendular ring was assumed to be minimal.

$$\frac{\partial V}{\partial L} = \pi\left[r_c^2 - \frac{1}{2}\pi\, B\, r_c - \frac{1}{2}\pi\, L\, r_c \frac{\partial B}{\partial L} + \frac{2}{3}B^2 + \frac{4}{3}L\, B \frac{\partial B}{\partial L} \right] \tag{54}$$

By setting Eq. (54) equal to zero, the change in B with a change in L can be found.

$$\frac{\partial B}{\partial L} = \frac{6\, r_c^2 - 3\pi\, B\, r_c + 4\, B^2}{L\,(3\pi\, r_c - 8\, B)} \tag{55}$$

Provided that B changes in accordance with Eq. (55), the condition of constant pendular ring volume is satisfied.

The revolved surface area of the capillary parabola about the central axis of the pendular ring can be found using the mathematical expression for the area of a surface of revolution, given by

$$S = \int_{\pi}^{2\pi} 2\pi\, \rho\, dH \tag{56}$$

where the limits denote the inwardly extending portion of the ellipse and dH is the width of the differential band of revolution given by

$$dH = \sqrt{\frac{\partial x}{\partial \theta^2} + \frac{\partial y}{\partial \theta^2}} \tag{57}$$

The integral solution of Eq. (56) is a polynomial series of complete elliptic integrals of the first kind. Under initial equilibrium conditions, the capillary semi-ellipse has dimensions of width and height approximately equal to that of a semi-circle of minor capillary radius, r_s. When the limit of the solution to Eq. (56) is taken where L and B are approximately equal to $2r_s$ and r_s, respectively, the following result is obtained.

$$S = 2\pi^2 r_s r_c - 4\pi r_s^2 \tag{58}$$

The combined capillary surface energy of a system composed of two particles and a capillary pendular ring is equal to the sum of the solid-vapor interface, solid-liquid interface, and the liquid-vapor interface surface energies, as given by

$$U_c = \gamma_{SV} S_1 + \gamma_{SL} S_2 + 2\pi^2 \gamma_{LV} r_s r_c \tag{59}$$

where γ_{SV}, γ_{SL}, and γ_{LV} are the three different surface energies per unit area, S_1 is the surface area of the free solids, and S_2 is the total surface area of the particles that is in contact with the liquid pendular ring. The surface area given in Eq. (58) was simplified in Eq. (59) by eliminating the last term, which is negligible since r_s is much smaller than r_c. The capillary energy given by Eq. (59) is applicable to both Type A and Type B capillary behavior when the contact angle, θ, is small.

Adhesion force, F_c, arising from the capillary pendular ring is found by taking the partial derivative of the combined capillary energy with respect to a change in the distance between particles, L. For Type B capillary behavior, the azimuthal extent of the pendular ring remains constant. Consequently, the partial derivatives of S_1 and S_2 with respect to L are

equal to zero. Capillary adhesion force, therefore, depends only on the liquid-vapor surface area given by the last term in Eq. (59). Differentiating, with respect to L, the integral solution of Eq. (56) times the liquid-vapor surface energy results in a polynomial series of incomplete and complete elliptic integrals of the first and second kind. The limit of the solution was taken as L and B approach the values of $2r_s$ and r_s, respectively. The end result is given by

$$F_c = \pi \gamma_{LV} \frac{r_c (3\pi r_c^2 - 16 r_c r_s + 2\pi r_s^2)}{r_s (3\pi r_c - 8 r_s)} \tag{60}$$

which can be simplified to yield the following equation by virtue of the geometric property of the system that r_s is much smaller than r_c.

$$F_c = \pi \gamma_{LV} \frac{r_c^2}{r_s} \tag{61}$$

Viability of Type B capillary pendular ring behavior can be examined further by comparing the resulting capillary force, Eq. (61), with that known for Type A behavior, Eq. (50). The major difference between the two types of behaviors is in regard to assumptions about the shape that a capillary pendular ring will take upon application of external removal force. Both behaviors provide for the conservation of capillary fluid volume. Thermodynamically, the behavior that produces the lowest energy change should be predominant. Another way of stating this is that whichever behavior produces the least force of resistance is the more correct behavior. The capillary force associated with Type B behavior, Eq. (61), can be restated by incorporation of the geometric relationship, Eq. (48), which links r_c^2 to r_s.

$$F_c = 4\pi\ \gamma_{LV} R^*(1 - \frac{t-\delta}{2r_s}) \qquad (62)$$

A comparison of Eq. (62) with Eq. (50) results in the following inequality.

$$\textit{Type B force} < \textit{Type A force} \quad \textit{if} \quad \cos\theta > (1 - \frac{t-\delta}{2\,r_s}) \qquad (63)$$

For the materials of interest in this study (liquid water on mineral, metal, and glass surfaces), contact angle is very small and cos θ is approximately equal to one. Hence, the inequality can be restated as

$$\textit{Type B force} < \textit{Type A force} \quad \textit{if} \quad t > \delta \qquad (64)$$

According to contact mechanics Eqs. (27) and (30), the value of δ transitions from a positive quantity at equilibrium (α=1) to a negative quantity at the critical point of surface separation (α_c=1/3(a/r_c)^2). For most materials, except possibly very hard solids such as diamond, the distance of approach, δ, is typically greater than the thickness of adsorbed gas, t, when the particle is at rest. Hence, Type A force is predominant during the initial stage of particle removal. As the force applied to remove a particle increases, α decreases. At a particular instant, when the distance of approach, δ, is exactly equal to the thickness of adsorbate, capillary behavior should transition to Type B behavior. Hence, Type B force is predominant during the final stage of particle removal. This consequence is applied in the development of the adhesion force model in later sections.

4.4 Interparticle Forces

Interparticle forces that are incorporated in the theoretical derivation of a model for predicting dust adhesion include van der Waals and electrostatic. In circular-cylindrical coordinates, van der Waals energy between two surfaces of a differential unit area is given by (Israelachvili, 1992)

$$dU_{VDW} = -\frac{A_V}{12\ \pi\ d^2}\ \rho\ d\rho\ d\theta \qquad (65)$$

where ρ is the distance from the central axis of the contact, d is the total distance between the surfaces at point ρ, and A_V is the Hamaker Coefficient. A review of interparticle forces and a summary of determining the Hamaker Coefficient using the Lifshitz Theory, along with several example calculations for different mineral dusts interacting across water and across air or vacuum, is found in Chapter 7.0 and in Perko (1996).

The distance, d, between interacting curved surfaces outside the pendular ring as a function of ρ can be approximated using the parabaloid model given by

$$d = \frac{\rho^2}{2\ R^*} + t - \delta \qquad (66)$$

where δ is the distance that the two curved surfaces approach each other due to contact deformation and t is the thickness of an adsorbed film separating the particle contact.

As discussed in §4.1, van der Waals energy fields are significantly reduced by the presence of liquid at and near the contact of two curved surfaces. Furthermore, van der Waals energy fields within the deformed contact between two surfaces exist in the region of molecular repulsion called the Lennard-Jones potential, as depicted in Fig. 4.13. Lennard-

Jones repulsion is accounted for by considering compressive surface stresses within the derivation of the stored elastic energy term. A reasonable estimate of the total attractive van der Waals interaction energy between curved surfaces can be obtained by considering only those energy fields which interact outside the compression zone and outside the liquid pendular ring. By substitution of Eq. (66) into Eq. (65), the integral of the van der Waals energy outside the liquid pendular ring is given by

$$U_{VDW} = \int_{r_c}^{\infty} dU_{VDW} = -\frac{1}{3}\left(\frac{A_V R^{*2}}{r_c^2 - 2\delta R^* + 2tR^*}\right) \tag{67}$$

where the upper limit was set to infinity without significantly changing the result since van der Waals energy fields are of short range. Substitution of the previously derived geometric relationship between r_c and r_s, Eq. (48), into Eq. (67) allows U_{VDW} to be written in terms of r_s.

$$U_{VDW} = -\frac{1}{12}\left(\frac{A_V R^*}{r_s}\right) \tag{68}$$

In Fig. 4.10, it can be seen that the height of the capillary pendular ring, given by 2 r_s, and the distance over which van der Waals forces act can not be less than the adsorbate thickness, t, minus the distance of approach, δ. Hence, another important geometric constraint is

$$r_s \geq \frac{t-\delta}{2} \tag{69}$$

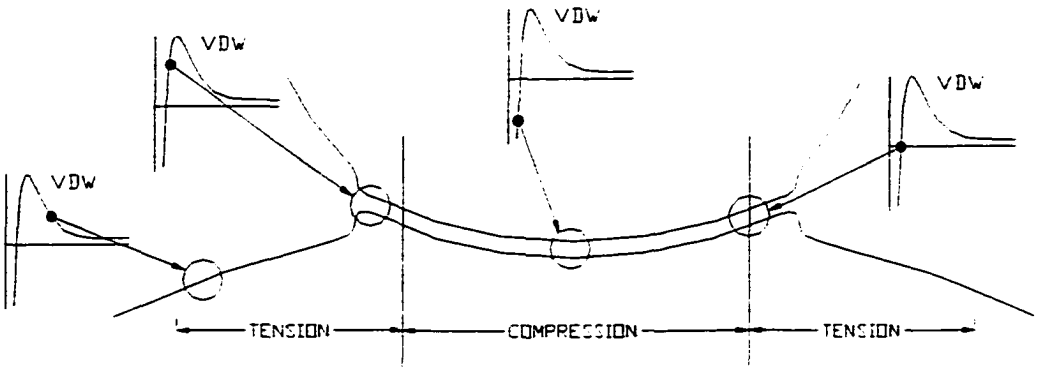

Fig. 4.13 State of Intermolecular Energy Fields within a Particle Contact

With regard to electrostatic forces, they too are significantly reduced by the presence of a liquid pendular ring. Thus, it is assumed that higher order polarization and dipole fields are negligible. Outside the pendular ring, electrostatic energy fields act at longer range and can be approximated using simpler equations. The Coulomb interaction between two charged particles is given by

$$U_{ELEC} = \frac{Q_1 Q_2}{4\pi\epsilon_o (R_1 + R_2 + t - \delta)} \qquad (70)$$

where Q_1 and Q_2 are the net electrostatic charge of each of the interacting particles of respective radii R_1 and R_2. The distance between the geometric centers of the two surfaces was set equal to the sum of their radii of curvature plus the thickness of adsorbate, t, minus the distance of approach, δ. Since the pendular ring is assumed small compared to radius of the particles, electrostatic forces primarily interact across air or vacuum and $\epsilon = 1$. When the

majority of electrostatic charge is present as surface charge density, Q_1 and Q_2 may be approximated by $4\pi R_1^2 s_1$ and $4\pi R_1^2 s_1$, respectively.

The electrostatic potential between a charged particle and a dielectric surface is the same as that between a charged particle and a grounded conducting surface (Jackson, 1975). The interaction energy, which was determined through the method of imaging and accounts for the dielectric properties of the surface, is given by (adapted from Griffiths, 1999)

$$U_{IMG} = -\frac{Q^2}{16\pi\epsilon_o (R_1 + R_2 + t - \delta)} \frac{\epsilon - 1}{\epsilon + 1} \tag{71}$$

where ϵ is the relative dielectric permittivity of the dielectric surface. When the surface is a conductor, ϵ approaches infinity and the right side of Eq. (71), which contains the ϵ term, approaches 1 in the limit.

4.5 Dust Adhesion Model

From Eq. (27), the Hertzian contact radius at equilibrium when α=1 is given by

$$a_o = \frac{1}{2}\left(\frac{6 F_o R^*}{E^*}\right)^{1/3} \tag{72}$$

The equilibrium tensile force term, F_o, consists of van der Waals, electrostatic, and capillary forces. Van der Waals energy, Eq. (68), is independent of a_o because r_s, which was derived in §4.1, is only a function of ambient environmental conditions. The dependance of electrostatic energies, Eqs. (70) and (71), on a_o is negligible since δ is very small compared to R_1 and R_2 in the parabaloid approximation. In equilibrium and during initial particle

removal modes, the liquid pendular ring follows Type A behavior, which is characterized by constant capillary force, and hence the capillary energy is also independent of a_o. Thus, the net tensile force F_o in Eq. (72) can be determine by direct summation of the component forces.

The van der Waals and electrostatic force components can be derived by differentiating energy with respect to the distance of separation ($-\delta$). The partial derivative of minor capillary radius, r_s, with respect to $-\delta$ in the van der Waals energy term can be determined from Eq. (48) and is equal to

$$\frac{\partial r_s}{\partial(-\delta)} = \frac{1}{2} \tag{73}$$

Differentiation of capillary energy with respect to separation distance is the capillary force given in Eq. (50). The total tensile force at equilibrium is therefore given by

$$F_o = 4\pi\ \gamma_{LV} R^*\ Cos\ \theta\ + \frac{1}{24}\left(\frac{A_V R^*}{r_{so}^2}\right) - \frac{Q_1 Q_2}{4\pi\epsilon_o(R_1+R_2)^2} + \frac{Q^2}{16\pi\epsilon_o(R_1+R_2)^2}\frac{\epsilon-1}{\epsilon+1} \tag{74}$$

where r_{so} is the minor capillary radius at equilibrium. In Eq. (74), the distance of approach under equilibrium conditions and the thickness of adsorbate was removed from the electrostatic terms after integration since they are much smaller than the particle and surface radii of curvature. Substitution of Eq. (74) into Eq. (72) enables determination of the initial contact radius.

According to Derjaguin, the smallest spacing between surfaces is the distance z_o where van der Waals attraction is balanced by Lennard-Jones molecular repulsion (Note: Derjaguin actually used the symbol ϵ, however that symbol is used for relative permittivity herein). The

van der Waals term in Eq. (74), when $2 r_s = z_o$, can be rewritten as

$$F_{o_{VDW}} = \frac{1}{6}\left(\frac{A_V R^*}{z_o^2}\right) \tag{75}$$

Solid-vapor surface energy, γ_{SV}, is approximately 2 times the van der Waals energy between surfaces, Eq. (68), separated by distance z_o. According to this definition, substitution of solid surface energy into Eq. (75) results in an adhesion force equal to $4\pi R^* \gamma_{SV}$. For electrostatically neutral surfaces and particles, the total tensile force is obtained by substitution of the latter term into Eq. (74).

$$F_o \approx 4\pi\ \gamma_{LV} R^* \cos\theta + 4\pi\ \gamma_{SV} R^* \qquad \textit{Electrostatic Charge} = 0 \tag{76}$$

For many surfaces with liquid water pendular rings, the liquid-vapor interaction energy term in the Young equation, presented in Chapter 3, is much greater than the solid-liquid interaction term. Consequently, $\gamma_{LV} \cos\theta$ is approximately equal to γ_{SV} and the resultant initial contact radius, found by substitution of Eq. (76) into Eq. (72), is given by

$$a_o \approx \left(\frac{7\pi\ R^{*2}\ \gamma_{SV}}{E^*}\right)^{1/3} \qquad \textit{Electrostatic Charge} = 0 \tag{77}$$

This is approximately 35% greater than the contact area predicted by the JKR model (Johnson, 1985). The dependence of initial contact radius on $R^{*2/3}$ is consistent with past laboratory measurements and is generally accepted for elastic contact (Maugus and Pullock, 1995). Despite this general acceptance, laboratory measurements have shown that the dependance of contact radius on R* can vary (Rimai and Busnaina, 1995). Introduction of electrostatic energy terms, which depend on R^{*-2}, into the derivation of the initial contact radius is a possible means of explaining variations in the dependence of contact radius on R*

that have been measured previously.

The initial equilibrium tensile forces given in Eqs. (74) and (76) are not equal to the removal force, nor are they equal to the force that must be applied to initiate particle removal. Rather, these forces represent the total tensile surface stress, which is exactly balanced by compressive surface stresses when the particle is at rest. Steady state equilibrium minor radius, r_{so}, of the liquid pendular ring can be determined using methods described in §4.1. Equilibrium distance of approach, δ_o, and initial stored elastic energy, U_{co}, can be determined simply by substitution of Eqs. (74) and (72) for F and a in Eqs. (30) and (31) with α=1. Once the distance of approach is known, steady state equilibrium azimuthal radius, r_{co}, of the liquid pendular ring can be determined from Eq. (48).

As determined in §4.3, the process of separation of two curved surfaces occurs initially with the capillary pendular ring in Type A capillary behavior mode. As the surfaces are pulled apart, a point will be reached where the distance of approach, δ, between the surfaces is momentarily equal in magnitude to the adsorbed gas thickness, t. According to the condition prescribed by Eq. (64), additional movement of the surfaces occurs with the capillary pendular ring in Type B behavior mode, and subsequently azimuthal radius, r_c, remains constant. Since the geometric constraint imposed by Eq. (48) continues to govern capillary pendular ring shape during Type A behavior, the value of r_c at the transition point can be determined directly from Eq. (48) with δ set equal to t, as given by

$$r_{cf} = 2\sqrt{R^* r_{so}} \tag{78}$$

The magnitude of r_{so} can be calculated using steady-state equilibrium methods provided in

§4.1. The value of r_{cf} remains constant from the transition point to the point of final particle removal.

The total energy, U_T, of a system of two elastically deformed surfaces with an interplay of capillary, van der Waals, and electrostatic interactions is given by

$$U_T = U_e + U_c + U_{VDW} + U_{ELEC} + U_{IMG} \tag{79}$$

At the instant of particle removal ($\alpha=1/3(a/r_c)^2$), the stored elastic energy is given by (reprint of Eq. (35))

$$U_{ef} = -\frac{17\,R^*\,E^*}{4\,r_{cf}}\,\delta_f^3 \tag{80}$$

Substitution of Eq. (80), stored elastic energy, and Eqs. (59), (68), (70) and (71), capillary, van der Waals, and electrostatic energies, into Eq. (79) results in the total energy of the system given by

$$U_T = -\frac{17\,R^*\,E^*}{4\,r_{cf}}\,\delta_f^3 + \gamma_{SV}\,S_1 + \gamma_{SL}\,S_2 + 2\pi^2\,\gamma_{LV}\,r_{cf}\,r_{sf} - \frac{1}{12}\left(\frac{A_V\,R^*}{r_{sf}}\right) + \frac{Q_1\,Q_2}{4\pi\epsilon_o\,(R_1+R_2+t-\delta_f)} - \frac{Q^2}{16\pi\epsilon_o\,(R_1+R_2+t-\delta_f)}\,\frac{\epsilon-1}{\epsilon+1} \tag{81}$$

The change in total energy with respect to a change in δ_f is indicative of the change in force applied to the system. Therefore, the peak removal force will occur where this change experiences a maximum. In order to find this point, the second derivative of Eq. (81) must be taken with respect to $-\delta_f$. The independent variables in Eq. (81) are the final minor capillary radius and final distance of approach r_{sf} and δ_f. The partial derivative of r_{sf} with respect to $-\delta_f$ from Eq. (73) was used to evaluate the van der Waals term. Final azimuthal

radius, r_{cf}, is obtained from Eq. (78), and since it is a constant, surface areas S_1 and S_2 are also constants. Differentiation of the remaining capillary term can not be performed directly. Instead, the expression given by Eq. (61), which was found by differentiating with respect to L, is appropriate since $\partial L/\partial(-\delta) = 1$. The end result of these manipulations provides the first partial derivative of U_T with respect to $-\delta$ given by

$$\frac{\partial U_T}{\partial(-\delta_f)} = \frac{51\ R^*\ E^*}{4\ r_{cf}}\ \delta_f^2 + \pi\ \gamma_{LV}\ \frac{r_{cf}^2}{r_{sf}} + \frac{1}{24}\left(\frac{A_V\ R^*}{r_{sf}^2}\right) - \frac{Q_1\ Q_2}{4\pi\epsilon_o\ (R_1+R_2+t-\delta_f)^2} + \frac{Q^2}{16\pi\epsilon_o\ (R_1+R_2+t-\delta_f)^2}\ \frac{\epsilon-1}{\epsilon+1} \tag{82}$$

In taking the second partial derivative, it is recognized that the change in electrostatic components will be small since R_1 and R_2 are much larger than δ_f. The partial derivative of the capillary term is taken directly. Again, Eq. (73) is implemented to evaluate the partial derivative of r_{sf} in the van der Waals and capillary terms. The end result of differentiation is given by

$$\frac{\partial U_T^2}{\partial^2(-\delta_f)} = -\frac{51\ R^*\ E^*}{2\ r_{cf}}\ \delta_f - \pi\ \gamma_{LV}\ \frac{r_{cf}^2}{r_{sf}^2} - \frac{1}{24}\left(\frac{A_V\ R^*}{r_{sf}^3}\right) \tag{83}$$

By applying Eq. (48), Eq. (83) can be expressed in terms of either r_{sf} or δ_f only. The roots of r_{sf} and δ_f could not be obtained exactly. However, analysis of each term in the expression indicates that the two effects act fairly independently. The capillary term is most significant in humid environments when r_{cf} is large. The van der Waals term is most significant in dry environments when r_{cf} is small. Since the terms in Eq. (83) act over fairly separate and distinct ranges, each was evaluated independently and summed to find the

desired roots of r_{sf} and δ_f that occur at the energy transition point.

To evaluate the root of the capillary term, Eqs. (48) and (78) were examined. From these equations it can be seen that if r_{cf} is large, then r_{sf} is approximately equal to $(2r_{so} + t)/2$. Input of this equation into Eq. (83) and omission of the van der Waals term allow for the partial root to be found.

$$\delta_{f1} = -\frac{8\pi\ \gamma_{LV}\ r_{cf}^3}{51\ R^*\ E^*\ (2\ r_{so} + t)^2} \tag{84}$$

To evaluate the root of the van der Waals term, it is recognized in Eq. (48) that if r_{cf} is small, then r_{sf} is approximately equal to $-\delta_f/2$. By substitution of this equation in Eq. (83) and omission of the capillary term, the partial root of δ_f is found.

$$\delta_{f2} = -\left(\frac{4\ A_V\ r_{cf}}{153\ E^*}\right)^{1/4} \tag{85}$$

Combining the two partial roots, Eq. (84) and Eq. (85) results in an approximate means of determining δ_f given by

$$\delta_f = -\frac{8\pi\ \gamma_{LV}\ r_{cf}^3}{51\ R^*\ E^*\ (2r_{so}+t)^2} - \left(\frac{4\ A_V\ r_{cf}}{153\ E^*}\right)^{1/4} \tag{86}$$

The final minor capillary radius, r_{sf}, at the instant of particle removal is obtained from Eq. (48).

$$r_{sf} = \frac{1}{2}\ (\ 2\ r_{so} + t - \delta_f\ ) \tag{87}$$

Final contact area was found by combining Eqs. (22), (27) and (30) and is given by

$$a_f = r_c - \sqrt{r_c^2 - \delta R^*} \tag{88}$$

At the instant of particle removal, the critical force ratio is reached and the surfaces jump apart. Under this assumption, the remaining stored elastic energy is lost to heat, sound, triboelectrostatic charge, or velocity of the particle. Stored elastic energy does not contribute to the final removal force. The removal force is determined by taking the partial derivative of the total energy of the system with respect to surface spacing t. The elastic term is assumed constant. To evaluate the van der Waals term, determination of the partial derivative of r_{sf} with respect to t is necessary. From Eq. (48), this derivative is given by

$$\frac{\partial r_{sf}}{\partial t} = \frac{1}{2} \tag{89}$$

The derivative of the capillary term with respect to t is correctly represented by Eq. (61) since $\partial L/\partial t = 1$. Thus, the removal force is equal to

$$F_a = \pi \gamma_{LV} \frac{r_{cf}^2}{r_{sf}} + \frac{1}{24}\left(\frac{A_V R^*}{r_{sf}^2}\right) - \frac{Q_1 Q_2}{4\pi\epsilon_o (R_1+R_2)^2} + \frac{Q^2}{16\pi\epsilon_o (R_1+R_2)^2} \frac{\epsilon-1}{\epsilon+1} \tag{90}$$

In summary, the important simplifying assumptions used in deriving the adhesion model were that the particle and surface are linearly elastic, liquid contact angles are small, and that the azimuthal radius of the capillary pendular ring and the radius of elastic contact are much less than the radius of curvature of the surfaces. As such, the model is not appropriate for surfaces and fluids with large contact angles, for very soft or non-linear elastic particles and surfaces, or for very wet environments.

The limit of Eq. (90) at high humidity was examined in order to evaluate its validity. For electrostatically neutral surfaces at high humidity, the van der Waals and electrostatic terms are negligible. Also at high humidity, r_{so} is much larger than a_f and t, and the ratio of r_{cf}^2 to r_{sf} is approximately equal to 4R*. Thus, the value of adhesion predicted by Eq. (90) is approximately given by $4\pi R^*\gamma_{LV}$. This value is exactly the same as that given by conventional capillary theory, $4\pi R^*\gamma_{LV}$, for fluids with a small contact angle.

At intermediate levels of humidity, the model predicts a smaller capillary force than that of conventional theory. Experimental data from Fisher and Israelachvili (1981), shown in Fig. 4.14, provide a verification of this prediction. The dashed line in the figure represents the force of capillary adhesion based on conventional theory with Type A pendular ring behavior only. The solid line in the figure represents a prediction based on the new model which utilizes Type B pendular ring behavior. For the model input, the Hamaker coefficient for mica computed by Perko (1996) was used, and the upper value ($5x10^{12}$ dyn/cm^2) of the Young Modulus for the composite mica, glue, and glass cylinders given by Horn, Israelachvili, and Pribac (1987) was used. As can be seen in the figure, the model matches the experimental data remarkably well. The data of Fisher and Israelachvili has been criticized by Christensen (1985), who showed that the use of a double spring atomic force microscope yields slightly different results than those obtained using a leaf spring atomic force microscope. Christensen's data also can be matched by application of the model with a slightly higher Modulus of Elasticity for the crossed mica cylinders.

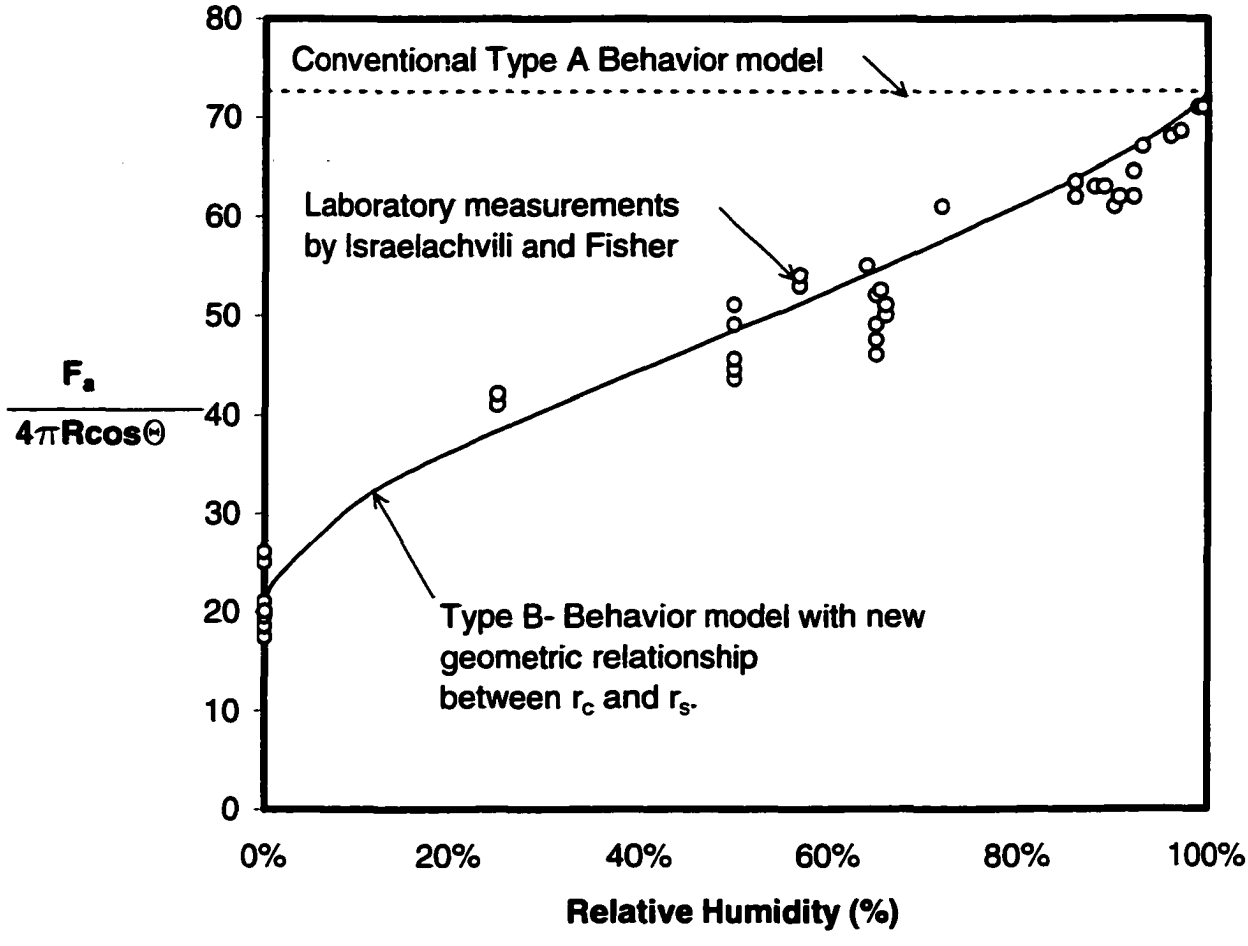

Fig. 4.14 Model Predictions for Crossed Mica Cylinders

(adapted from Fisher and Israelachvili, 1981)

For electrostatically neutral surfaces at the limit of negligible humidity, the capillary and electrostatic terms in the model are approximately equal to zero. According to Derjaguin, the smallest spacing between surfaces is the distance z_o where van der Waals attraction is balanced by Lennard-Jones molecular repulsion (Note: Derjaguin actually used the symbol ϵ, however that symbol is used for relative permittivity herein). The adhesion force predicted

by Eq. (90) under these conditions and when $2 r_s = z_o$ is approximately equal to

$$F_{a_{2r_s=z_o}} = \frac{1}{6}\left(\frac{A_V R^*}{z_o^2}\right) \tag{91}$$

Solid-vapor surface energy, γ_{SV}, can be estimated by taking 2 times the van der Waals energy between surfaces, Eq. (64), separated by distance z_o. According to this definition, substitution of solid surface energy into Eq. (91) results in a predicted adhesion force equal to $4\pi R^*\gamma_{SV}$. This value is exactly the same as that predicted by the DMT model.

CHAPTER 5.0 LABORATORY INVESTIGATION

A laboratory investigation was conducted to verify the theoretical model over a range of planetary environments from Earth-like to comet-like conditions. Specifically, variations in dust adhesion with changes in environmental conditions of humidity, pressure, and temperature were measured. Effects of dust particle roughness, size, and mineralogy and the composition of surface materials on dust adhesion were also investigated.

The experiments consisted of depositing dust onto various spacecraft materials under different environmental conditions and attempting to mechanically shake the dust off to obtain a measure of adhesion. A specimen of each different material was affixed to a vibrating cantilever beam, which was used to induce dust separation. An identical specimen of each material was mounted to an electrometer, which was used to witness accumulated dust mass and charge. Dust was sifted onto the specimens in an environmentally monitored and controlled chamber. Dust adhesion force was determined from the amplitude and frequency of beam vibrations and the mass of dust particles.

5.1 Dust Specimens

In order to enable comparison with the theoretical model, which involves spherical dust particles resting on a surface, 53 to 75 μm spherically shaped glass beads

were selected as the control or benchmark dust material to be used in the majority of the experiments. Glass spheres in this size range exert an adhesive force that is capable of being easily measured by the experimental apparatus. The dependence of dust adhesion on particle size was investigated using glass spheres that were both smaller and larger in diameter as compared to the benchmark dust. The dependence of dust adhesion on particle mineralogy and roughness was investigated using crushed olivine particles of the same gradation as the benchmark dust. Olivine was selected as a mineral of particular interest due to its predominance in comet surface charge density material.

The glass beads were obtained from Jaygo, Inc. of Union, NJ. Commercially termed "Dragonite", these glass beads are predominantly used as grinding media in various manufacturing processes. The specific type of glass comprising the spheres is fused quartz according to the manufacturer. Using a set of wet sieves, the beads were separated into four groups of particles with diameters of 38 to 45 μm, 45 to 53 μm, 53 to 75 μm, and 75 to 100 μm. An optical micrograph of a sample of particles from the benchmark range of 53 to 75 μm at 100X magnification is shown in Fig. 5.1. It can be seen in the figure that most of the glass beads are spherically shaped. The specific gravity of the beads was measured to be 2.30 by the water displacement method. The index of refraction of the beads was measured using optical microscopy and oil emersion, and a value of 1.518 +- 0.004 was obtained. The relative dielectric constant for quartz glass is 3.75 (CRC, 1997). According to the manufacturer, the Mohs hardness of the glass beads is 6.0.

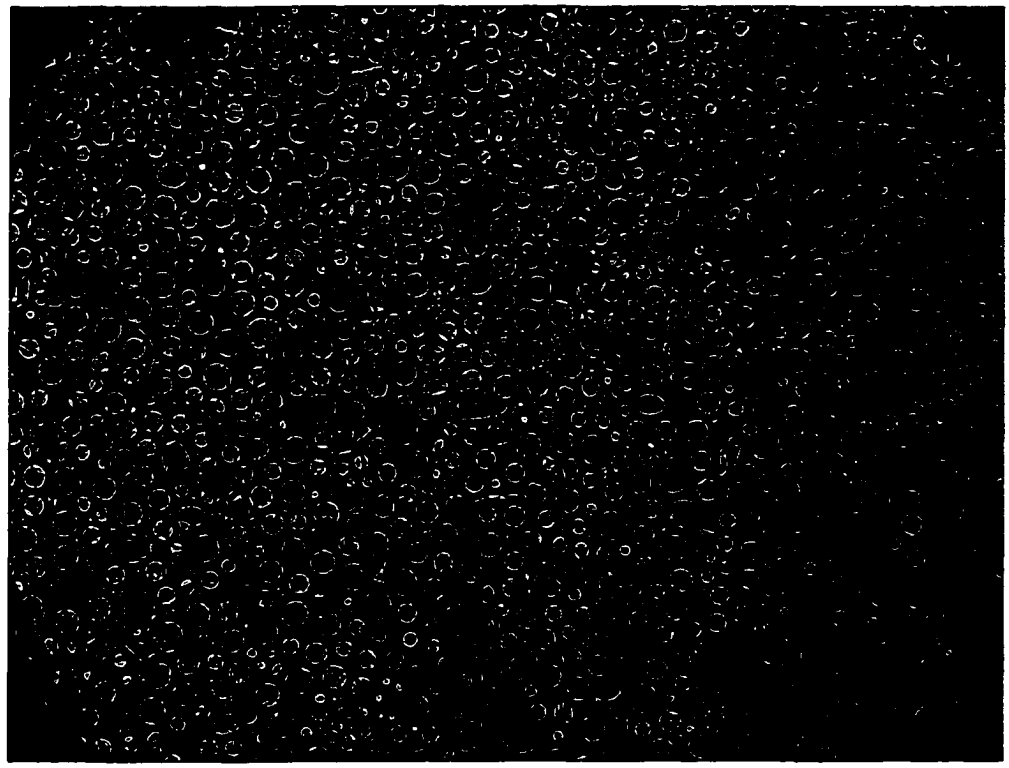

Fig. 5.1 Optical Micrograph of Glass Spheres

The olivine dust was obtained from Unimin, Inc. of Hamilton, WA. The olivine is type AFS-GFN 278 and is used commercially as a low expansion foundry sand for investment casting. The chemical breakdown of the olivine consists of 48% magnesium oxide, 43% silicon dioxide, 8% iron oxide, and other minor oxides. The sample used in the dust adhesion experiments was passed through a set of wet sieves to obtain a group of particles with diameters from 53 to 75 μm. An optical micrograph of a sample of olivine at 100X magnification is shown in Fig. 5.2. It can be seen in the figure that the olivine is angular and blocky. The specific gravity and index of refraction of the olivine were measured as described above. A specific gravity value of 3.52 was obtained. The index of refraction was measured to be between 1.65 and 1.68. These values indicate that the

olivine is 92%-95% Mg as opposed to Fe. In addition to the three principal crystal directions, a small amount of variability in the index of refraction was observed in the sample. The relative dielectric constant for olivine is unknown but is expected to be in the typical range of minerals from 4 to 12. The Mohs hardness of olivine is 6.8 (CRC, 1997).

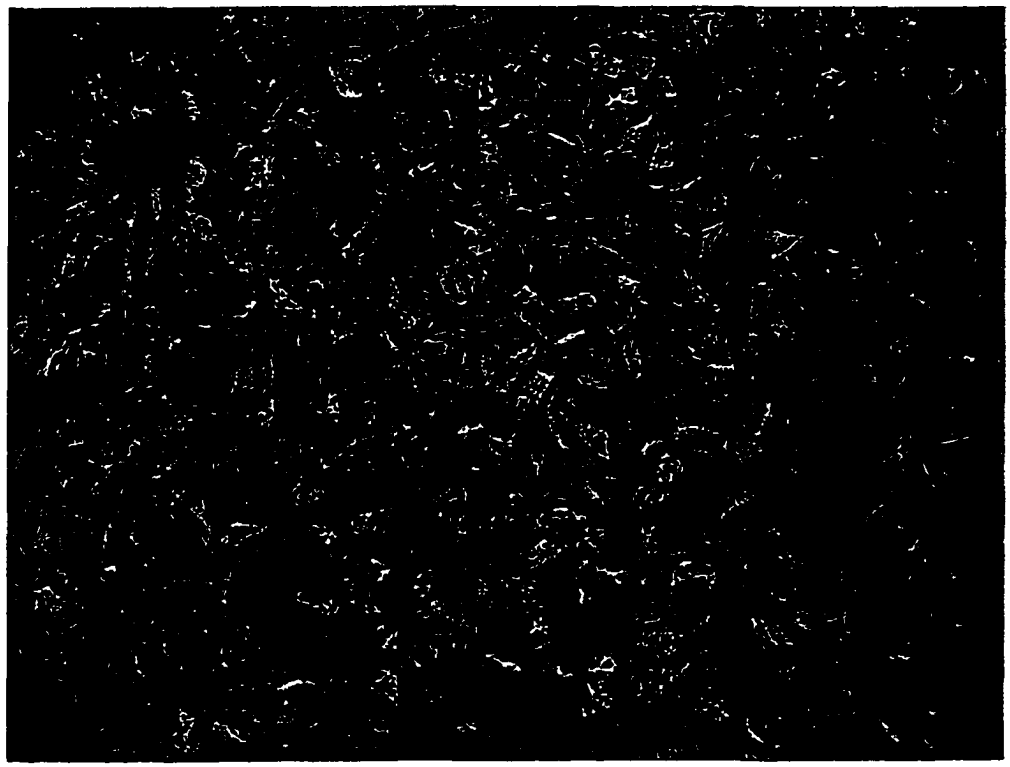

Fig. 5.2 Optical Micrograph of Olivine Dust

Dust samples were handled using non-latex surgical gloves to avoid contamination. Prior to use in the experiments, all dust samples were wet sieved using tap water. The samples were rinsed with distilled water and oven dried at 105 degrees C for 24 to 48 hours. Following oven drying, all samples were exposed to laboratory air for a period of several days.

In order to determine if organic contaminants were present on the surfaces of the dust, approximately 100g samples of the glass and the olivine were saturated with Freon and then vacuum dried through a 10 μm filter pad. The filter pad was examined under ultraviolet light and no fluorescence was observed.

5.2 Material Specimens

The material surfaces used in the dust experiments consisted of painted aluminum, bare aluminum, stainless steel, and glass. The paint was a type of NASA approved spacecraft black provided by spacecraft assembly personnel at JPL. The aluminum and stainless steel were obtained from K&S Engineering Company of Chicago, IL. The glass was obtained from the optics laboratory at JPL and is believed to be a type of Crown glass. All of material specimens were approximately 2.5 x 5 cm (1 x 2 in) in size and ranged in thickness between 1.2 and 3.5 mm. The hardness, Poisson Ratio, Young Modulus, density, index of refraction, and dielectric constant of each material are given in Table 5.1.

Hardness of the specimens was measured using an ATS Digital Rockwell Type Hardness Tester, Model ADT8 and the procedures for Rockwell Hardness Scale 15-T which incorporates a 1/16" diameter steel ball, a 10 Kg minimum load, and a 15 Kg maximum load. Similar results were obtained using the superficial test which incorporates a minimum load of 3 Kg and a maximum load of 15 Kg. The hardness values shown in the table represent the average and standard deviation of 10 measured values. Index of refraction, dielectric constant, and density were obtained from the CRC Handbook (1997). Young Modulus and Poisson Ratio are from Machinery's

Handbook (2001). In order to enable direct use in the generalized Lifshitz theory for computation of Hamaker Coefficients, index of refraction is given at the mean value within the visible range of wavelengths and the dielectric constant is given as the static, zero frequency, value. The dielectric constant and index of refraction for polyvinyl chloride were assumed to approximate the properties of the black spacecraft paint. The shear modulus of acrylic was used for the Young Modulus of the paint. The index of refraction for iron-oxide was assumed to approximate that of stainless steel due to exposure of the surface to humid air.

Table 5.1 Material Specimen Properties

Material	Hardness	Poisson Ratio	Young Modulus (GPa)	Density (g/cm3)	Index of Refraction	Dielectric Constant
Painted Aluminum	70 ± 12	0.33	3	2.7	≈1.5	≈3.2
Aluminum	56 ± 2	0.33	70	2.7	1.3	∞
Stainless Steel	86 ± 1	0.31	190	7.9	≈2.0	∞
Glass	99 ± 1	0.24	46	2.4	1.5	5

Prior to each experiment, material specimens were cleaned using the following procedure.

1.) high pressure rinse with tap water

2.) ultrasonic clean for 5 minutes in a mild detergent

3.) rinse with tap water

4.) blot dry with a lint-free laboratory tissue

5.) submerge in a mild acetone solution (10%) for 30 seconds

6.) agitate in two separate distilled water rinses

7.) oven dry at 105 deg C for a minimum of 12 hrs

The specimens were weighed on an electronic scale (A250 Denver Instrument Company) with 0.0001 g accuracy and individually placed in covered petri dishes where they remained until use. The material specimens were handled by their edges or with non-latex surgical procedures gloves at all times to avoid contamination.

At the start of each test the specimens were wiped with a chemical degreasing solution from Micromeasuments, Inc. (CSM-1, a tricholoro-trifluoro-ethane spray) using separate lint-free, delicate task wipes (Kimwipes EX-L from Kimberly Clark) for each specimen. The material specimens were attached to the experimental apparatus using nylon or Teflon screws and were underlain with a 0.50 mm thick Teflon sheet to electrically isolate them from the apparatus. Two sets of identical material specimens were used in order to expedite testing procedures. This enabled one set of specimens to be involved in the experiments, while the other was being weighed and cleaned for the next experiment. An alphanumeric designation was etched in the corner of each specimen for identification and to ensure that the specimens were mounted to the apparatus in the same way every time.

5.3 Apparatus

The experimental apparatus, shown in Fig. 5.3 and in more detail in App. I, consisted of bottom plate, four columns, structural cross members, a sheet-metal sieve/shaker box, a test platform, and aluminum dust shields over the electronics. Along one side of the test platform was mounted a rectangular fixture from which eight channel beams were cantilevered. The beams were attached by pounding the end into a slot with a rubber mallet and then compressing them with a screw-fastened strap across the top. Along the other side of the test platform was an electromagnet with four openings. The openings were positions at the fee ends of four of the cantilever beams. "Voice coils", formed by 300 wraps of 30 ga Teflon coated magnet wire around a grooved Teflon block, were affixed to the cantilever beam ends at these openings. The impedance of the voice coils varied from 8.5 to 9.5 Ω. The electromagnet was milled from mu-metal bar stock wrapped with 500 winds of 27 ga Teflon coated copper wire. The rest of the apparatus, except the electronics, was constructed using only aluminum plate, stainless steel screws, and Teflon bushings to minimize outgassing in vacuum.

The experimental apparatus was constructed so that the test platform was positioned at a location that allowed for optimal observation through the glass viewports at the top of the vacuum chamber. The test platform was bolted at each end to the frame in a way that enabled single axis rotation. Thereby, the test platform could be tilted and fixed at an angle from approximately -75 degrees to +75 degrees from horizontal. The sieve/shaker box was oriented above the test platform on two hinged arms. The arms and box moved uniformly in a radial direction about the approximate center of the apparatus upon the application of force to a bar that connected the two arms. Force was transmitted

Fig. 5.3 Experimental Apparatus

to the connecting bar via a linear mechanical feedthrough in the vacuum chamber. In this manner, the sieve/shaker box could be rotated from a position offset the test platform to a position directly over it. This rotation was necessary to prohibit dust from falling from the box onto the material specimens during the experiment and to allow for possible irradiation of the dust-coated specimens using the solar simulator. The sieve/shaker box could be fitted with either a No. 50, 70, 80, 100, 140, 200, or 280 U.S. standard size wire cloth sieve. On either side of the sieve were located two electromagnetic actuators that "clicked" when activated and subsequently caused a small amount of dust to fall through the sieve onto the test platform below. Early in the experiment, it was determined that electromagnetic noise from the "clickers" was affecting electrometer measurements.

Consequently, the box was mechanically tapped or agitated, and the "clickers" were abandoned.

The four cantilever beams without voice coils were instrumented with independent nearly identical electrometers. Dr. Martin Buehler of JPL assisted with the design of these devices. They are similar in design to the electrometers that were to be used to study the triboelectric behavior of Martian dust on-board the Mars Polar Lander (Buehler, 2000). A wiring diagram for the electrometers is contained in App. II. Essentially, the electrometers function by providing a measurement of voltage across a capacitor of known capacitance that was connected in series with a capacitor formed by one of the material specimens and Teflon sheets overlaying a copper clad circuit board. The voltage measurement was amplified 101X using an operational amplifier integrated circuit that was located nearby. The amplified voltage was read outside the vacuum chamber using either a RadioShack True RMS Multimeter or a Fluke 87 III True RMS Multimeter. Electrostatic charge of the material specimen with dust was determined simply by Q=C V where Q is charge, C is the known capacitance, and V is the voltage measurement. Two of the electrometers were constructed using 0.4 nF capacitors and two were constructed using 2.0 nF capacitors. The electrometers are capable of detecting and measuring a total electrostatic charnge as little as 0.1 pC on each of the material specimens. The stability of the electrometers was determined by monitoring the amplified voltage readings over time. Current leakage of the electrometers was near the tolerance reported by Buehler (2000).

The four cantilever beams with voice coils were instrumented with strain gages in order to measure vibration amplitude. Strain gages were affixed to the top, sides, and

inner web of the channels at a location very near the beam fixture block. The strain gages were connected to form a temperature compensating, full Wheatstone bridge. The voltage reading across the bridge was amplified 100X using an instrument amplifier integrated circuit located near the fixed end of each beam. A full wiring diagram for the stain gages and amplifier is contained in App. II. Amplification of the bridge voltage increased the signal to noise ratio and enabled discernable measurements of beam displacements on the order to 10 μm despite the electrically noisy environment of the vacuum chamber.

Amplified Wheatstone bridge voltage measurements were viewed and recorded using a high speed National Instruments Data Acquisition Card, a Gateway 2000 Pentium II Computer, and LabView software for Windows. A copy of the virtual instrument program written in LabView is contained in App. III. The program was written so that 40 voltage readings were taken over a time period corresponding to 4 times the period of the excitation or driving frequency. Provided the beams were vibrating at the driven frequency, this programming resulted in 4 full periods being displayed in "oscilloscope" type format on the computer screen. Amplitude of the beam vibrations was read from the y-axis of the display. Each of the four Wheatstone bridges was calibrated statically using a digital displacement dial gage at a set distance from the beam fixture. Calibration plots for each of the beams are provided in App. IV. The displacement or amplitude of vibration increased from near zero at the fixture to a maximum value at the end of the cantilever. Displacement or amplitude at a given distance from the beam fixture was computed using elastic equations for single mode beam vibration as outlined in App. IV.

Vibrations were excited individually in each of the beams by passing a sinusoidal alternating current through their respective voice coils. The alternating current was generated by the data acquisition card using LabView. Driving frequency was set equal to the resonant frequency of each of the beams. Driving current was increased through the use of a 30 W audio amplifier. The voice coils were positioned halfway in the magnetic field created by the large electromagnet bar attached to the test platform. As current is passed through the voice coils, it caused them to be forced into or out of the magnetic field depending on direction of the current at that instant. This design is similar to the technology used in audio speakers. The resonant frequency was determined for each beam using a scanning virtual instrument program written in LabView that incrementally increased the driving frequency by 0.5 Hz every 500 ms.

The 30 W audio amplifier, as well as the power supplies for the strain gages, instrumentation amplifiers, electrometers, electromagnet, sieve shakers, and audio amplifier, were all hand-built and housed in an electronics project enclosure. Wiring diagrams for the complete project enclosure are contained in App. II.

5.4 Environmental Chambers

Vacuum and cryogenic experiments were conducted at the Extraterrestrial Materials Simulation Laboratory at the NASA Jet Propulsion Laboratory in Pasadena, CA. A Kurt J. Kesker Company 1.0 m diameter ultrahigh vacuum chamber, equipped with temperature controlled internal shrouds, was used for the experiments. A photograph of the vacuum chamber and control unit is shown in Fig. 5.4. The chamber was fitted with two thermocouple pressure transducers and a cold cathode pressure ion

gauge. Two thermocouples and Omega controllers were used to monitor and control the temperatures of the internal shrouds. A third thermocouple was affixed to the bottom of the experimental test platform and was used to directly monitor the temperature of the apparatus. A differentially pumped residual gas analyzer was also fitted to the chamber. During the vibration and dust deposition phases of the experiment, this residual gas analyzer was isolated from the chamber to reduce the risk of dust contamination. The chamber was equipped with a scroll pump and a turbo pump. The entire system was completely oil free so as to avoid contamination. Cryogenic temperatures were obtained by controlled circulation of liquid nitrogen through the internal shrouds. Bakeout of the chamber was accomplished by circulation of heated gaseous nitrogen through the internal shrouds.

Fig. 5.4 Vacuum Chamber

Controlled humidity and cold temperature experiments were conducted in a walk-in humidity chamber and a walk-in freezer at the Shepherd Miller and John D. Nelson Graduate Geotechnical Laboratory at Colorado State University. Each chamber has a circular chart that records temperature and humidity during the experiment. Temperature and humidity were controlled to within 2 deg C and 2 %, respectively.

5.5 Procedures

At the start of each experiment, the material specimens of different composition were mounted to the cantilever beams in a random order except that pairs of identical specimens were located adjacent to one another; one was attached to the electrometer and one was on the vibrating beam. Next, the resonant frequency was determined for each beam. Scanning for resonant frequency was required for every experiment, since these values changed slightly depending on which material specimen, Teflon spacer, and Teflon screw combination was attached to a particular beam. After scanning, aluminum foil was loosely placed over the beams and the sieve/shaker box was filled with a thin (approximately 0.5 cm thick) layer of dust and leveled-off with an aluminum striker bar. The sieve/shaker box was rotated to a position to the side of the specimens, and the apparatus was placed inside an environmental chamber. The aluminum foil was removed, and specific environmental conditions were maintained for a period of approximately 24 hrs.

A few additional procedures were necessary for experiments in the vacuum chamber. After placing the apparatus in the chamber, the vacuum roughing pump was started with the valve between the pump and the chamber in the closed position. In order

to reduce the risk of dust transport caused by excess pore air pressures within the dust layer, the valve was opened slowly so that the chamber pressure decreased from 750 Torr to 1 Torr in approximately 6 hours. A that point, the valve to the scroll pump was fully opened. Vacuum rough pumping continued for approximately 8 hours. Once the pressure fell below $3x10^{-3}$ Torr, the turbo pump was activated and the internal shrouds were heated to 60 deg C for a period of typically 12 hrs. The temperature of the apparatus generally reached 50 deg. C. After bakeout, the chamber temperature was changed to the desired level at which the experiment was to be conducted. These environmental conditions were held constant for a period of at least 24 hours.

After environmental conditioning, the temperature, pressure, and humidity, prior to dust deposition and removal activities, were recorded. In the vacuum experiments, the valve to the differentially pumped residual gas analyzer was opened, and the composition of gas remaining in the vacuum chamber was recorded. The valve was closed after taking the gas composition measurement. Next, the four electrometers were momentarily grounded and the sieve/shaker box was rotated over the specimens. The sieve/shaker box was mechanically tapped, which caused dust to be deposited onto the specimens. Electrostatic charge was measured at equally spaced intervals during dust deposition. Once a thin layer of dust, discernible by the unaided human eye, was deposited on every specimen, the sieve/shaker box was again rotated to a position to the side of the specimens. A photograph of the experiment at this point is shown in Fig. 5.5.

Fig. 5.5 Freshly Deposited Dust on Specimens

Immediately after dust deposition, each beam and its specimen were vibrated individually in order to remove some of the dust. Frequency was held constant at the resonant value while amplitude was increased gradually by changing the voltage across the large electromagnet bar. In all experiments, dust removal began, as it should, at the end of the cantilever beam that is located furthest from the fixture. As amplitude was increased, the removal front moved up the cantilever beam toward the fixture. Once a distinct removal front was observed, vibrations were halted and the time, amplitude, and frequency were recorded. The same procedure of vibration excitation was repeated for each subsequent beam. Beam vibrations were conducted in random order and were

separated by approximately 5 minute time intervals. Longer duration intervals were used in the tests for the effect of dust residence time.

Following vibration and removal activities, final environmental conditions were recorded. In vacuum experiments, the turbo pump was decelerated with the valve leading to the scroll pump closed to eliminate backstreaming. The vacuum chamber was slowly backfilled with dry nitrogen over a period of approximately 6 hours in order to avoid the risk of dust transport off of the specimens, and then the chamber was opened. Distance between the fixture and the dust removal front on each beam was measured. The material specimens were carefully removed form the apparatus, placed in petri dishes, transported to the scale, and weighed. Electrostatic charge per unit dust mass and the acceleration required to remove the dust were calculated.

CHAPTER 6.0 LABORATORY RESULTS

A total of 62 vibratory dust removal experiments were conducted. A matrix that lists the variable and control parameters for different categories of experiments is provided in Tables 6.1 and 6.2. The number of experiments actually performed is shown in parenthesis next to the planned number of experiments for each category. The majority of planned vacuum and cryogenic experiments were cancelled due to budget constraints at the Jet Propulsion Laboratory. These cancelled experiments and others may be performed in later post-doctoral research. Experimental data were collected for the effects of dust residence time, humidity, cold temperature, mineral composition, particle size, and high vacuum.

6.1 Adhesion Force Calculation

It was assumed in the experiments that individual dust particles were not influenced by the number of neighboring particles. Consequently, the adhesion force for a single particle can be calculated from the removal force experienced by the particle due to its individual mass during vibration. Dust removal force was computed from amplitude and frequency of vibrations using the following relationship

$$F_a = m\ \alpha_\omega$$

where m is the mass of a dust particle and α_ω is beam acceleration at the removal point.

Table 6.1 In-Air Dust Adhesion Experiments at CSU

No. Planned No. Complete	12 (12)	8 (8)	8 (8)	5 (5)	3 (3)	12 (12)
Materials	aluminum steel	aluminum steel glass painted	aluminum steel glass painted	aluminum steel glass painted	aluminum steel glass painted	aluminum steel glass painted
Dust Simulant	70 μm Glass 90 μm Glass	70 μm Glass 90 μm Glass	70 μm Glass	70 μm Glass	70 μm Olivine	40,60,70,and 90 μm Glass
Pressure*	600 torr	600 torr	600 torr	600 torr	600 torr	600 torr
Temperature	293 deg K	293 deg K	293 deg K	253 and 273 deg K	293 deg K	293 deg K
Humidity	20-30%	20-30%	50,75, & 85%	70-90%	20-30%	20-30%
Description	Effect of Beam Position	Effect of Time	Effect of Humidity	Effect of Cold Temperature	Effect of Mineral	Effect of Particle Size

*Experiments were conducted at an elevation of approximately 1,800 m above sea level.

Table 6.2 Vacuum Dust Adhesion Experiments at JPL

No. Planned No. Complete	3 (0)	3 (1)	3 (0)	3 (1)	3 (0)	3 (2)
Materials	aluminum steel glass painted	aluminum steel glass painted	aluminum steel glass painted	aluminum steel glass painted	aluminum steel glass painted	aluminum steel glass painted
Dust Simulant	70 μm Glass	70 μm Glass	70 μm Glass	70 μm Glass	70 μm Glass	70 μm Olivine
Pressure	10^{-3} torr	10^{-6} torr	10^{-9} torr	10^{-6} torr	10^{-6} torr	10^{-6} torr
Temperature	293 deg K	293 deg K	293 deg K	333 deg K	120 deg K	293 deg K
Irradiation	none	none	none	none	none	none
Description	Effect of Low Vacuum	Effect of High Vacuum	Effect of Ultra High Vacuum	Effect of High Vacuum and Temperature	Effect of Vacuum and Cold Temperature	Effect of Vacuum and Mineral Composition

Mass of an individual dust particle was determined by assuming the particle was spherical and using 4/3 πR_n^3 times specific gravity. Beam acceleration was determined by

$$\alpha_\omega = 4\pi^2 D \omega^2$$

where D is the amplitude of vibration and ω is the frequency of vibration in cycles per second. The amplitude of vibration was found using the equation for elastic beam deflection given by

$$D = \beta_n V_n (-j^3 + 3 l^2 j - 2 l^3)$$

where β_n is the calibration constant for beam n, V_n is the measured voltage across the Wheatstone bridge, j is the distance from the free end of the cantilever beam to the dust removal front, and l is the unsupported length of the cantilever beam. This equation is derived in App. IV.

6.2 Error Analysis

With the background noise in the system, V_n could be measured to the nearest 0.005 V. The random error caused by this limit of precision is inversely proportional to the magnitude of the voltage measurement. The smallest voltage measurement recorded was 0.050 V. Hence, the error introduced by precision of the voltage measurement was less than or equal to 10%. Since the frequency of vibration was driven very precisely by a computer, no significant random error can be attributed to frequency measurement.

The standard deviation of the beam deflection calibration plots in App. IV is an indication of the precision of the calibration constant, β_n. For all beams, the standard deviation was approximately ± 0.007. The random error caused by the limit of precision of

β_n is inversely proportional to the magnitude of the calibration constants which ranged from 0.287 to 0.356. Hence, the error introduced by the precision of the calibration constants is less than or equal to 2%.

In an ideal case, all particles would exhibit the same adhesion and the material specimen would move in a uniform single-mode of vibration. The removal front for the ideal case should appear linear and perpendicular to the axis of the beam. In all of the experiments, the removal front was clearly discernable. However, it often formed different shapes as shown in Fig. 6.1. Several factors can affect the shape of the removal front. If more than one layer of dust particles is deposited onto the beam, there should exist more than one distinct removal front as shown in Fig. 6.1b. This occurrence was observed only once. Lack of uniformity in dust particle gradation is expected to cause the removal front to be less distinct, as shown in Fig. 6.1c. This behavior was slight in all experiments. Secondary modes of vibration of the specimen is expected to disrupt the lineal shape of the removal front, as shown in Fig. 6.1d. This was the predominant shape of the removal front indicating that a secondary mode of vibration was often present. Contamination on the surface of the specimens is expected to cause discontinuities in the removal front as shown in Fig. 6.1e. These discontinuities were observed rarely.

In accordance with previous laboratory work in dust adhesion measurement, the removal force was computed at the point along the beam where 50% of dust particles were removed. This point corresponds to the average distance from the beam fixture to the removal front. Errors introduced by variations in the shape of the removal front were computed for each experiment by taking the differences between the adhesion forces found

using the maximum and minimum distance from the beam fixture to the removal front and that found at the average distance from the beam fixture to the removal front. Error bars were derived for each measurement to account for both random precision errors and variations in shape of the removal front. These error bars appear in all data sets presented herein.

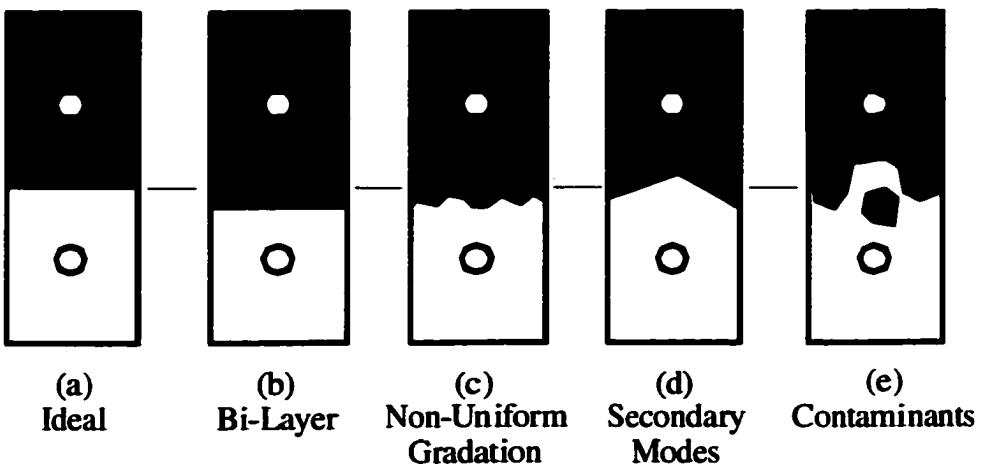

Fig. 6.1 Shape of Dust Removal Fronts

6.3 Laboratory Results

Several experiments were performed to evaluate the effect of time elapsed after dust deposition using 50 to 90 μm diameter glass spheres at 20 to 60 % relative humidity and a temperature between 20 and 22 deg C. Results of the experiments are presented in Figs. 6.2 through 6.5. The solid lines in the figures represent linear regressions. Adhesion appeared to increase with residence time on stainless steel and glass specimens. This result is consistent with the theory that adhesion increases with time for viscoelastic materials.

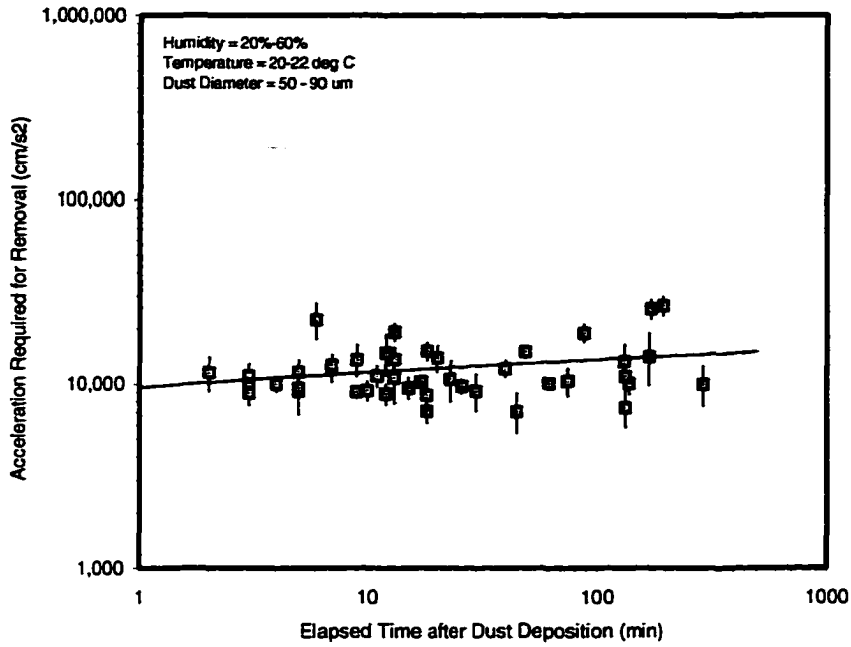

Fig. 6.2 Effect of Dust Residence Time on Adhesion of Glass Spheres to Stainless Steel

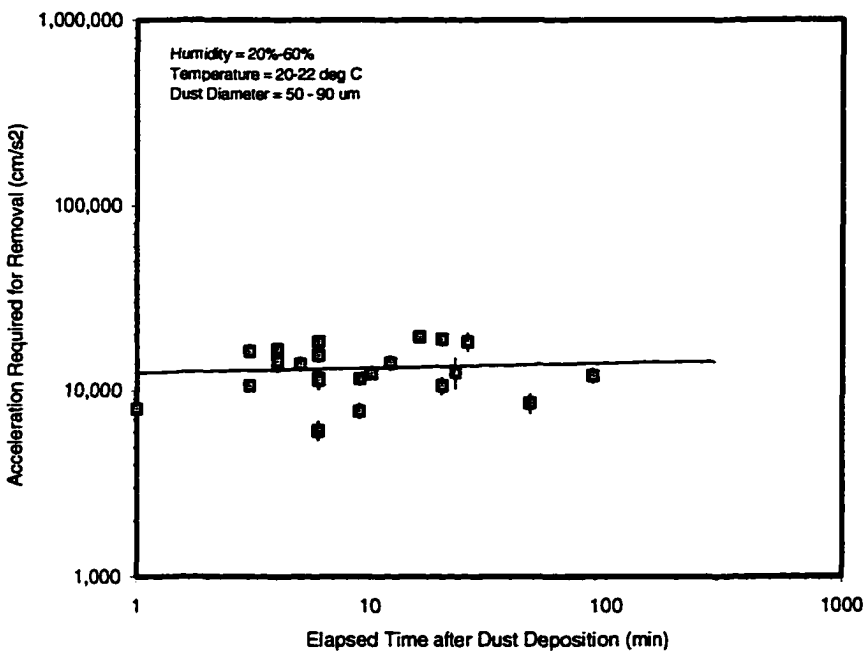

Fig. 6.3 Effect of Residence Time on Adhesion of Glass Spheres to Painted Aluminum

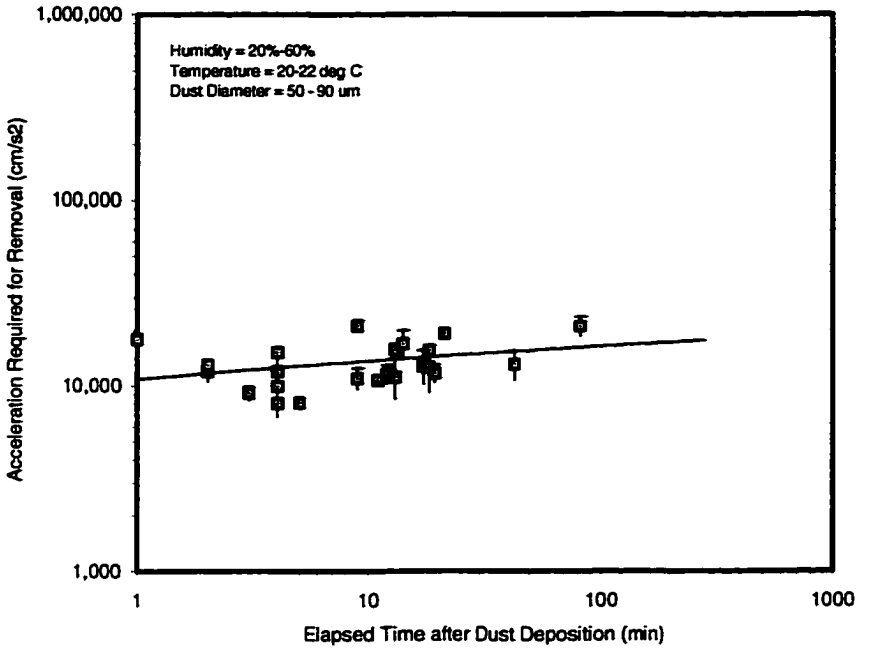

Fig. 6.4 Effect of Dust Residence Time on Adhesion of Glass Spheres to Glass

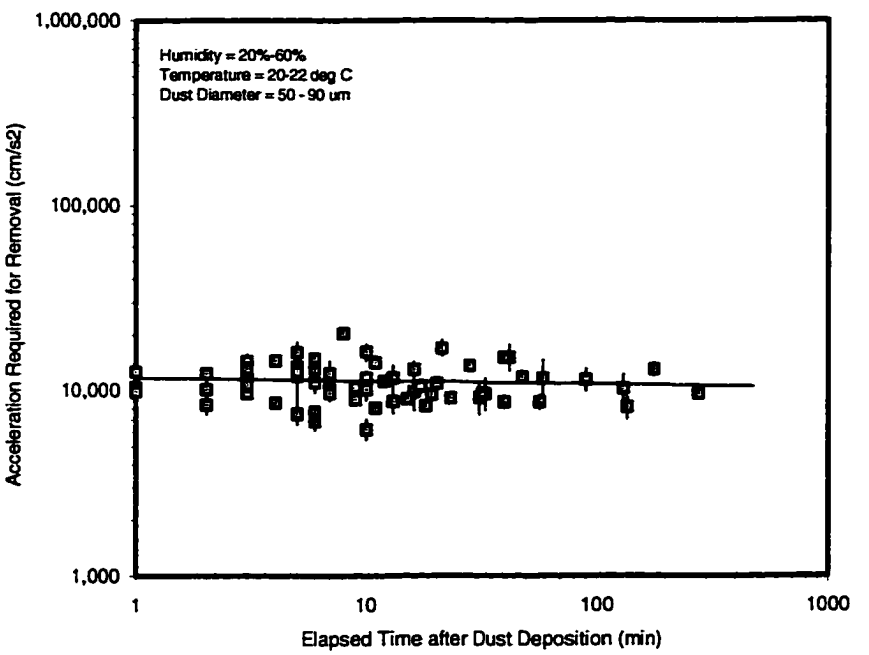

Fig. 6.5 Effect of Dust Residence Time on Adhesion of Glass Spheres to Aluminum

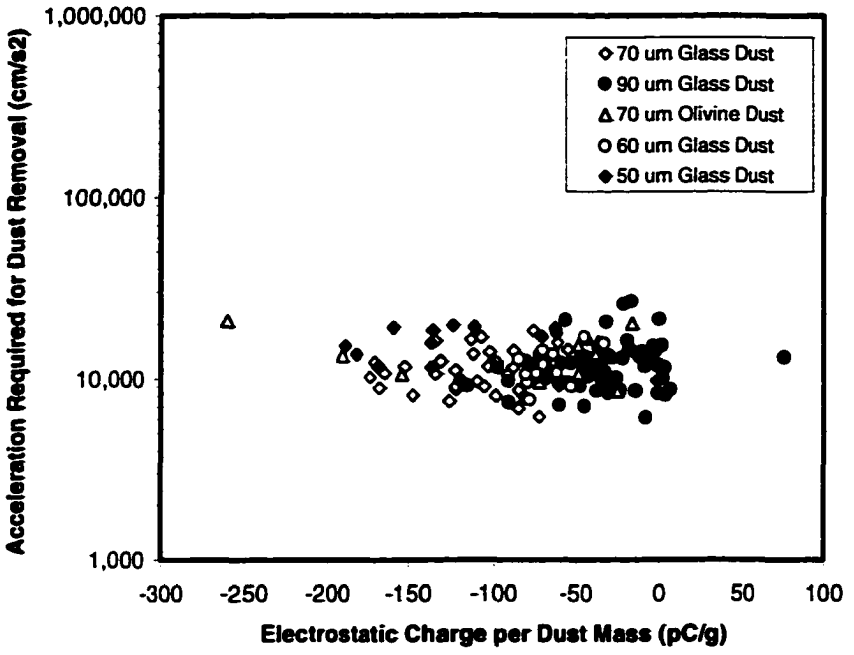

Fig. 6.6 Measured Electrostatic Charge

The total electrostatic charge measured by the electrometers during all experiments is shown in Fig. 6.6. As can be seen in the figure, the dust was almost always negatively charged. Olivine dust, shown by the open triangles in the figure, exhibited the highest degree of variability in electrostatic charge which ranged from -706 to +533 pC/g. The average electrostatic charge carried by the glass spheres was inversely proportional to the dust diameter as shown in Table 6.3.

Removal acceleration results for experiments using 50 to 90 μm diameter glass spheres in-air at a temperature of 20 to 22 deg C and at different levels of relative humidity are shown in Figs. 6.7 through 6.10. The solid lines in the figures represents exponential regressions. The time elapsed after dust deposition varied but was less than 30 to 300

minutes for the data shown. Adhesion to all materials except painted aluminum increased with higher humidity. Adhesion to glass surfaces exhibited the strongest correlation with humidity.

Table 6.3 Average Electrostatic Charge of Glass Spheres

Average Glass Sphere Diameter	Average Electrostatic Charge
90 μm	-29 pC/g
69 μm	-40 pC/g
58 μm	-69 pC/g
49 μm	-113 pC/g

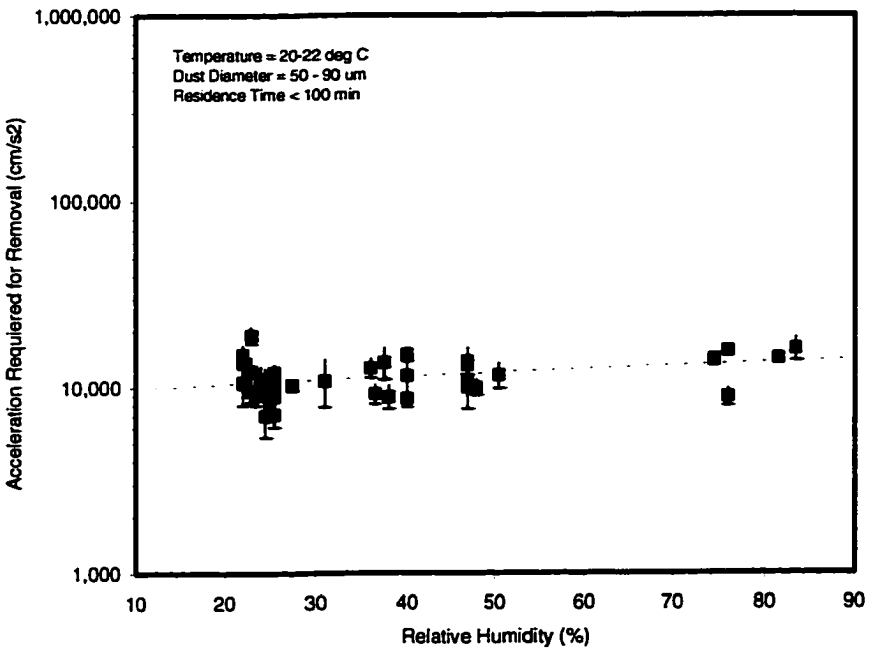

Fig. 6.7 Effect of Relative Humidity on Adhesion of Glass Spheres to Stainless Steel

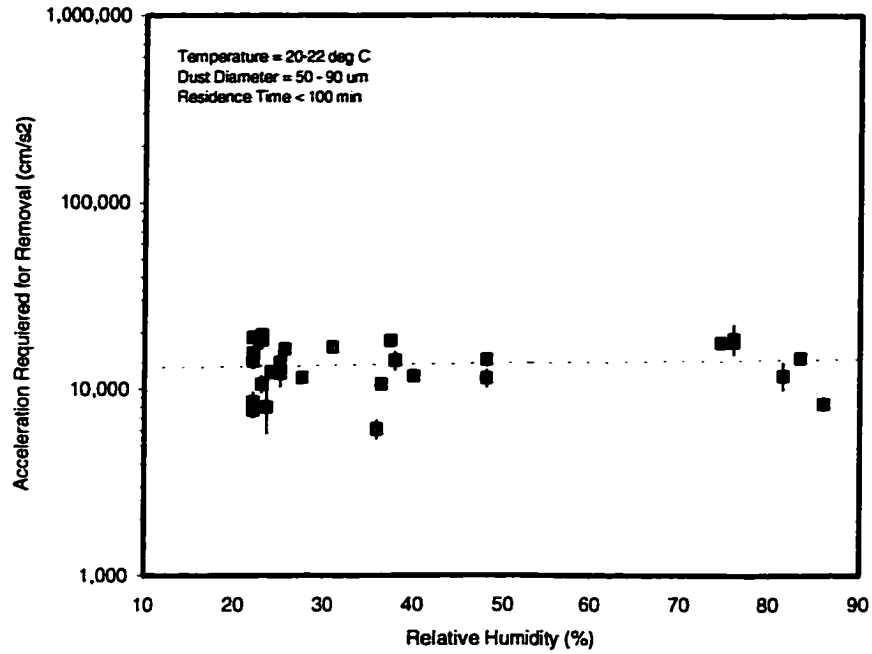

Fig. 6.8 Effect of Relative Humidity on Adhesion of Glass Spheres to Painted Aluminum

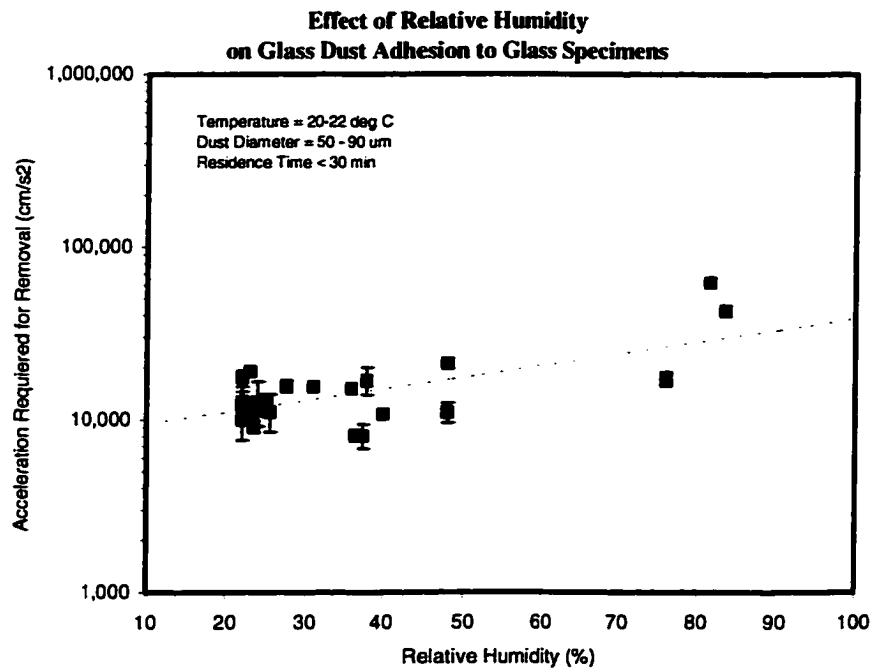

Fig. 6.9 Effect of Relative Humidity on Adhesion of Glass Spheres to Glass

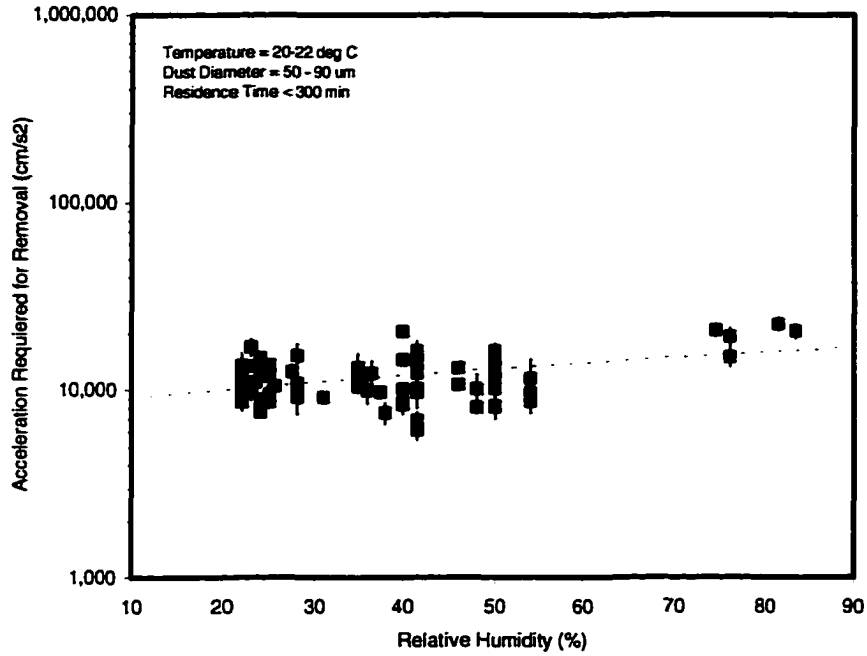

Fig. 6.10 Effect of Relative Humidity on Adhesion of Glass Spheres to Aluminum

Several experiments were conducted using 50 to 90 μm diameter glass spheres in-air within the walk-in freezer. Direct measurements of humidity were not taken in the freezer. However, evidence of frost accumulation on the aluminum dust shields during the experiment suggests that relative humidity was high. The results of experiments conducted at cold temperatures are compared to experiments conducted at standard room temperature in Figs. 6.11 through 6.14. Except for glass surfaces, adhesion exhibited a minimum value near 0 deg C and then increased at colder temperature. Adhesion to glass appeared to show a slightly opposite effect.

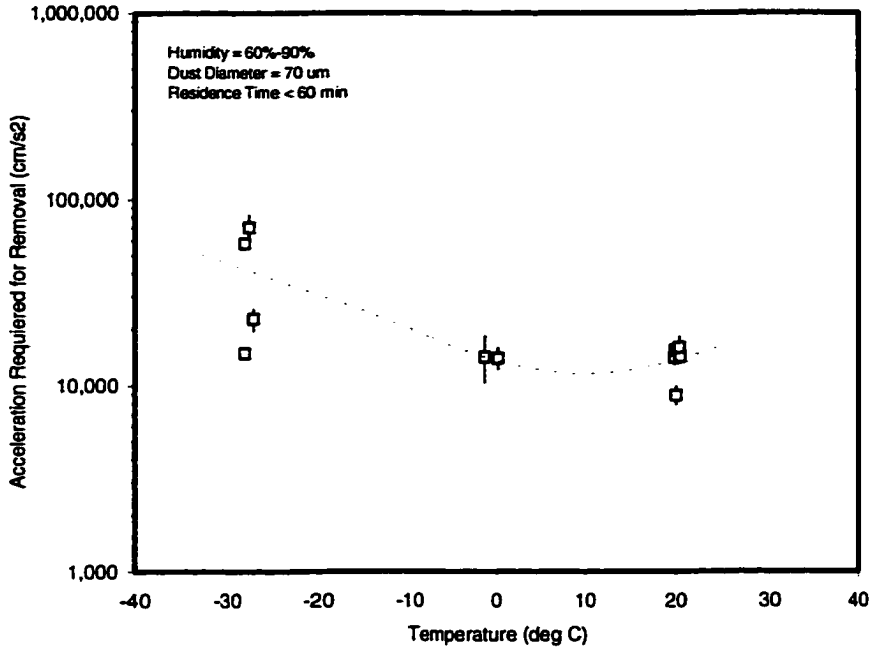

Fig. 6.11 Effect of Cold Temperature on Adhesion of Glass Spheres to Stainless Steel

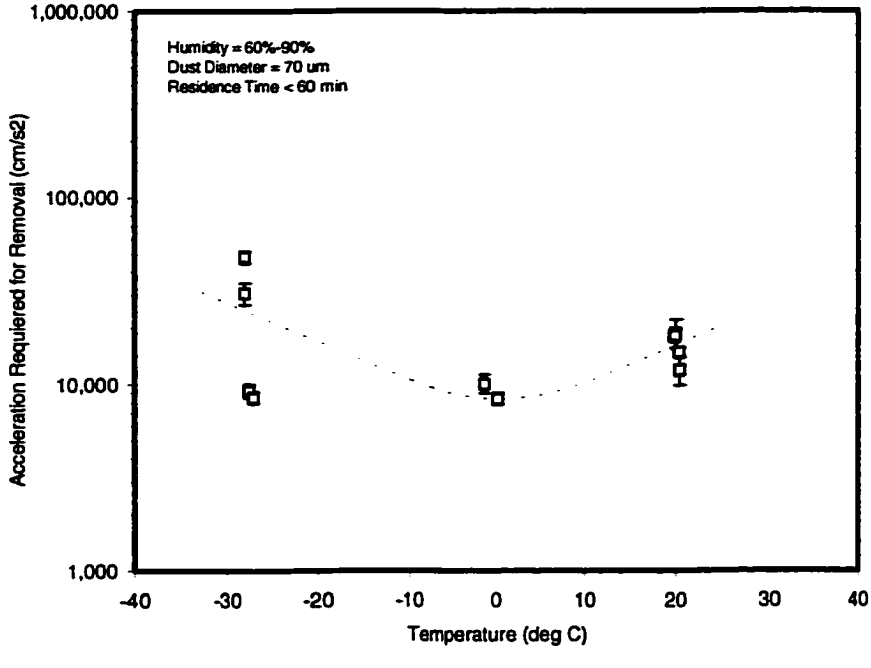

Fig. 6.12 Effect of Cold Temperature on Adhesion of Glass Spheres to Painted Aluminum

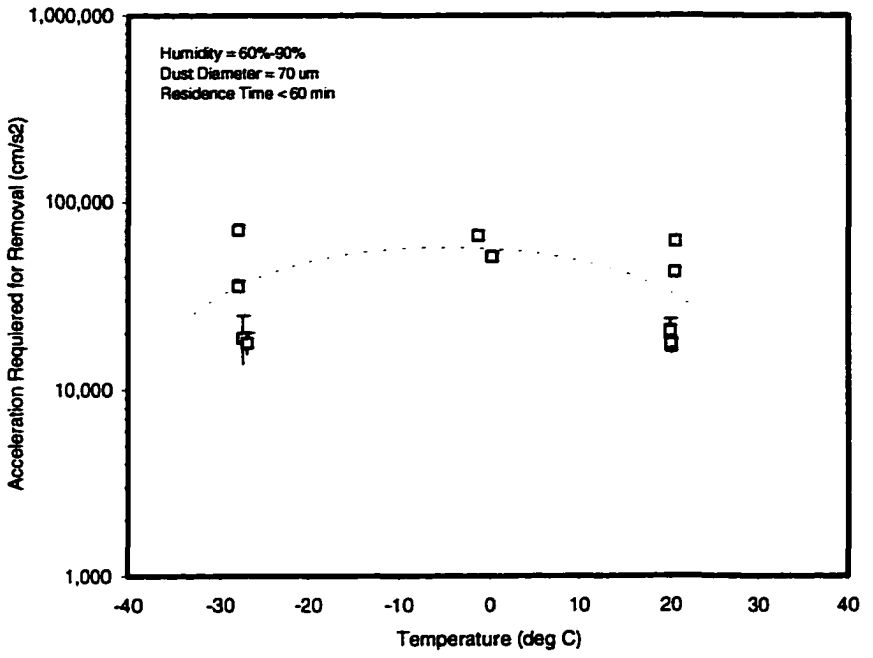

Fig. 6.13 Effect of Cold Temperature on Adhesion of Glass Spheres to Glass

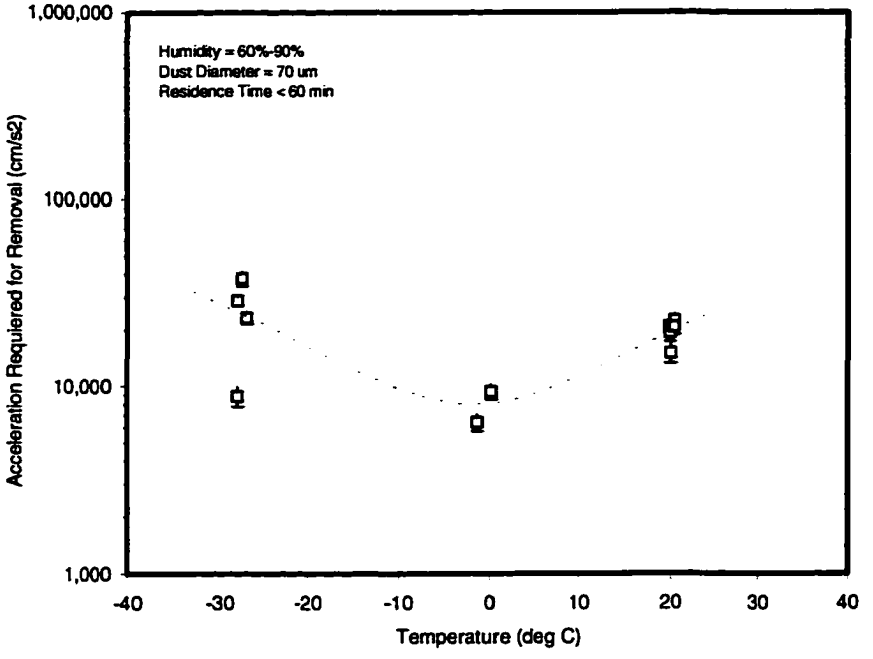

Fig. 6.14 Effect of Cold Temperature on Adhesion of Glass Spheres to Aluminum

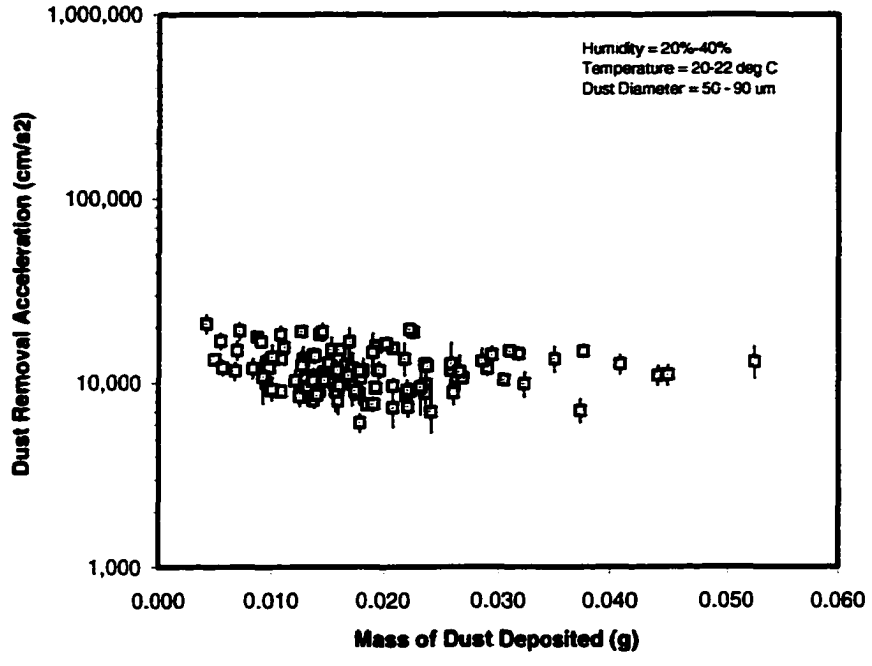

Fig. 6.15 Mass of Dust Deposited on Material Specimens

All measurements of removal acceleration for 50 to 90 μm diameter glass spheres on the four different material specimens at 20 to 22 deg C and at a humidity of 20 to 40% are shown in Fig. 6.15. As can be seen in the figure, dust adhesion was not affected by the total mass of dust deposited, which indicates that the adhesion of individual particles was not affected by the number of neighboring particles. The mass of dust that corresponds to an ideal, closely-packed complete monolayer is equal to 0.105 g. Hence, the amount of dust deposited during the experiments was less than an ideal monolayer.

The results of experiments conducted using four different particle size gradations of glass spheres in-air at 20 to 22 deg C and at 22 to 28% relative humidity are shown in Figs. 6.16 through 6.19. All data points were obtained for dust residence times less than 30 min.

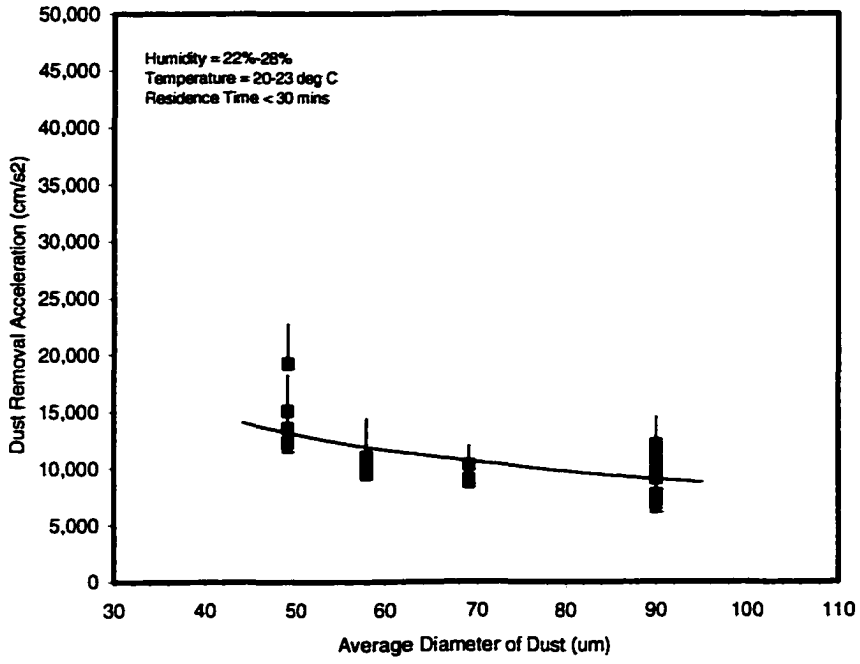

Fig. 6.16 Effect of Glass Sphere Diameter on Removal Acceleration for Stainless Steel

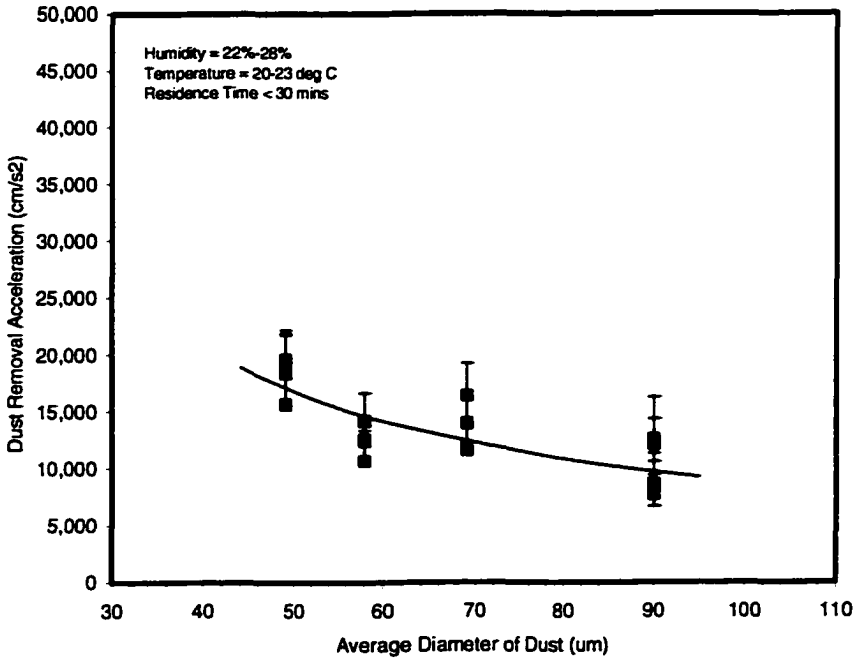

Fig. 6.17 Effect of Glass Diameter on Removal Acceleration for Painted Aluminum

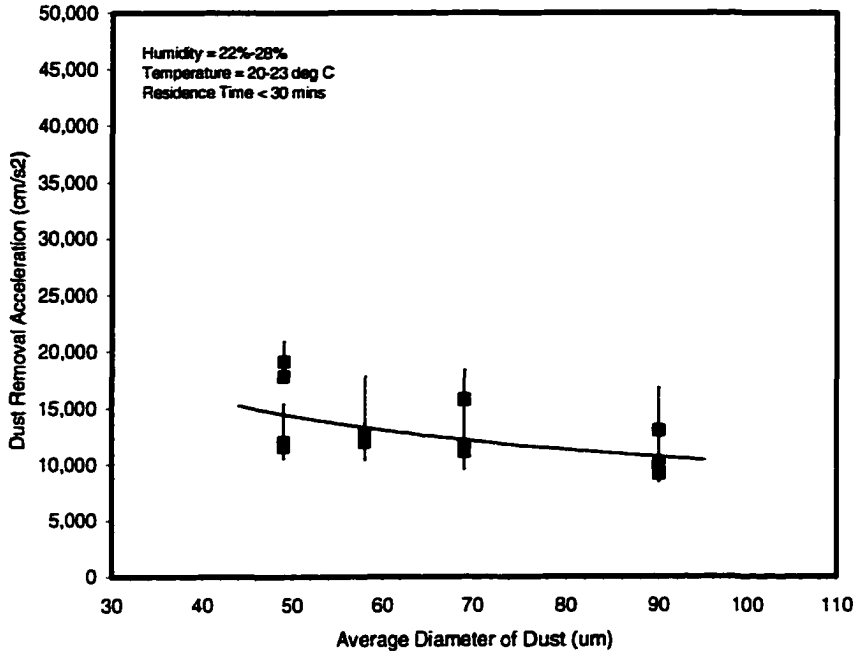

Fig. 6.18 Effect of Glass Sphere Diameter on Removal Acceleration for Glass

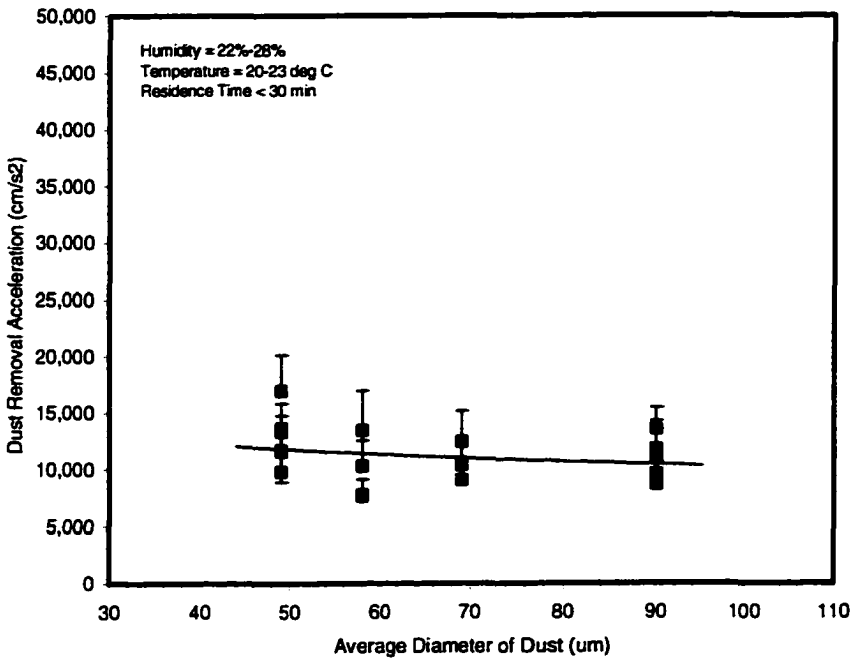

Fig. 6.19 Effect of Glass Sphere Diameter on Removal Acceleration for Aluminum

The acceleration required for dust removal increased with smaller sized dust particles for all four material specimens. The trend was most distinct on painted aluminum and least distinct on aluminum.

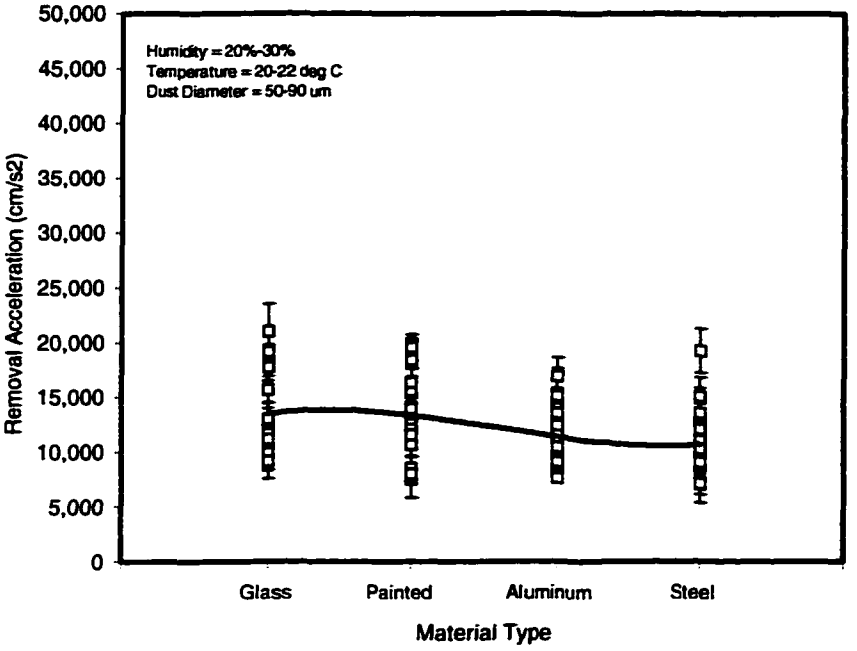

Fig. 6.20 Material Specimen Composition Differences

Acceleration required for dust removal and, hence, dust adhesion differed only slightly between the four different specimens, as shown in Fig. 6.20. These data were collected in-air at a temperature of 20 to 22 deg C and at a relative humidity between 20 and 30 %. The average acceleration required for removal of glass dust on glass and painted surfaces was on the order of 1.5 times that required for glass dust on aluminum and steel surfaces. A similar review of data collected for olivine dust on the four different material specimens, indicates that approximately 1.5 times greater acceleration is required to remove glass dust from glass

surfaces as compared with painted aluminum, aluminum, and steel.

Only three dust removal experiments were conducted in high vacuum at a temperature between 20 and 29 deg C. Data collected are compared with results obtained in-air at 32 to 46% relative humidity in Figs. 6.21 and 6.22. High vacuum appeared to cause an increase in the adhesion of glass spheres to stainless steel specimens and a decrease in adhesion of glass spheres to painted aluminum specimens. The adhesion of olivine dust to all specimens decreased in high vacuum.

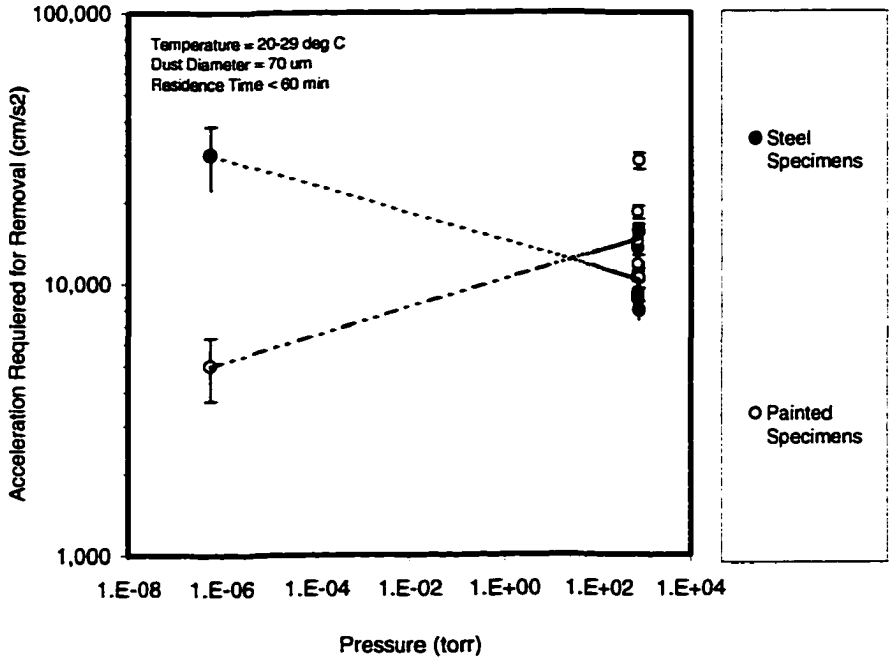

Fig. 6.21 Adhesion of Glass Spheres in High Vacuum

One experiment was conducted using glass spheres in high vacuum at a temperature of 44.5 deg C. An experiment was not conducted at the same temperature in air. The adhesion exhibited by the glass spheres was less in high vacuum at high temperature than that

in-air at standard room temperature and a humidity between 32 to 46% for all material specimen except glass, which had approximately the same adhesion in both environments.

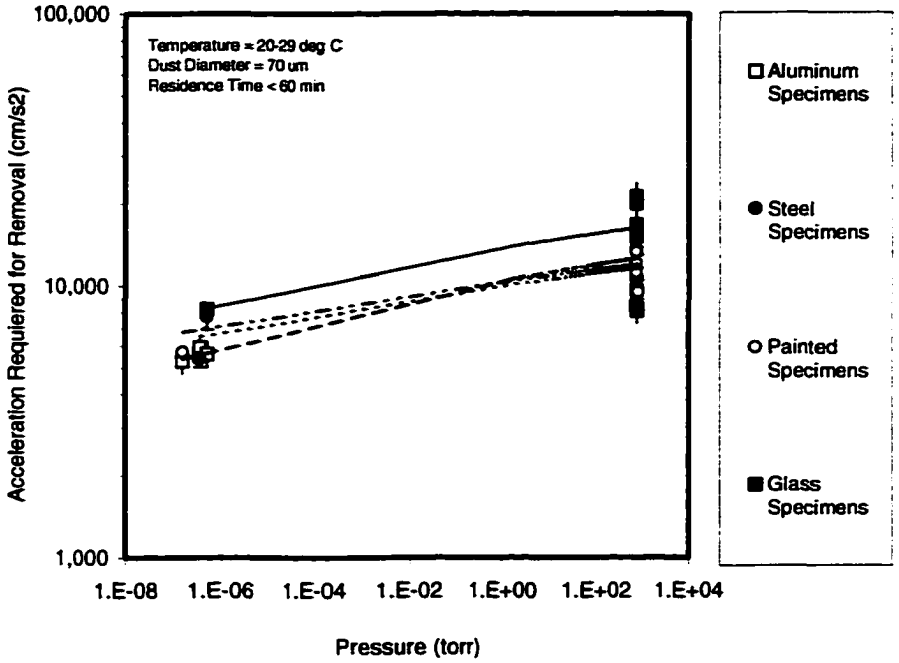

Fig. 6.22 Adhesion of Olivine Dust in High Vacuum

CHAPTER 7.0 MODEL COMPARISONS & DISCUSSION

Gas adsorption at different levels of humidity and within atmospheres of varied composition is discussed. Physical chemical properties necessary for input in the model are computed. The model is compared with results of laboratory experiments presented in Chapter 6. The model is shown to match the general trend and magnitude of laboratory measurements fairly well.

7.1 Gas Adsorption

According to generalized Lifshitz theory (Israelachvili, 1992), the Hamaker Coefficient between two solids separated by an interior medium is given by

$$A = A_{V=0} + A_{V>0}$$

where $A_{v=0}$ is the dipole and induced dipole component given by

$$A_{V=0} = \frac{3}{4}kT\left(\frac{\epsilon_1 - \epsilon_3}{\epsilon_1 + \epsilon_3}\right)\left(\frac{\epsilon_2 - \epsilon_3}{\epsilon_2 + \epsilon_3}\right)$$

and $A_{v>0}$ is the dispersion component given by

$$A_{V>0} = \frac{3h\nu_e}{8\sqrt{2}} \frac{(n_1^2 - n_3^2)(n_2^2 - n_3^2)}{(n_1^2 + n_3^2)^{1/2}(n_2^2 + n_3^2)^{1/2}[(n_1^2 + n_3^2)^{1/2} + (n_2^2 + n_3^2)^{1/2}]}$$

where k is the Boltzmann Constant, ϵ_1, ϵ_2, and ϵ_3 are dielectric constants of the two

interacting surfaces and the interior medium, respectively, h is the Plank Constant, ν_e is ionization frequency, and n_1, n_2, and n_3 are refractive indices of the two interacting surfaces and the interior medium, respectively.

Physical-chemical properties of the two dust types and the material surfaces used in the experiments are described in Chapter 5. The static dielectric constant, index of refraction for visible light, and surface energy for several adsorbed substances are given in Table 7.1. The dielectric constant for all substances and the index of refraction of water are from CRC (1997). The index of refraction for most substances except water and ferromagnetic materials is approximately equal to the square root of the dielectric constant (Fishbane, Gasiorowicz, and Thornton, 1993). Values of index of refraction shown in the table for substances other than water were computed using this relationship. Surface energy is from Adamson (1990).

Using the properties listed in Tables 5.1 and 7.1 and the generalized Lifshitz theory given above, Hamaker Coefficients between the two dust types and the four material specimens were calculated across an interior medium consisting of air/vacuum or of various interior media. Resulting values are shown in Table 5.2. A relative dielectric constant of 8 was assumed for the olivine dust. An ionization frequency of $3x10^{15}$ s^{-1} was assumed for all materials. Temperature and interior medium used in the calculations are listed in the 2nd and 3rd columns. The interior medium was assumed to be in either liquid or solid state. Temperature only affects the dipole and induced dipole Hamaker term which is small for the interaction of solids across air or vacuum. Temperature slightly affects Hamaker values with water or ice as the interior medium. The considerable reduction in Hamaker Coefficient due to the presence of an adsorbed interior medium compared to that across vacuum or air is

apparent in the tabulated values. Hydrogen and helium affect the Hamaker Coefficient less than other types of adsorbate.

Table 7.1 Chemical Properties of Adsorbed Substances

Substance	Temperature *(K)*	Dielectric Constant	Index of Refraction	Surface Energy *(mN/m)*
Liquid Argon	140	1.32	1.15	12.0
Liquid Carbon Dioxide	293	1.45	1.20	unk
Liquid Nitrogen	75	1.47	1.21	9.4
Liquid Helium	2	1.05	1.02	0.4
Liquid Oxygen	77	1.56	1.25	16.1
Liquid Hydrogen	20	1.28	1.13	2.0
Liquid Methane	110	1.68	1.30	13.7
Liquid Water	313	73.2	1.330	69.6
Liquid Water	293	80.2	1.332	72.8
Water Ice	273	88	1.333	75.6
Water Ice	270	88	1.333	110

Table 7.2 Computed Lifshitz Hamaker Coefficients for Test Materials

Dust Type	Interior Medium	Temp. (K)	Hamaker Coefficient for Surface (10^{-20} J)			
			Painted Aluminum	Aluminum	Stainless Steel	Glass
Fused Quartz	H_2O	313	1.10	-0.45	2.65	1.09
	H_2O	293	1.18	-0.38	2.87	1.18
	H_2O	273	1.05	-0.43	2.62	1.04
	H_2O	270	1.04	-0.42	2.62	1.04
	CO_2	293	2.63	1.03	6.19	2.65
	Ar	140	3.54	1.65	7.56	3.56
	CH_4	110	1.16	0.04	3.62	1.17
	N_2	75	2.42	0.82	5.82	2.42
	O_2	77	1.80	0.41	4.79	1.80
	H_2	20	3.94	1.91	8.11	3.94
	He	2	6.69	4.12	11.79	6.67
	Vacuum	293	7.34	4.78	12.69	7.36
Olivine	H_2O	313	1.66	-0.51	4.84	1.65
	H_2O	293	1.80	-0.43	5.08	1.79
	H_2O	273	1.62	-0.52	4.78	1.61
	H_2O	270	1.62	-0.52	4.78	1.61
	CO_2	293	3.71	1.48	8.78	3.75
	Ar	140	4.78	2.23	10.22	4.80
	CH_4	110	1.88	0.07	5.89	1.90
	N_2	75	3.45	1.17	8.32	3.46
	O_2	77	2.69	0.61	7.18	2.70
	H_2	20	5.22	2.53	10.79	5.23
	He	2	8.28	5.10	14.68	8.28
	Vacuum	293	9.03	5.88	15.68	9.06

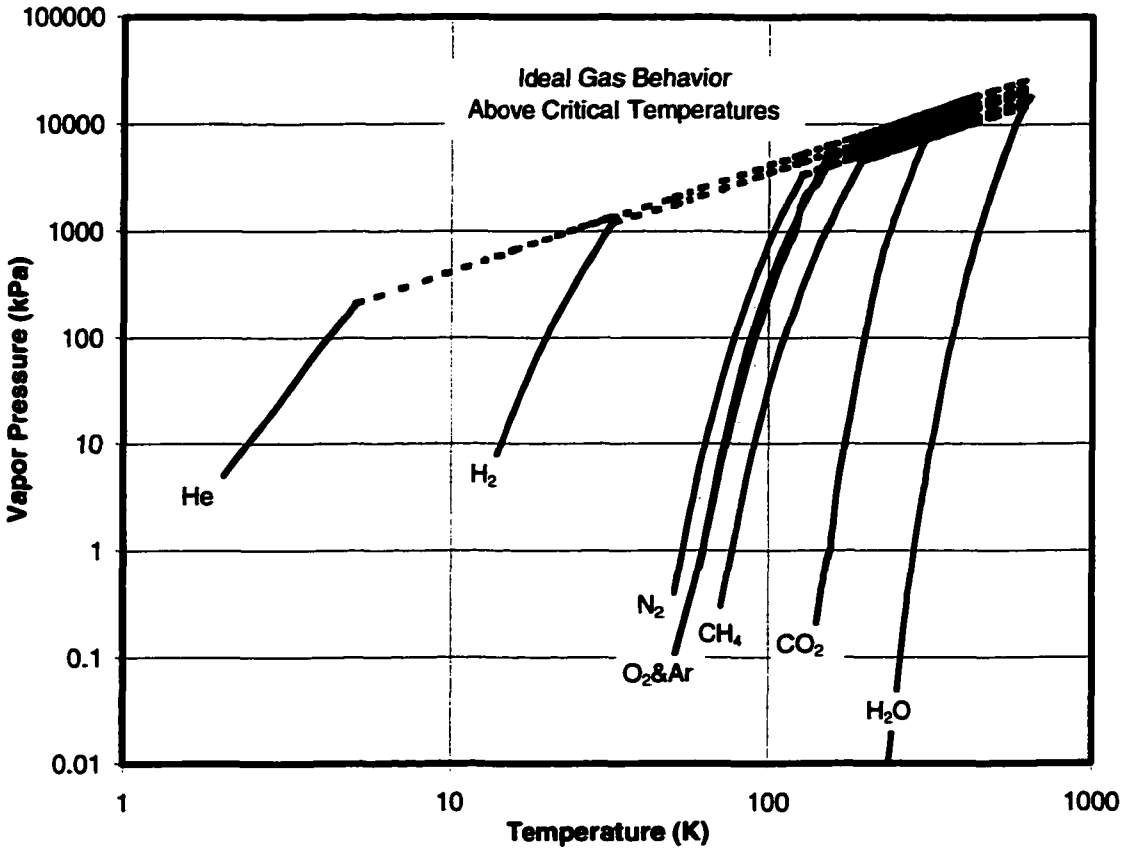

Fig. 7.1 Liquid and Solid Vapor Pressures of Common Gasses

The vapor pressure of common adsorbates is given in Fig. 7.1. Above critical temperatures, gasses behave like a compressible fluid and a transition between liquid and gas or between solid and gas is absent. Adsorption is thought not to occur above the critical temperature of a gas (Adamson, 1990). Perko (1996) reviewed past desorption spectra for vacuum outgassing of granular media and pointed to the presence of gasses in the spectra at temperatures far above their respective critical temperatures. Perko used this observation to argue that adsorption occurs above critical temperatures and that adsorbate thickness between particle contacts can be calculated using a potential energy solution, similar to that derived

in Chapter 4, with the adsorption energy set equal to that required to compress a gas to its adsorbed molar volume. This was accomplished herein by defining an effective "vapor pressure", P_o^*, based on the ideal gas law, given by

$$P_o^* = \frac{R\,T}{V_L}$$

where R is the Ideal Gas Constant, T is temperature, and V_L is adsorbed molar volume. Effective vapor pressure, shown by dashed lines, is plotted as a function of temperature for each adsorbate in Fig. 7.1. Values of P_o^* can be directly substituted for P_o in the adsorption model developed in Chapter 4 when temperatures exceed critical values. Effective vapor pressure can not be used to obtain capillary radius since the surface energy of the adsorbed layer with ambient vapor is zero when a transition to liquid or solid phase is nonexistent.

The sea-level composition of air on Earth is shown in Table 7.3 by percent volume. Partial pressure of each component was computed according to the ideal gas law at standard atmospheric pressure (101 kPa). These partial pressures were used in combination with the effective partial pressures shown in Fig. 7.1 to compute the thickness of adsorbed gas between a glass dust particle and a glass surface. Furthermore, the thickness of adsorbate in an atmosphere of pure nitrogen was also computed using the model. Results are shown in Fig. 7.2. As can be seen in the figure, preferential adsorption of gasses other than water occurs below a relative water vapor humidity of about 0.6%. Hence, van der Waals forces that may occur in vacuum are shielded from occurring in dry air and in an atmosphere of pure nitrogen.

Table 7.3 Major Components of Air at Sea-Level (CRC, 1997)

Gas	Volume Fraction	Partial Pressure (kPa)
Nitrogen	78.08%	79
Oxygen	20.95%	21
Argon	0.93%	0.94
Caron Dioxide	0.03%	0.03

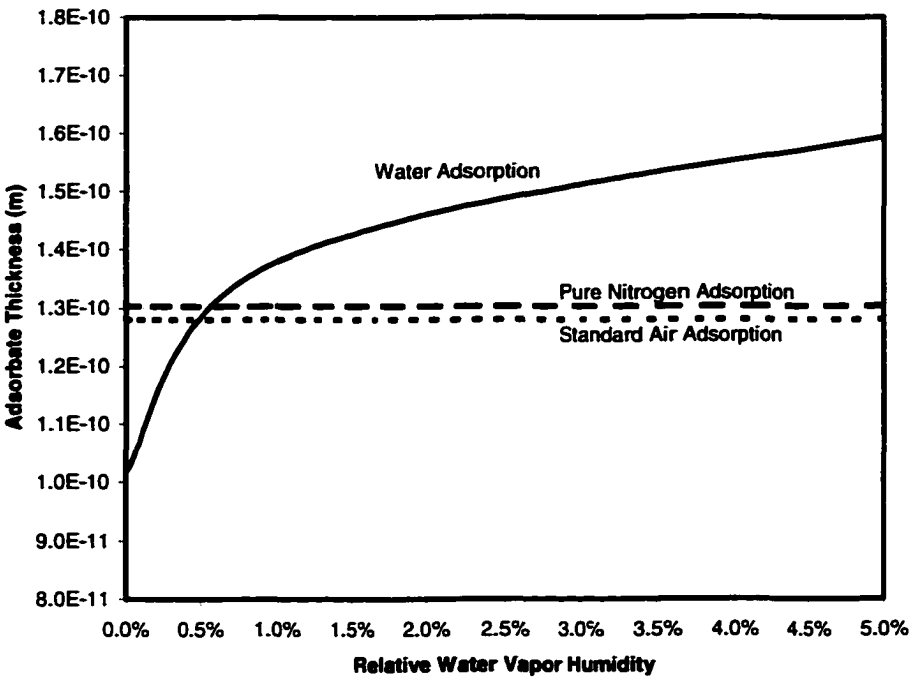

Fig. 7.2 Adsorbate Thickness in Air and Pure Nitrogen

7.2 Model Comparisons

The model was compared to laboratory measurements of adhesion at different levels of relative water vapor humidity. The electrostatic component of adhesion, which is discussed in a later section, was assumed small. Glass dust particles were assumed to be

characterized by the same Young Modulus and Poisson Ratio as given for glass plates in Chapter 6. Average diameter of the majority of particles used in the experiments was used to compute effective particle radius. Surface roughness was neglected. Results of the model comparison are shown in Figs. 7.3 through 7.6. For the humidity levels used in the experiment, the computed capillary force as much greater than the van der Waals contribution. The majority of laboratory measurements were slightly below model predictions. This may have been due to secondary modes of vibration contributing to removal.

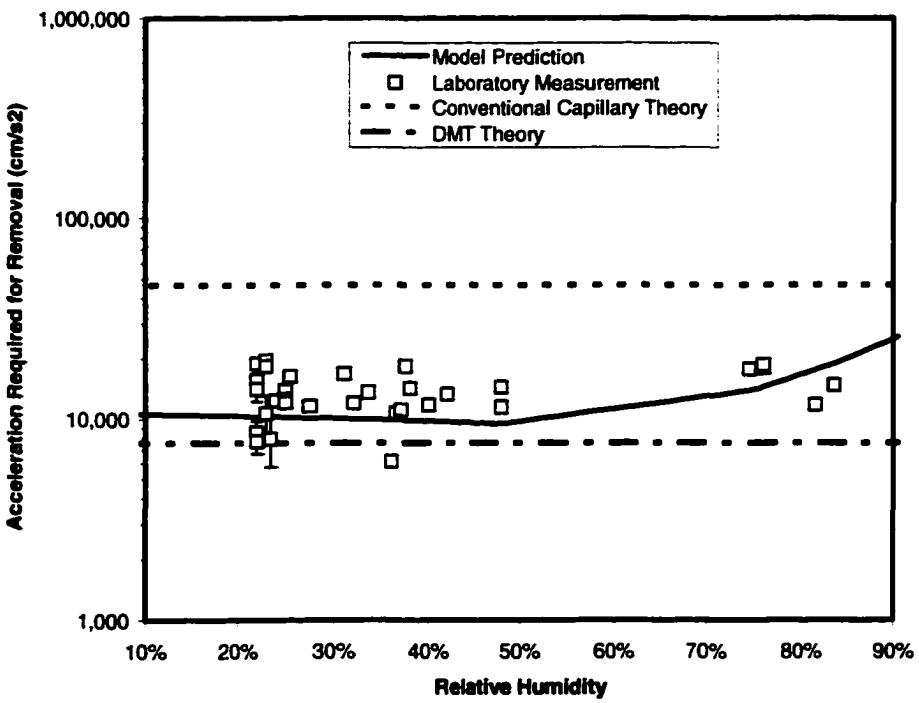

Fig. 7.3 Model Comparison for Dust on Painted Aluminum Surfaces in Humid Air

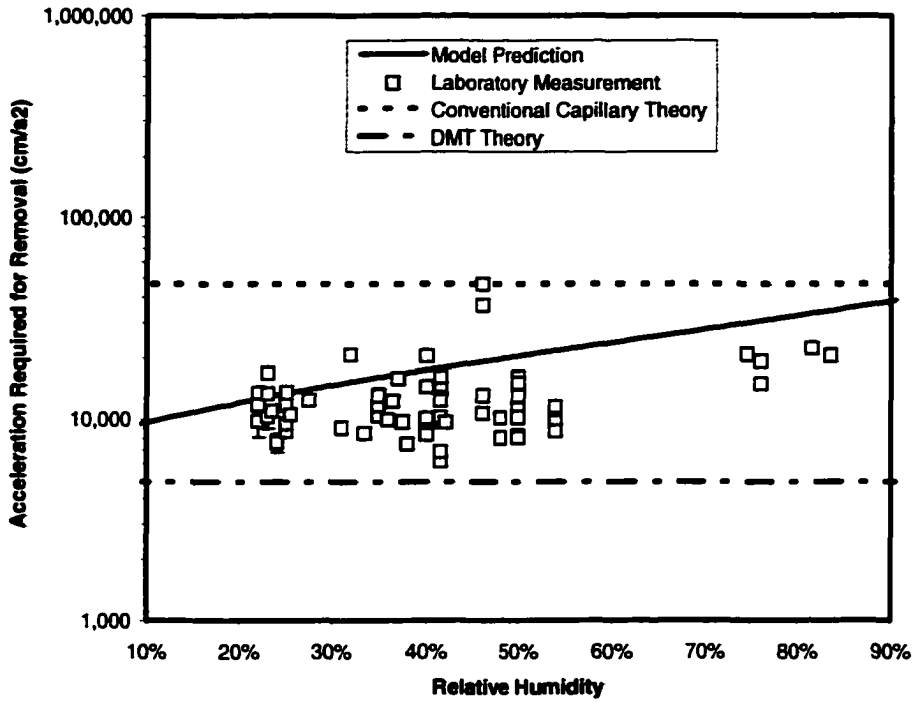

Fig. 7.4 Model Comparison for Dust on Aluminum Surfaces in Humid Air

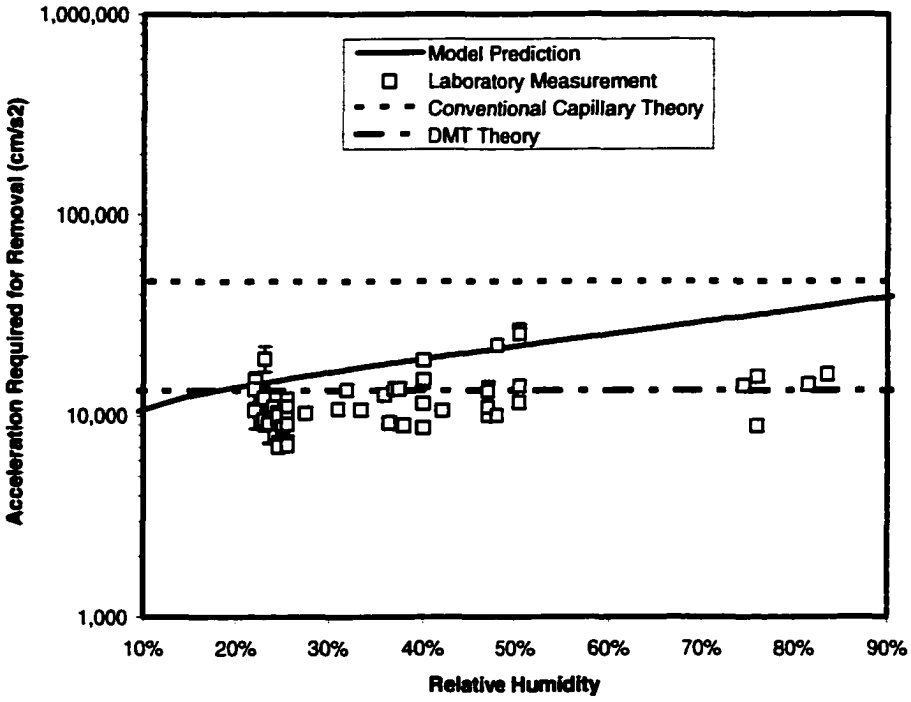

Fig. 7.5 Model Comparison for Dust on Stainless Steel Surfaces in Humid Air

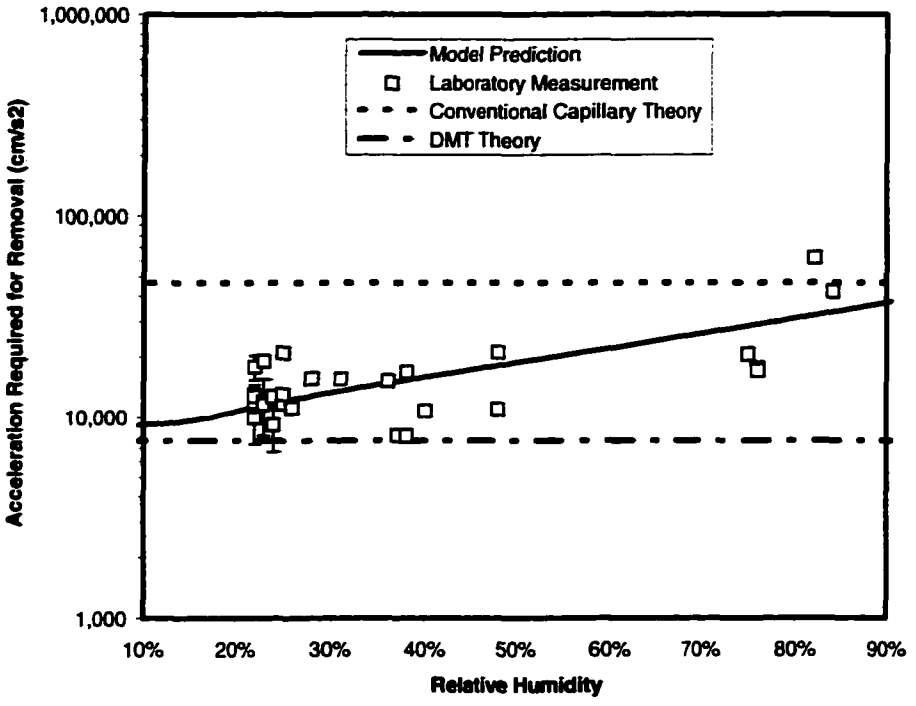

Fig. 7.6 Model Comparison for Dust on Glass Surfaces in Humid Air

The main difference in the shape of model prediction curves shown in Figs. 7.3 through 7.6 is due to differences in the Young Modulus of the surfaces. At high humidity levels, the model predicts a linear correlation between the natural logarithm of required removal acceleration and relative water vapor humidity. The flatter portion of the curve predicted for painted specimens is due to the intersection of the capillary pendular ring with the contact radius. Painted specimens are thought to have the lowest value of Young Modulus, and, therefore, this intersection occurs at much higher levels of humidity.

The upper dashed lines in Figs. 7.3 through 7.6 depict the adhesion force predicted by conventional capillary models based on Type A pendular ring behavior. The lower dashed line in the figures represents the adhesion based on the DMT model, which accounts for van

der Waals forces only. The new model appears to match the experimental data better than either of these two earlier models.

Several dust adhesion experiments were performed in a walk-in freezer to evaluate the effect of temperature on adhesion. It has been suggested by earlier theoretical research, as described in Chapter 3, that particle adhesion is increased at temperatures below the freezing point of water due to the formation of sintered necks of ice between particle asperities. The model is compared with the data generated at cold temperatures in Figs. 7.7 through 7.10. In these experiments, the humidity at 273 deg K was measured directly with a digital humidity gauge. Relative water vapor humidity at this temperature ranged from 65 to 70%. The humidity level at 245 deg K was not measured directly due to the temperature limit of the humidity gauge. However, a small amount of frost formed on the aluminum dust shields indicating high humidity during the experiments conducted at this temperature. A relative humidity of 95% was assumed in the calculations. The laboratory data listed at standard room temperature was obtained at a relative humidity of between 20 and 30%. As such, the data in the figures represent a combined effect of variations in temperature and relative humidity. Much of the increase in adhesion predicted by the model is due to the increase in relative humidity levels that occurred at cold temperatures. Nonetheless, altered adhesion due to a change in phase of the capillary pendular ring was not detected, since model predictions, which account only for the change in size of the pendular ring at the environmental conditions imposed, closely match laboratory results.

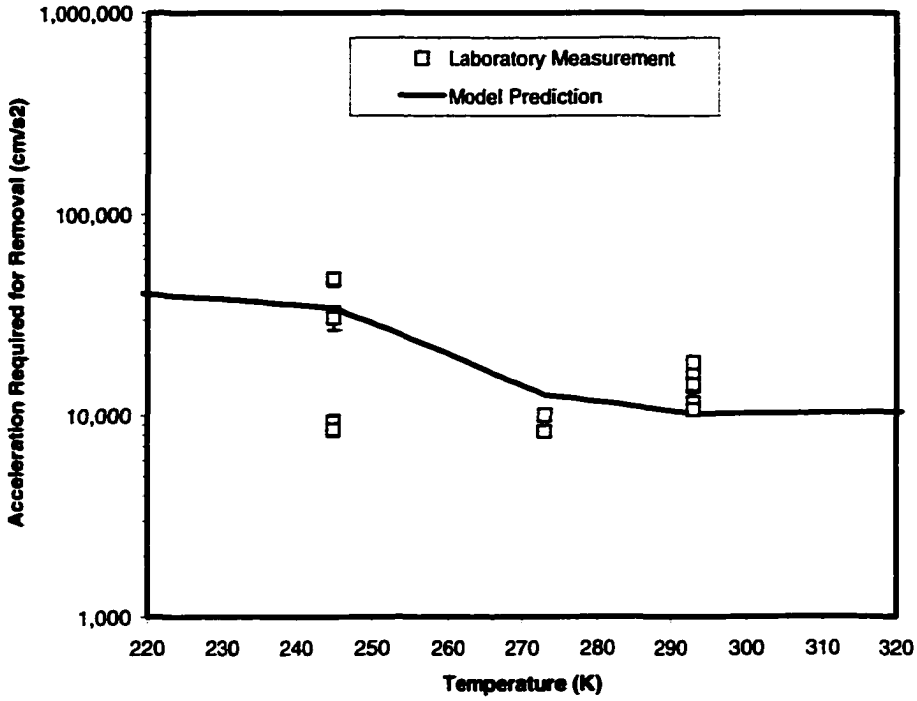

Fig. 7.7 Model Comparison for Dust on Painted Surfaces at Different Temperatures

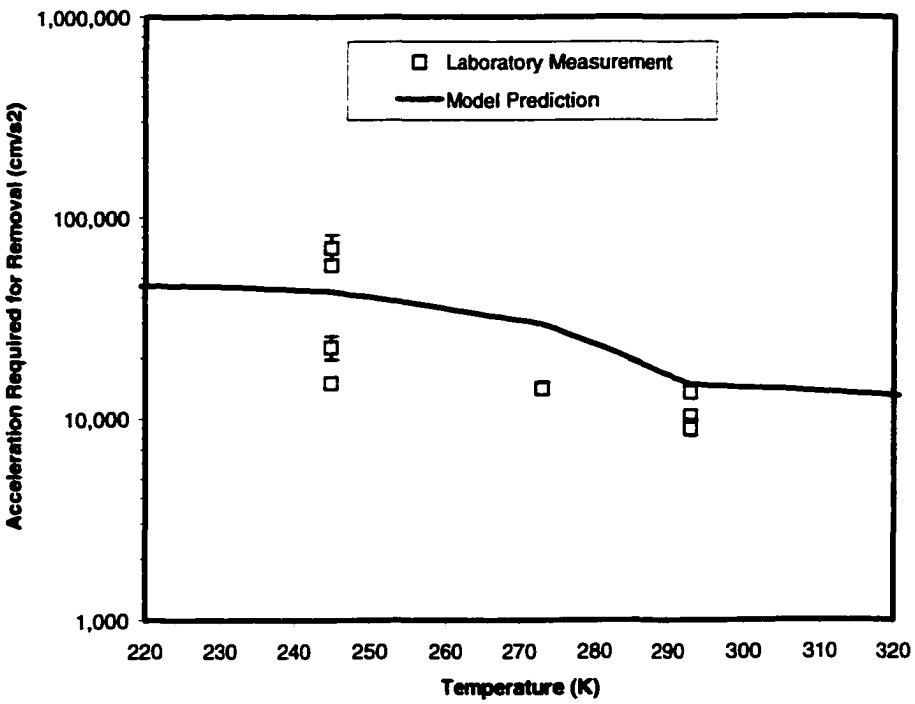

Fig. 7.8 Model Comparison for Dust on Aluminum Surfaces at Different Temperatures

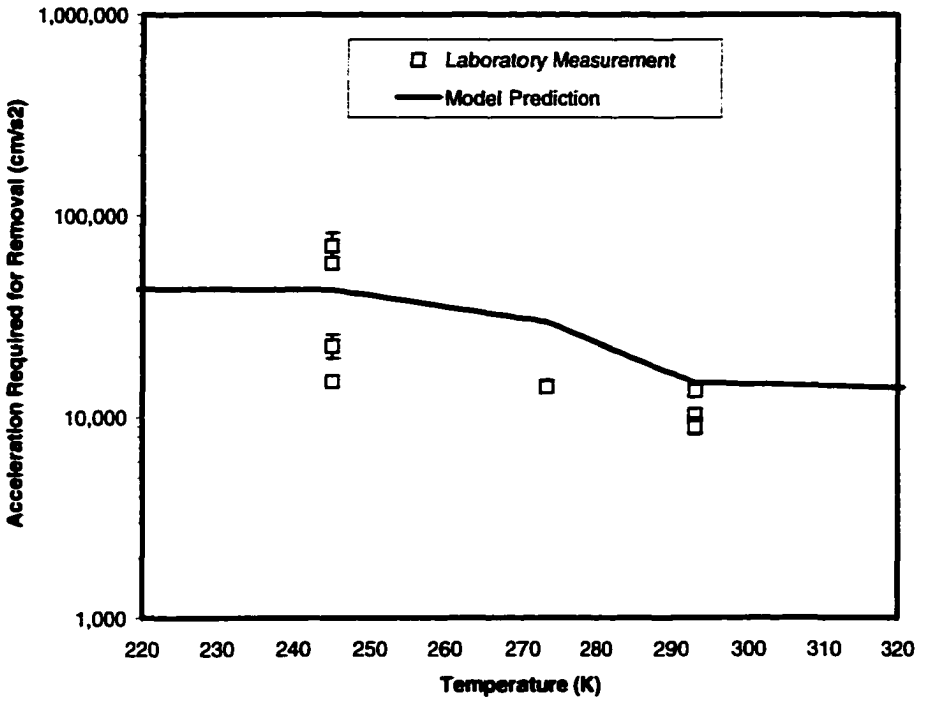

Fig. 7.9 Model Comparison for Dust on Aluminum Surfaces at Different Temperatures

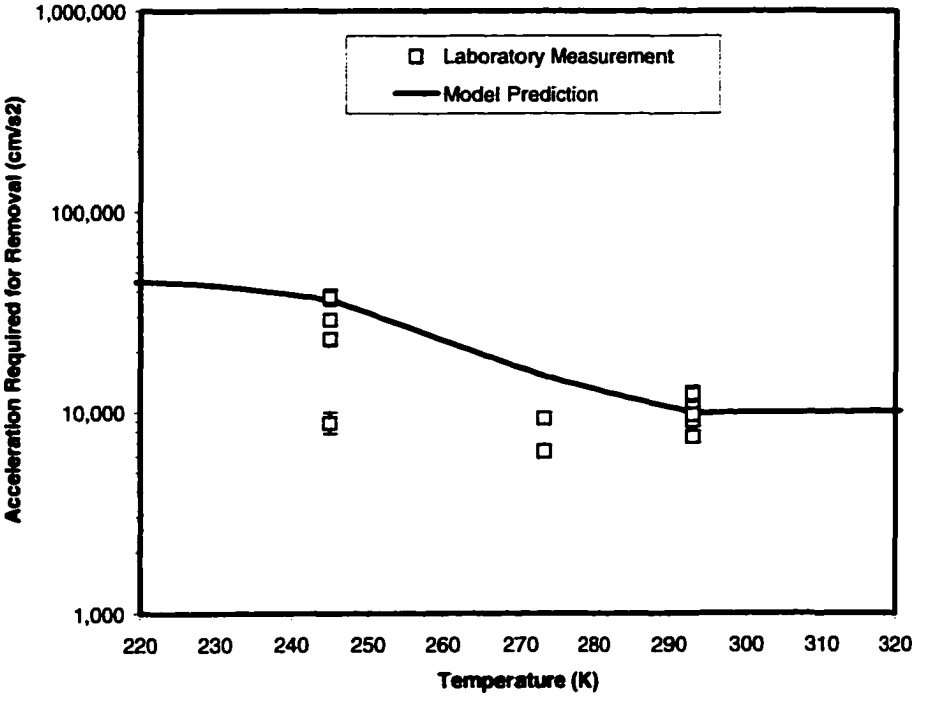

Fig. 7.10 Model Comparison for Dust on Aluminum Surfaces at Different Temperatures

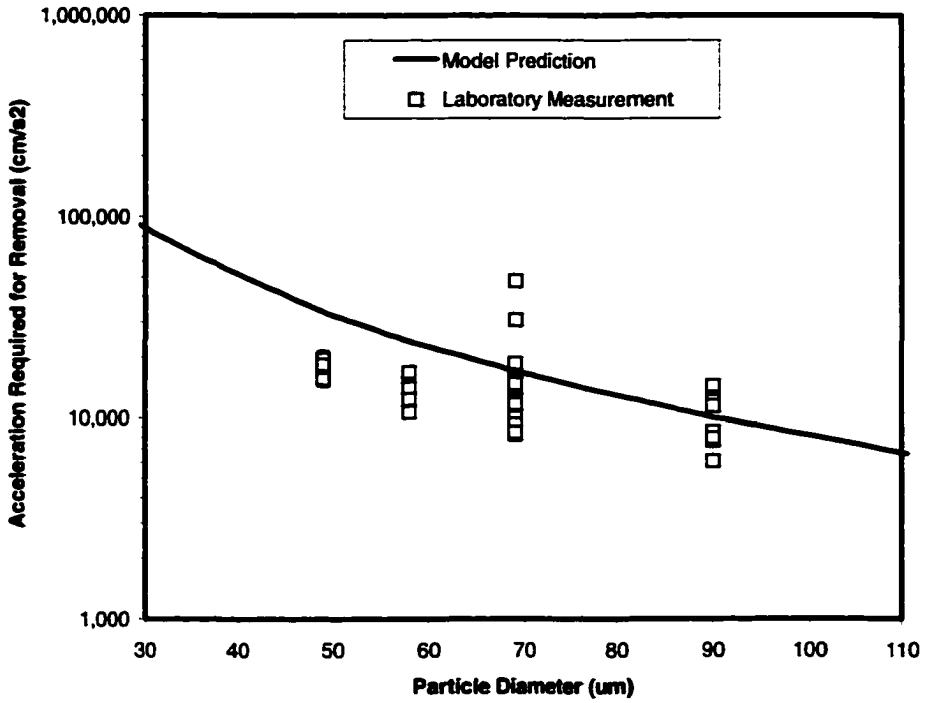

Fig. 7.11 Model Comparison for Dust with Different Diameters on Painted Surfaces

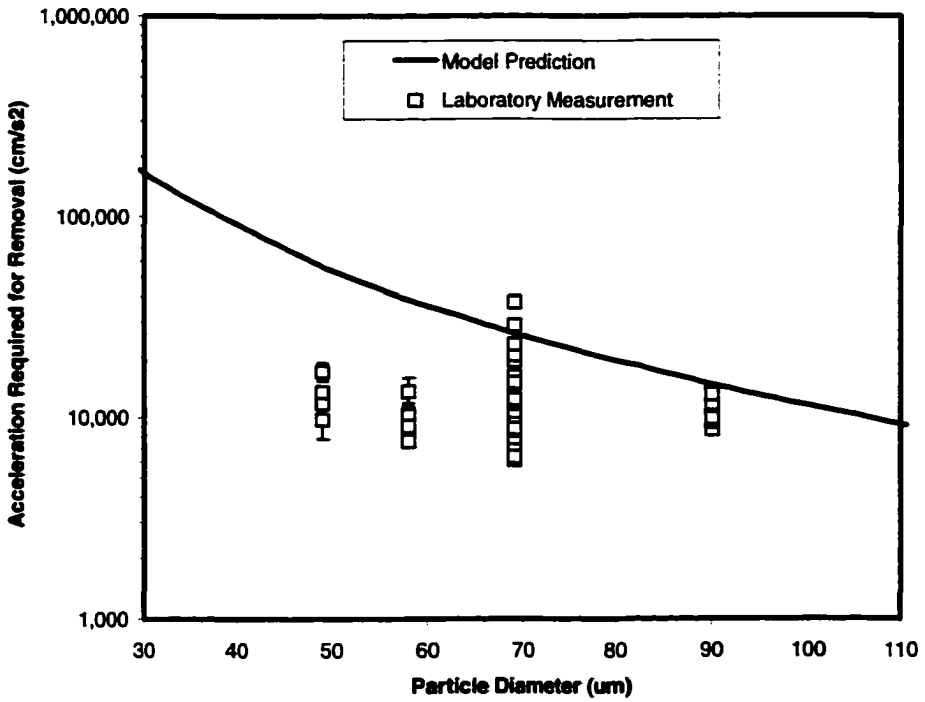

Fig. 7.12 Model Comparison for Dust with Different Diameters on Aluminum Surfaces

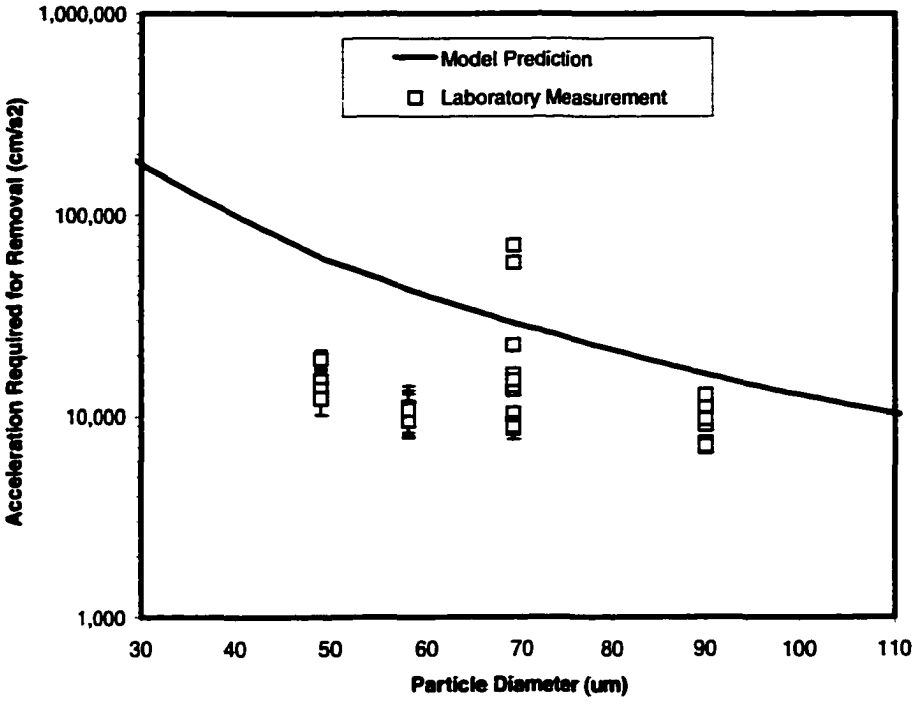

Fig. 7.13 Model Comparison for Dust with Different Diameters on Steel Surfaces

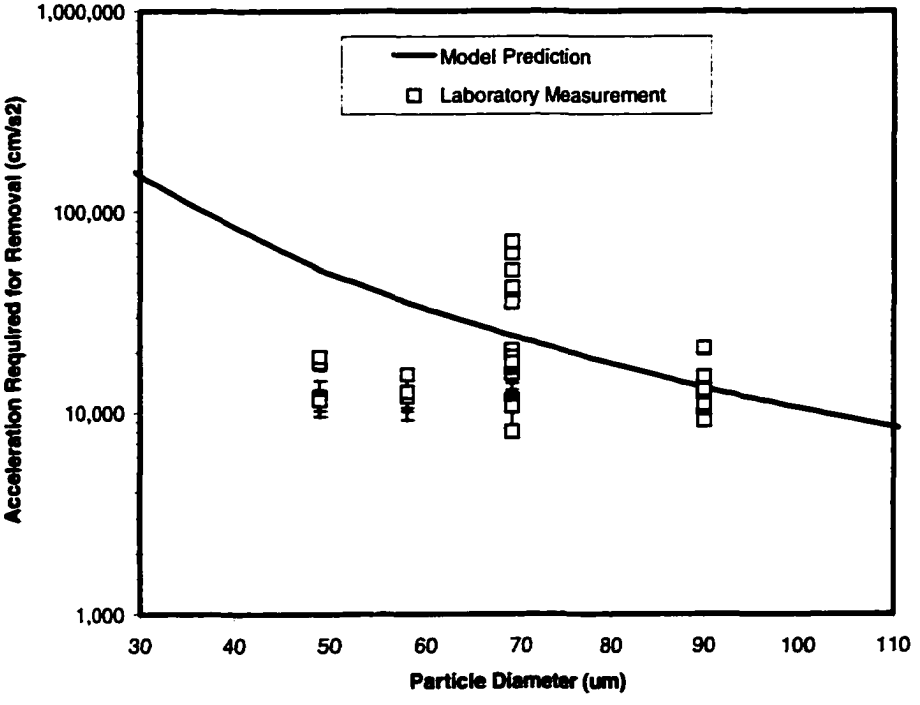

Fig. 7.14 Model Comparison for Dust with Different Diameters on Glass Surfaces

Experiments were conducted using particles of varied gradation in order to determine the effect of particle size on the acceleration required for removal. The model is compared with the results from these experiments in Figs. 7.11 through 7.14. Predicted removal acceleration matches the trend of the data for painted specimens. For all other specimens, increases in acceleration with decreasing particle size were not measured to the extent indicated by the model.

Electrostatic charge of the dust was also measured during all experiments. The measured mass density of charge ranged from -189 to 1 pC/g. The results of these experiments, shown in Fig. 7.15, indicate that electrostatic charge had no measurable effect on particle adhesion. Adhesion force calculated based on the model also indicates that electrostatic charge in the range that was measured is insignificant. Predicted adhesion based on the model is shown by the solid line in the figure.

The ability of the model to correctly predict differences in adhesion between the glass dust and the four different material specimen was verified by comparing model predictions with the results from laboratory experiments on 90 μm diameter dust at standard room temperature and at a relative humidity between 20% and 40%. Laboratory results and model predictions are shown in Fig. 7.16. The model appears to match the small differences in adhesion between the four materials except stainless steel. The predicted acceleration required for removal of glass dust from stainless steel is slightly higher than measured results. According to the model, capillary adhesion is significantly affected by material and dust particle surface Young Modulus. Since the value of the Young Modulus used in the calculations was referenced and not measured, slight differences in the Young Modulus could

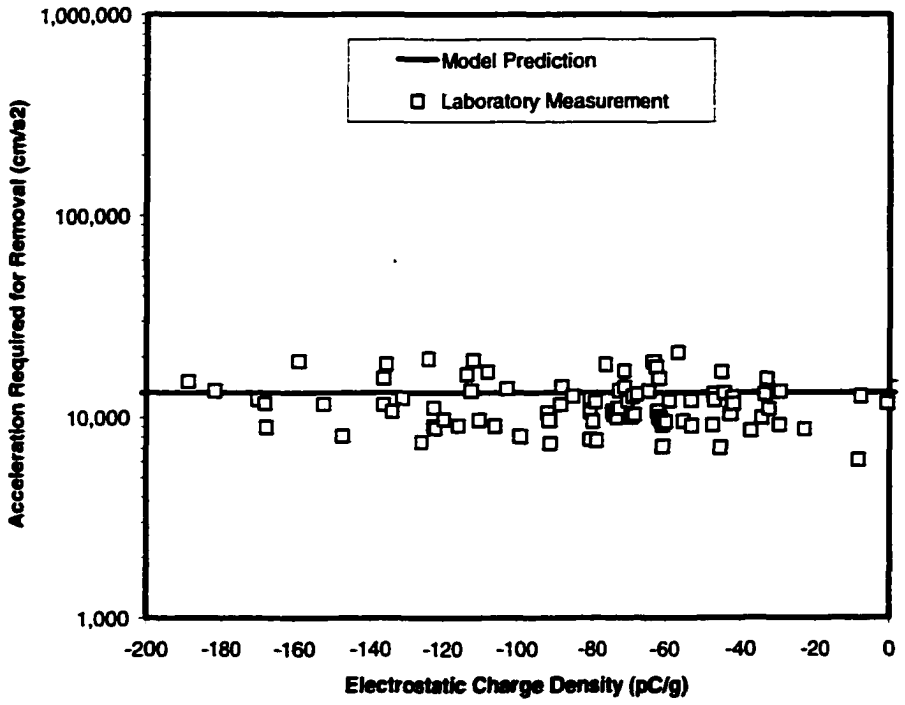

Fig. 7.15 Effect of Measured Electrostatic Charge on Adhesion

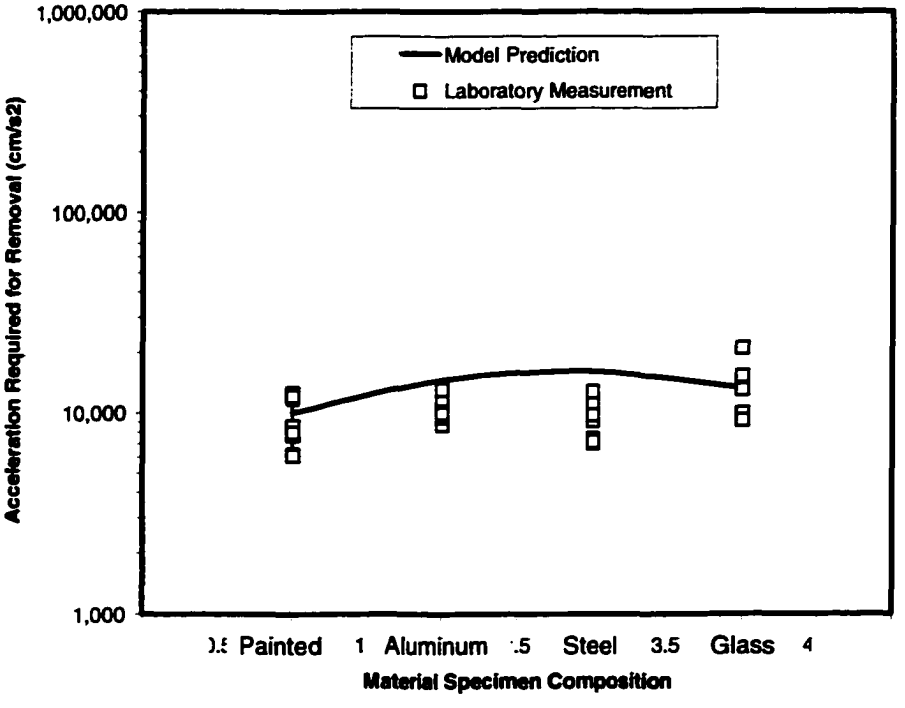

Fig. 7.16 Model Comparison for Dust on Materials of Different Composition

account for the discrepancy. Alternatively, it is noted that the steel specimens were the thinnest material used in the experiments. Consequently, secondary modes of vibration may have been more prevalent, which would cause a lower measured value of adhesion.

7.3 Model Predictions

Dust adhesion to spacecraft and equipment surfaces during planetary exploration is of considerable importance in mission design. As discussed in Chapter 2, the steady state accumulation of dust on surfaces during calm conditions on Mars causes an obscuration of solar panels and optics at a rate of 0.3% per sol (Mars day). Dust accumulation is a primary limitation on mission duration. Cometary surfaces also are anticipated to represent extremely dusty environments. Dust has been identified as a primary design parameter in the construction of a lunar base. Hence, the adhesion of planetary dusts is of paramount interest to NASA. A better understanding of adhesion may enable the development of dust mitigation strategies for future planetary surface exploration.

The model was applied to predict the adhesion of dust to surfaces under different planetary environmental conditions. The model and laboratory measurements of adhesion indicate that mineral composition has a small effect on adhesion. The chemical and physical properties of olivine were used in the model predictions for all planetary surfaces. Due to their importance in spacecraft and rover construction, glass and aluminum materials were selected as the solid surface materials that were used in the parametric analysis. Electrostatic charge on the dust particles and surfaces was assumed to be negligible. Dust particle radius was varied within the range expected for a given planetary surface. The radius of curvature

of the glass and aluminum surfaces was set equal to infinity, which is indicative of smooth flat plates. On all planetary surfaces, the presence of trace amounts of water vapor was assumed to govern adsorbed gas thickness and minor capillary radius. The strong attraction of mineral surfaces to water causes it to govern capillary adhesion, even on the Moon, which has considerably more argon than water vapor, and on Mars, which has considerably more carbon dioxide than water vapor (Perko, 1998). Saturation vapor pressures were obtained from Fig. 7.1. At low temperatures, where vapor pressure information was not available, the curves in Fig. 7.1 were linearly extrapolated. Also, at low temperatures the surface energy of water ice and Hamaker Coefficients for olivine at 270 deg K from Table 7.1 were used.

The average partial pressure of water vapor in the Martian atmosphere is 0.03% (CRC, 1997). Martian seasonal temperatures range from approximately 150 deg K to approximately 280 deg K. Atmospheric pressure on the surface of Mars is approximately 700 Pa. During the lowest temperatures of the seasonal cycle, the average composition of Mars' atmosphere, as given above, indicates that the partial pressure of water exceeds the saturation vapor pressure and frost will occur. This phenomenon was observed during the Viking missions. Under these conditions, an infinite size pendular meniscus (ice bridge) is predicted by the model. To obtain finite predictions, a practical humidity limit of 95% was assumed. Since model predictions depend on the natural logarithm of humidity, a humidity variation within the range of approximately 85% to 99% produces similar adhesion predictions.

Adhesion predicted by the model for the range of temperatures typical of the surface of Mars is shown in Fig. 7.17. Perpetually suspended dust particles in the Martian

atmosphere are expected to range in size from 0.1 to 10 μm. Hence, the model was applied for particles in this size range. The fairly flat portion of the curves on the left side of the figure is due to very high levels of relative humidity. It can be seen from the results that adhesion force is primarily dependent on particle size and is affected moderately by temperature. The role of material composition on dust adhesion is of minor importance for the two surfaces selected for this parametric study.

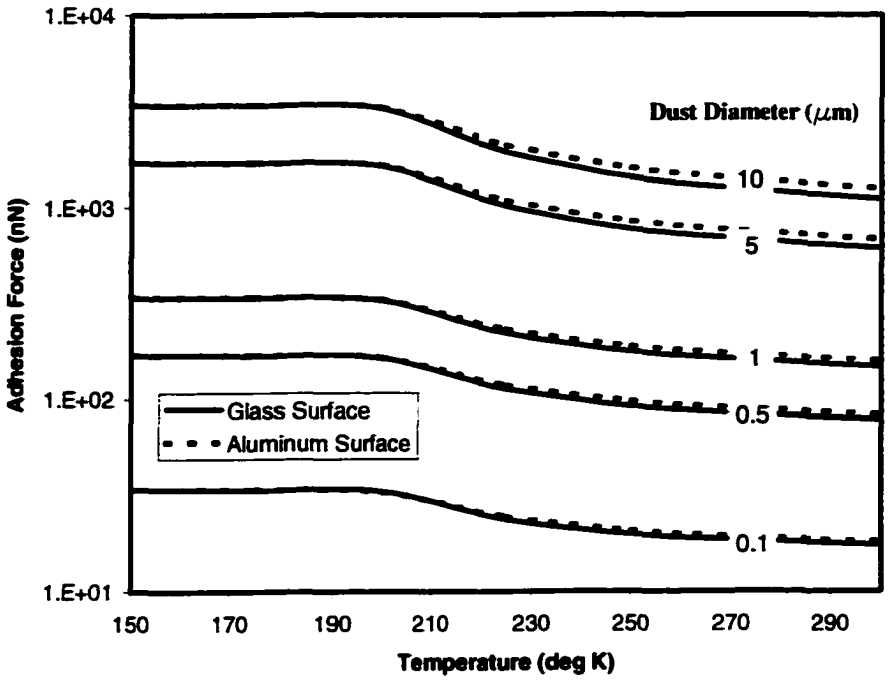

Fig. 7.17 Predicted Adhesion Force of Typical Dusts in Mars' Environmental Conditions

Perhaps more interesting than force is the acceleration required to remove dust from surfaces on Mars, which is shown in Fig. 7.18. Due to their minuscule mass, 0.1 μm diameter particles require extremely large accelerations, thereby making vibrational removal impractical. Removal of 10 μm diameter dust particles from surfaces requires 5 orders of

magnitude less vibrational acceleration than 0.1 μm particles. For comparison with Figs. 7.17 and 7.18, the model predicts that 10 μm diameter dust particles produce an adhesion force of 250 nN and require an acceleration of 1.8×10^8 cm/s^2 for removal at standard temperature, pressure, and humidity (40%) on Earth.

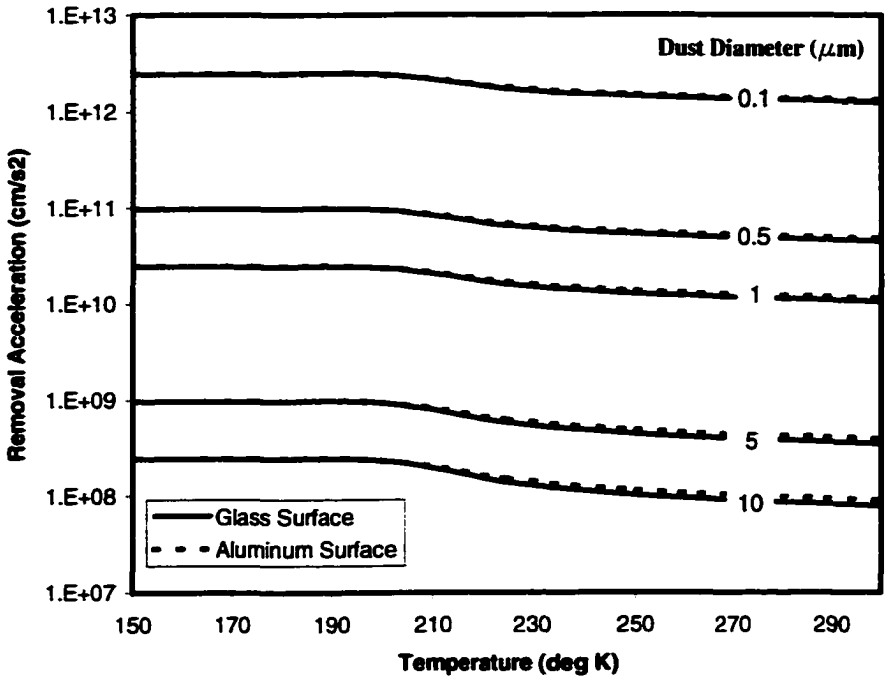

Fig. 7.18 Predicted Acceleration Required to Remove Dust from Surfaces on Mars

According to the Heiken, Vaniman, and French (1991), the partial pressure of water vapor in the thin lunar atmosphere is 0.00003% during daytime. Diurnal temperatures on the Moon range from approximately 150 deg K to approximately 400 deg K. Vacuum conditions on the Moon are on the order of 10^{-12} Pa. Due to hard vacuum, relative humidity on the Moon never exceeds 3×10^{-18} %. Soil particle gradation measured in returned near surface lunar surfaces samples mostly ranged from 5 μm to 500 μm. The average particle size was

approximately 75 μm. Hence, the model was applied to dust particles of this size range under the aforementioned lunar conditions.

Model predictions for adhesion and acceleration required for removal of dust in the lunar environment are shown in Figs. 7.19 and 7.20. The difference in adhesion force for dust on aluminum compared to glass indicates that material composition has a more important role in the adhesion of particles under vacuum conditions. This can be explained by the fact that van der Waals forces, which depend mostly on material composition, are large in very dry vacuum as compared to capillary forces, which depend mostly on the properties of water. The new model predicts an increase in adhesion at low temperatures due to the development of a monomolecular pendular ice bridge. This effect is opposite that previously predicted by Perko (1998). The latter work considered only electrostatic and van der Waals forces and failed to account for capillary force and particle deformations.

It can be seen in Fig. 7.20 that the acceleration required to remove 100 μm diameter dust from aluminum and glass is on the order of 1,000 times Earth's gravity. This acceleration is considerably less than that required to remove fine dust deposited from the Martian atmosphere. In both Figs. 7.19 and 7.20, temperature is predicted to have a small affect on the adhesion of dust on glass surfaces in vacuum.

Environmental conditions on the surface of comets is much less well known. However, it is known that comets contain a considerable amount of water ice mixed with the dust mantle. Vacuum conditions on comets were assumed to be similar to that of the lunar environment (10^{-12} Pa). Water vapor was assumed to comprise 100% of the gas present in the thin cometary atmosphere. The surface of some comets can reach temperatures as high

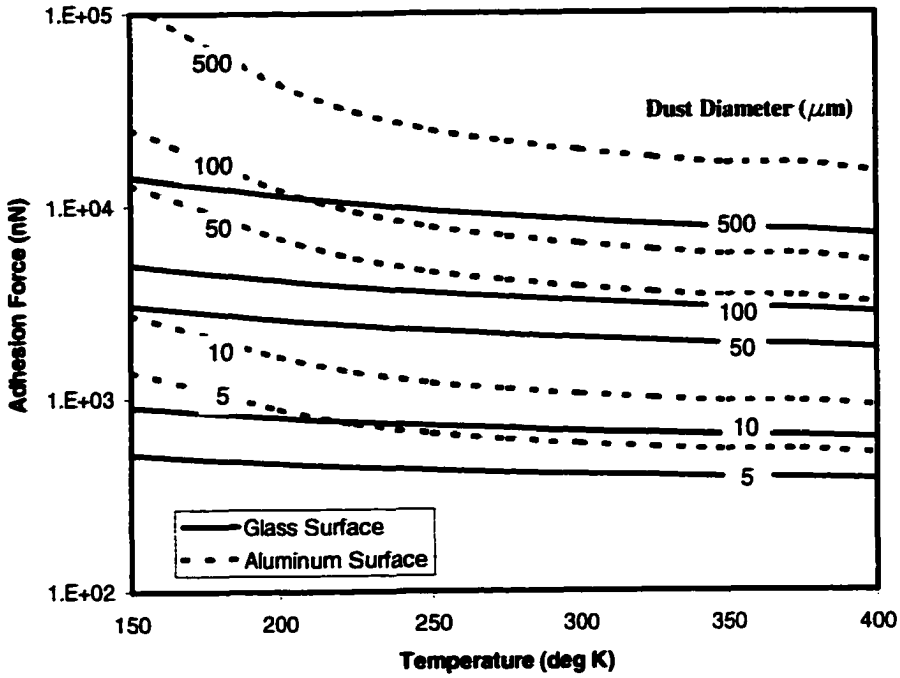

Fig. 7.19 Predicted Adhesion Force of Typical Dusts in Lunar Environmental Conditions

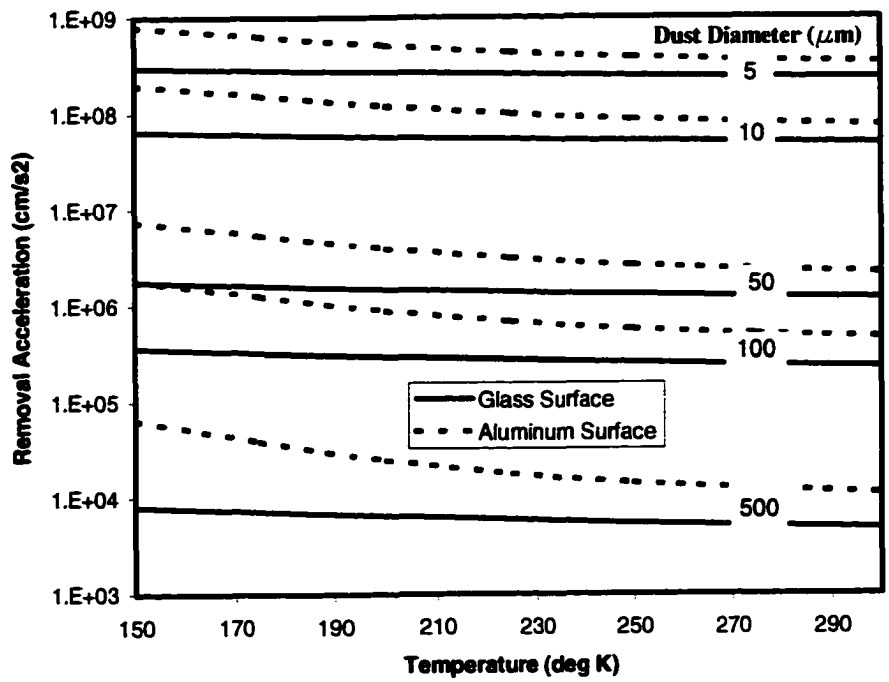

Fig. 7.20 Predicted Acceleration Required to Remove Dust from Surfaces on the Moon

as 500 deg K at perihelion. At aphelion, a temperature of 100 deg K is appropriate for the surface of many short period comets. The gradation of dust particles comprising a comet's mantle is likely between 1 μm and 10 μm.

The model was applied to predict dust adhesion force and acceleration required for dust removal on the surface of comets. Results are shown in Figs. 7.21 and 7.22. Due to the ultrahigh vacuum environment assumed for comets, the variation in dust adhesion force with temperature is small. For comparison, the adhesion force of 1 μm diameter dust at standard temperature, pressure, and humidity (40%) on Earth is approximately 30 nN and the acceleration required for removal is approximately 2.0 x 10^{10} cm/s^2. These values for Earth conditions are approximately 2 times greater than those predicted for dust of the same composition and size on the surface of comets.

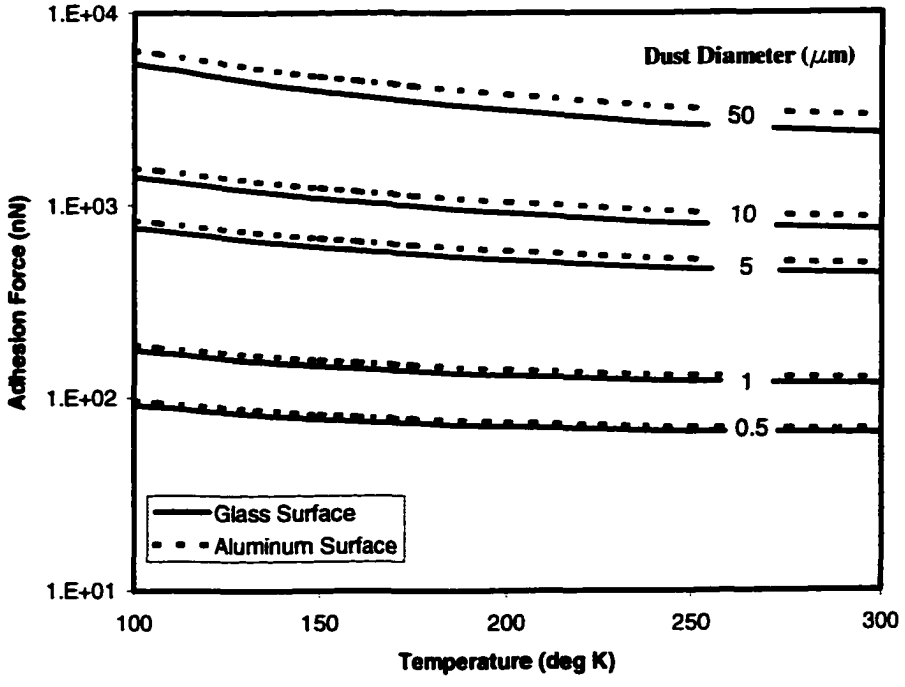

Fig. 7.21 Predicted Adhesion Force of Dust in Cometary Environmental Conditions

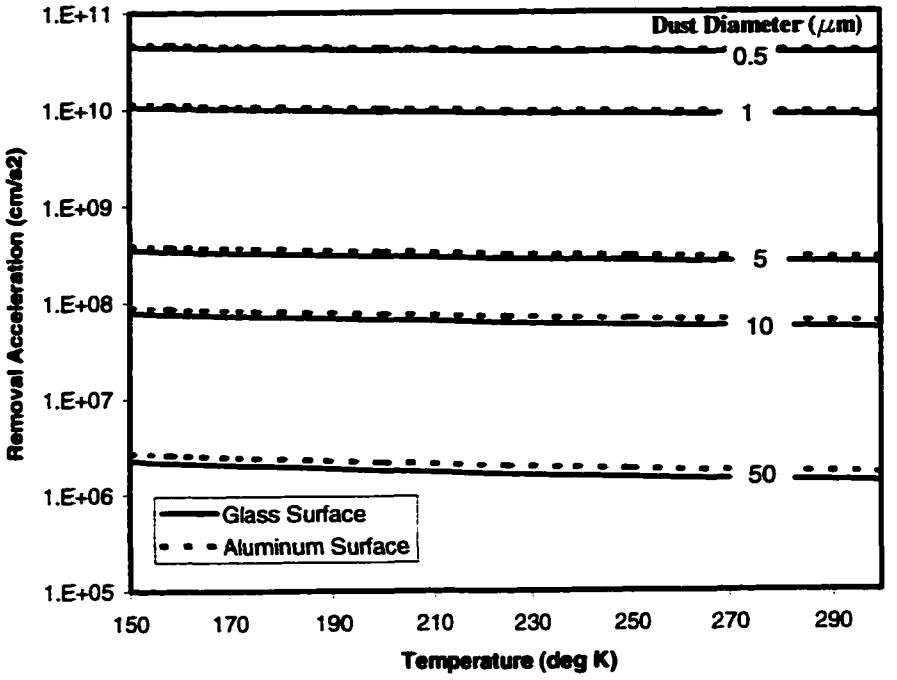

Fig. 7.22 Predicted Acceleration Required to Remove Dust from Surfaces on Comets

CHAPTER 8.0 CONCLUSIONS

In planetary exploration, dust contamination affects radiator, solar cell, optical lens, and mirror performance. During future human missions to planetary surfaces, dust may have ramifications with regard to overall cleanliness, respiratory problems, house-keeping, air-locks, biological contaminant transport, and frictional wear of machinery and equipment. Dust mechanics and adhesion research also has general applications in semiconductor, xerography, paint, air-pollution, pesticide, sand paper, tertiary oil recovery, and pharmaceutical manufacturing industries. Theoretical and laboratory investigations were conducted to gain an improved understanding of the fundamental mechanisms by which surfaces attract dust. The study was conducted in order to provide much needed criteria for development of dust mitigation techniques, that will increase the success of future planetary science exploration initiatives. Emphasis was placed on determination of the effect of environmental conditions, including temperature, pressure, and relative humidity, on dust adhesion.

The present state of knowledge regarding dust adhesion was summarized. It was identified that a theoretical effort to combine the effects of capillary, van der Waals, and electrostatic forces, as well as elastic deformation, is needed to advance the state of the art. A model for determining dust adhesion was derived which attempts to link the three major

forces of adhesion (capillary, van der Waals, and electrostatic). The model accounts for elastic particle deformation and the potential of an adsorbed gas layer separating the particles. Laboratory measurements of mineral dust adhesion were conducted using a vibrating cantilever beam apparatus under different environmental conditions. Results from the experiments, as well as prior laboratory research by others, are shown to match model predictions relatively well. The model was extended to predict dust adhesion on Mars, the Moon, and comets.

8.1 Summary of Results

1. A new method of determining adsorbate thickness and minor capillary radius between closely spaced surfaces was derived. The method accounts for combined intermolecular fields between surfaces and hence the disjoining pressure. At the limit where humidity approaches 100%, the method reduces to the well-known DLVO theory for colloidal suspensions of particles. At the limit where electrostatic energy between the surfaces is zero and humidity is high, the method reduces to the well-known Young-Laplace equation for capillary pressure.

2. It was shown that the method for predicting adsorbate thickness indicates less than a monolayer of water is present between quartz surfaces at a relative water vapor humidity below approximately 0.005%. When the layer is under a mechanical pressure equal to the hardness of quartz, a monolayer of adsorbed gas is predicted at a relative water vapor humidity below approximately 0.1%. The method was also

shown to predict that a capillary pendular ring is viable at moderate to high vacuum due to the increased adsorption potential that occurs very close to the surfaces.

3. Equations governing the shape and stresses at the contact between a particle and a curved surface or another particle were derived based on a superposition of Hertz-spherical and Boussinesq-cylindrical punch solutions. The Hertz solution was used to govern the compressive stresses and to calculate contact area. The cylindrical punch solution was used to describe the tensile surface stresses at the contact. The radius of the punch was set equal to the azimuthal radius of the liquid pendular ring between the particle contact. In this way, tensile stresses were concentrated along the perimeter of the pendular ring where van der Waals and capillary forces are highest.

4. The new model for elastic contact between two curved surfaces separated by a liquid pendular ring was shown to be capable of predicting the shape of particles at low and high humidity in accordance with interferometry observations by others.

5. An equation relating the minor and azimuthal radii of a pendular ring between deformed surfaces separated by a layer of adsorbed gas was derived for the case where liquid-solid contact angles are small. The new equation reduces to that derived by others for the case where adsorbate thickness and particle deformation are set equal to zero.

6. An alternate behavior of capillary pendular rings was presented. It was shown that this new behavior is predominant when the deformation of the particles is less than the adsorbate thickness separating them. Capillary force was derived based on the new behavior. At high humidity, the new expression for capillary force was shown to be equivalent to conventional capillary theory.

7. A model for dust adhesion was derived by combining capillary, van der Waals, and electrostatic energies. Deformation of the particle and the surface were taken into account. The limits of the model were shown to match the DMT theory at low humidity and conventional capillary theory at high humidity. At intermediate levels of humidity, the model was shown to correlate well with laboratory measurements obtained by Fisher and Israelachvili (1981).

8. A total of 248 laboratory measurements of dust adhesion were obtained using glass microspheres and olivine dust. The experiments consisted of depositing the dust on aluminum, stainless steel, painted aluminum, and glass material specimens under different environmental conditions, that included high humidity, vacuum, and cold temperatures. The material specimen were vibrated, and the force required to remove the dust was inferred from frequency and amplitude.

9. The adhesion of glass microspheres to glass and stainless steel material specimens increased with time, whereas, adhesion was not a function of dust residence time on

aluminum and painted aluminum specimens. Residence time was varied from 1 to 300 minutes in the experiments.

10. Laboratory experiments confirmed the results of Mizes, et al. (2000), which showed that the number of neighboring particles had no measurable effect on individual dust particle adhesion. Experiments were conducted using less than 50% of the mass of dust required to form a complete closely packed monolayer.

11. Electrostatic charge of the dust was measured during deposition on the material specimens. In all experiments, the electrostatic charge was small and had no measurable effect on adhesion.

12. Olivine particles were both positively and negatively charged, and their net charge varied considerably more than that of the glass particles. Glass particles almost always carried a net negative charge, which was strongly correlated with dust diameter. The average electrostatic charge carried by 45 μm diameter glass spheres was approximately 3 times greater than that of 69 μm diameter glass spheres and 4 times greater than that of 90 μm diameter glass spheres.

13. Measured adhesion of glass dust on aluminum, stainless steel, and glass increased with humidity. The adhesion of glass dust on glass surfaces exhibited the largest effect. The adhesion of glass dust on painted aluminum was insignificantly affected by

humidity.

14. Temperature had a small effect on the adhesion of glass dust to glass surfaces. However, the adhesion of glass dust to the other materials was less at 273 deg K than that at standard room temperature. Below 273 deg K, adhesion of glass dust to the other materials increased. The coldest environments in which experiments were conducted in air was 260 deg K and in vacuum was 150 deg K.

15. In general, measured adhesion force increased inversely with dust particle diameter. This effect was most pronounced for glass dust on painted aluminum surfaces, where the average adhesion of 45 μm spheres at standard temperature, pressure, and humidity was approximately 2 times greater than the average adhesion of 90 μ diameter glass spheres.

16. The difference in measured adhesion for dust on the four material specimens at standard temperature, pressure, and humidity was small. Average adhesion of glass dust to glass and painted specimens was approximately 1.2 times greater than the average adhesion of glass dust to stainless steel and aluminum specimens.

17. In the limited number of experiments conducted in vacuum, the adhesion of glass dust to stainless steel was greater in high vacuum than at standard pressure. Adhesion of glass dust to painted aluminum and the adhesion of olivine dust to all four materials

was less in high vacuum than at standard pressure. During the experiments, vacuum levels were approximately 10^{-6} Torr, and outgassing was conducted for approximately 48 hours prior to deposition of the dust on the material specimen.

18. One experiment was conducted with glass spheres in high vacuum at a temperature of 44.5 deg C. An experiment was not conducted at the same temperature in air. The adhesion exhibited by the glass spheres was less in high vacuum at high temperature than that in-air at standard temperature and humidity for all material specimen except glass, which had approximately the same adhesion in both environments.

19. In all of the vacuum experiments, the concentration of water vapor was always on the order of 100 to 1000 times greater than other background gases within the chamber even after several days of outgassing.

20. A theoretical analysis was performed to evaluate the effectiveness of using dry nitrogen at 1 atm to simulate vacuum conditions. The model predicts that at a relative water vapor humidity less than 0.6%, the preferential adsorption of nitrogen begins and potential van der Waals forces that would manifest in vacuum may be shielded by adsorbed nitrogen.

21. The model compares well with laboratory results obtained for aluminum, painted, and glass surfaces at different levels of humidity. Model predictions of the adhesion of

glass dust to stainless steel compare less well. The model indicates that the primary difference between the trend of adhesion measurements for painted surfaces and the trend for aluminum and glass surfaces is due to differences in the Modulus of Elasticity of those surfaces.

22. Although provisions that account for transformation of the capillary pendular ring to solid phase were not incorporated in the model, theoretical predictions match the general trend and magnitude of laboratory adhesion force measurements conducted over the temperature range from 20 deg C to -30 deg C for all materials.

23. The model correctly predicts an increase in adhesion with a decrease in dust particle diameter, as was measured in the laboratory experiments. However, the model appears to overestimate the adhesive strength of smaller particles on all surfaces. The discrepancy was less for dust on aluminum surfaces.

24. The model indicates that the electrostatic charge of the dust deposited on the material surfaces was insufficient to cause measurable changes in adhesion. This is consistent with laboratory results.

25. The model indicates that only small differences in the adhesion force of dust is due to the composition of the material surfaces used in the experiments. This is also consistent with laboratory results.

26. The model was applied to predict the adhesion of dust in different planetary environments. In the application, the dust was assumed to be electrostatically neutral. Results indicate that the adhesion force of dust is generally smaller on the Moon, Mars, and comets than in humid environments on Earth. However, the predicted adhesion force on these planetary bodies is higher than in dry environments on Earth.

27. The model predicts that adhesion generally increases with decreasing temperature on planetary surfaces. Material composition appears to have a greater role in governing adhesion in the lunar environment. This prediction was explained by the fact that van der Waals forces, which depend on material composition, are much greater on the Moon than capillary forces, which depend mostly on the properties of liquid water.

8.2 Recommendations for Additional Study

During one of the first vacuum experiments, the material specimens were contaminated with enamel from the outgassing of nearby magnet wires. This coating appeared to significantly reduce adhesion of dust to glass and aluminum. It had no apparent affect on adhesion of dust to painted aluminum and caused a slight increase in adhesion to stainless steel. The outgassing wires were replaced with teflon coated wires in later experiments. Previous work in the pharmaceutical industry has shown that surface coatings which increase material hardness can considerably decrease dust adhesion. Investigation into the effect of enamel and general research in the application of surface coatings for dust mitigation are important areas of future research that should be undertaken.

Results and predictions of the model, which is based on a liquid pendular ring around the contact between particles and surfaces, compare well with laboratory measurements at cold temperatures. Much more experimental data are needed to adequately describe the behavior of dust and to further verify the performance of the model in cold environments. The effect of a change in the pendular ring to solid phase needs to be theoretically evaluated to determine if it is appropriate to model an ice bridge using the same procedures as a liquid capillary.

In the derivation of the model, a few numerical substitutions and approximations were necessary to find a closed-form solution. Errors introduced by these simplifications need to be further evaluated from a theoretical and experimental standpoint. The model provides poor predictions of final contact area, which tends toward zero under all conditions. Several interferometry studies, Fisher and Israelachvili (1981a and 1981b) and Christensen (1996), showed that final contact area does tend toward zero in humid environments. However, it has been shown theoretically in the JKR model and experimentally verified in numerous studies that the final contact area is approximately 0.7 times the initial contact area in dry environments. Additional theoretical work is necessary to try and modify the model and to better predict final contact area.

REFERENCES

Adamson, A.W. (1990) *Physical Chemistry of Surfaces*, 5th Edition, Wiley Interscience, New York.

Ando, Y. and Ino, J. (1998) "Friction and Pull-Off Forces on Submicron-Size Asperities" Wear, 216, pp. 115-122

Appelbaum, J., Landis, G.A., and Sherman, I. (1993) "Solar Radiation on Mars - Update 1991" Solar Energy, Vol. 50, pp. 35-51

Balbanov, E.M. (1954) "Dispersed Systems in the Electric Field of a Corona Discharge" Doctoral Dissertation, P.N. Lebedev Physics Institute

Banin, A. (1989) "The Mineral Components of Dust on Mars" LPI Technical Report No. 89-01, MECA Workshop on Dust on Mars III, Houston, TX, pp. 15-17

Bar-Nun, A., et. al. (1989). "Experimental Studies of Gas Trapping in Amorphous Ice and Thermal Modeling of Comets - Implications for Rosetta". LPI Workshop, Analysis of Returned Comet Nucleus Samples, Milpitas, CA

Barenblatt, G.I. (1962) Adv. Apl. Mech, No. 7, pp. 55

Bell, III, J.F., et al. (2000) "Mineralogic and Compositional Properties of Martian Soil and Dust: Results from Mars Pathfinder" Journal of Geophysical Research, Vol. 105, No. E1, pp. 1721-1755.

Berbner, S. and Loffler, F. (1994) "Influence of High Temperatures on Particle Adhesion" Powder Technology, Vol. 78, pp. 273-280

Blum, J. (2000) "Laboratory Experiments on Preplanetary Dust Aggregation" Space Science Reviews, 192, pp. 265-278.

Boussinesq, J. (1885) *Application des Potentiels a l'Etude de l'Equilibre et du Mouvement des Solides Elastiques*, Gauthier-Villars, Paris

Bowden, F.P., and Tabor, D. (1954) *The Friction and Lubrication of Solids*, Oxford Univ. Press, London

REFERENCES

Bowen, R.C., et al. (1991) J. Appl. Phys., No. 70, p. 3360

Braaten, D.A. (1994) "Wind-Tunnel Experiments of Large Particle Reentrainment-Deposition and Development of Large Particle Scaling Parameters" Aerosol Science and Technology, 21, (2), pp. 157-169

Buehler, M.G., et al. (2000) "From Concept to Flight Delivery in Eighteen Months: The MECA/Electrometer Case Study" Proceedings of the 2000 IEEE Aerospace Conference.

Busnaina, A.A. (1995) "Particle-Substrate Collisions, Particle Rebound and Removal" Journal of Adhesion, Vol. 51, pp. 167-180

Chaudhury, M.K. and Whitesides, G.M. (1996) "Correlation Between Surface Free Energy and Surface Constitution" Science, Vol. 255, p. 1230

Christensen, H.K. (1987) "Adhesion between Surfaces in Undersaturated Vapors-A Reexamination of the Influence of Meniscus Curvature and Surface Forces" Pull Off Force Between Surfaces, Academic Press Inc.

Christenson, H.K. (1985) Journal of Colloid Interface Science, No. 105, pp. 234-249

Christenson, H.K. (1996) "Surface Deformations in Direct Force Measurements" Langmuir, 12, pp. 1404-1405.

Clancy, R.T. and Lee, S.W. (1991) "A New Look at Dust and Couds in the Mars Atmosphere" Icarus, Vol. 93, pp. 135-158

Clark, B.C., et al. (1982) "Chemical Composition of Martian Fines" Journal of Geophysical Research, No. 87, pp. 10,059-10,067

Cooper, D.W., Wolfe, H.L., and Miller, R.J. (1988) "Electrostatic Removal of Particles from Surfaces" Particles on Surfaces 1, Detection, Adhesion, and Removal, K.L. Mittal, Ed., Plenum Press, New York

Chemical Rubber Company (1997) *Handbook of Chemistry and Physics,* 77th Edition, CRC Press

REFERENCES

Delsemme (1988) "The Chemistry of Comets" Phil. Trans. Roy. Soc. London A, No. 325, pp. 509-523

Derjaguin, B.V. (1934) Knoll. Z., No. 69, p. 155

Derjaguin, B.V. and Landau (1941) Acta Physicochim. URSS, No. 14, pp. 633-662

Derjaguin, B.V. (1961) "Influence of Liquid Films on Adhesion Between Particles and Powders" Symposium on Powders in Industry, Society of Chemical Industry, London

Derjaguin, B.V., Muller, V.M., and Toporov, Y.P. (1975) "Effect of Contact Deformations on the Adhesion of Particles" Journal of Colloid Interface Science, Vol. 53, No. 2, p. 314.

DeVore, G. W. (1963) "Compositions of Silicate Surfaces and Surface Phenomena" Contrib. Geol. 2, pp. 21-37

Domink, C. and Tielens, A.G.G.M. (1997) "The Physics of Dust Coagulation and the Structure of Dust Aggregates in Space" The Astrophysical Journal, 480, pp. 647-673.

Duncan, et al. (1988) "The Origin of Short Period Comets" Astrophys. J., No. 328, pp. L69-L73

Evans, S. (1965) "Dielectric Properties of Ice and Snow-A Review" J. of Glaciology, p. 773

Feng, J.Q. (2000) "Contact Behavior of Spherical Elastic Particles: A Comutational Study of Particle Adhesion and Deformations" Colloids and Surfaces A-Physicochemical and Engineering Aspects, 172, pp. 175-198.

Feng, J.Q. and Hays, D.A. (2000) "Therory of Electric Field Detachment of Charged Tonner Particles in Electrophotography" Journal of Imaging Science and Technology, Vol. 44, No. 1, pp. 19-25.

Ferguson, D.C., et al. (1999) "Evidence for Martian Electrostatic Charging and Abrasive Wheel Wear from the Wheel Abrasion Experiment on the Pathfinder Sojourner Rover" Journal of Geophysical Research, No. 104, Vol. E4, pp. 8747-8759.

REFERENCES

Fischer-Cripps, A.C. (2000) *Introduction to Contact Mechanics*, Springer, New York.

Fisher, L.R. and Israelachvili, J.N. (1981a) "Experimental Studies on the Applicability of the Kelvin Equation to Highly Curved Concave Menisci" J. Colloid Int. Sci., Vol. 80, No. 2, p. 528

Fisher, L.R. and Israelachvili, J.N. (1981b) "Direct Measurement of the Effect of Meniscus Forces on Adhesion: A Study of the Applicability of Macroscopic Thermodynamics to Microscopic Liquid Interfaces" Colloids and Surfaces, Vol. 3, pp. 303-319

Fishbane, P.M., Gasiorowicz, S., and Thornton, S.T. (1993) *Physics for Scientists and Engineers*, Prentice-Hall, Inc., New Jersey

Fogden and White (1990) "Contact Elasticity in the Presence of Capillary Condensation" J. Colloid Int. Sci., Vol. 138, No. 2, p. 414

Fowlkes, W.Y. and Robinson, K.S. (1988) "The Electrostatic Force on a Dielectric Sphere Resting on a Conducting Substrate" Particles on Surfaces 1, Detection, Adhesion, and Removal. K.L. Mittal, Ed., Plenum Press, New York

Fuller, K.N.G. and Tabor, D. (1975) "The Effect of Surface Roughness on The Adhesion of Elastic Solids" Proceedings of the Royal Society of London A, Vol. 345, p. 327

Gaier, J. R., Perez-Davis, M. E., Marabito, M. (1990) "Aeolian Removal of Dust From Photovoltaic Surfaces on Mars" NASA Technical Memorandum 102507

Gane, N., Pfaelzer, P.F., and Tabor, D. (1974) Proc. Roy. Soc. Ser. A, 340, p. 495

Gierasch, P.J., and Goody, R.M. (1973) "A Model of a Martian Great Dust Storm" Journal of Atmospheric Science, 30, pp. 169-179

Glazanov, V.N. (1950) "On The Electrostatic Enrichment of Coal Fragments" Ugletekhizdat

Gombosi, T. I., Nagy, A. F., Cravens, T. E. (1986) "Dust and Neutral Gas Modeling of the Inner Atmospheres of Comets." Reviews of Geophysics, Vol. 24, No. 3, pp. 667-700

REFERENCES

Good, R.J. (1993) "Contact Angle, Wetting, and Adhesion: A Critical Review" *Contact Angle, Wettability, and Adhesion*, K.L. Mittal, Ed., VSP, The Netherlands

Gooding, J.L. (1991) "Chemistry and Mineralogy of Martian Dust: An Explorers Primer" Sand and Dust on Mars, NASA Conference Publication CP-10074, pp. 21-22.

Green, J.R. (1999a) "Deep Space 4 / Champollion Extraterrestrial Materials Simulation Laboratory Fiscal Year 1999 Activities". JPL Internal Document, Pasadena, CA

Green, J.R. (1999b) Personal Communication

Greenberg, J.M., Mizutani, H. and Yamamoto, T. (1995). "A New Derivation of the Tensile Strength of Cometary Nuclei: Application to Comet Shoemaker - Levy 9". Astronomy and Astrophysics, pp. L35-L38

Greenberg, J. M. (1989) "Interstellar Dust as the Source of Organic Molecules in Comet Halley" Adv. Space Research, Vol 9, No. 2, pp. (2)13-(2)22

Griffiths, D.J. (1999) *Introduction to Electrodynamics*, Prentice-Hall, Inc., New Jersey

Griffith, A.A. (1920) Philos. Trans. R. Soc. London A, Vol. 221, p. 163

Grun, E., et al. (1989). "Mechanisms of Dust Emission from the Surface of a Cometary Nucleus" Adv. Space Research, Vol. 9, No. 3, pp. (3)133-(3) 137

Grun, E., et al. (1991) "Laboratory Simulation of Cometary Processes: Results from First KOSI Experiments" Comets in the Post-Halley Era. Vol. 1, Newburn R.L., Jr., eds., pp. 277-297

Grun, E. (1991) "Modifications of Comet Materials by the Sublimation Process: Results from Simulation Experiments" Workshop on the Analysis of Returned Comet Samples, LPI, Milpitas, CA

Hardy, W. B. (1936) *Collected Works*, Cambridge University Press, Cambridge, England

REFERENCES

Hartmann, W.K. (1989) "Comments on Comet Shapes and Aggregation Processes". LPI Workshop, Analysis of Returned Comet Nucleus Samples, Milpitas, CA

Havnes, O. (1984) "Charges on Dust Particles" Adv. Space Res. Vol. 4, No. 9, pp. 75-83

Hehn, A.H., Kimzey, J.H. (1968) "Adhesion of Metals and Nonmetals in Ultrahigh Vacuum" Lubrication Engineering, Vol. 24, p. 274-285

Heiken, G.H., Vaniman, D.T., and French, B.M. (1991) *Lunar Sourcebook: A User's Guide to the Moon*, Cambridge Unviersity Press, New York.

Henniker, J. (1962) Nature, No. 196, p. 474

Hertz, H. (1881) "On the Contact of Elastic Solids", J. Reine Angew. Math., No. 92, pp. 156-171

Hill, L. R., and Cakmak, A. S. (1965) "The Effect of Vacuum on the Shear Strength of an Idealized Granular Medium" Astronautica Acta, Vol. 11, pp. 261-267 [AIAA #A66-28180]

Hoenig, S.A. (1988) "Fine Particles on Semiconductor Surfaces: Sources, Removal, and Impact on the Semiconductor Industry" Particles on Surfaces 1, Detection, Adhesion, and Removal, K.L. Mittal, Ed., Plenum Press, New York

Horn, R.G., Israelachvili, J.N., and Pribac, F. (1987) "Measurement of the Deformation and Adhesion of Solids in Contact" Journal of Colloid Interface Science, Vol. 115, No. 2, p. 480.

Huebner, W.F., and Boice, D.C. (1989) "Morphology and Compositional Differentiation of the Surface of Comets". LPI Workshop, Analysis of Returned Comet Nucleus Samples, Milpitas, CA

Huebner, W.F., Ed. (1990) *Physics and Chemistry of Comets*, Springer-Verlag, Berlin.

Israelachvili, J. (1992) *Intermolecular & Surface Forces*, 2nd Edition, Academic Press, London.

REFERENCES

Israelachvili, J.N. and Ninham, B.W. (1977) "Intermolecular Forces-The Long and Short of It" Journal of Colloid and Interface Science, Vol. 58, No. 1, p. 14.

Jackson, J.D. (1975) *Classical Electrodynamics*, 2nd Edition, John Wiley & Sons, New York

Johnson, K.L. (1958) "A Note on the Adhesion of Elastic Solids" British Journal of Applied Physics, Vol. 9, pp. 199-200

Johnson, K.L. (1971) "Surface Energy and the Contact of Elastic Solids" Proceedings of the Royal Society of London A, Vol. 324, pp. 301-313

Johnson, K.L. (1985) *Contact Mechanics*, Cambridge University Press, Cambridge

Johnson, K.L., Kendel, K., and Roberts, A.D. (1971) "Surface Energy and the Contact of Elastic Solids" Proc. R. Soc. Lond. A, No. 324, pp. 301-313

Johnson, R. W., and Greiner, J. M. (1965) "Chemical Bonding and Shear Strength of Silicate Systems under Lunar Conditions" 4th Annual Meeting, Working Group on Extraterrestrial Resources, Colorado Springs, CO

Johnson, S.W., Chua, K.M., and Burns, J.O. (1995) "Lunar Dust, Lunar Observatories, and Other Operations on the Moon" Journal of The British Interplanetary Society, Vol. 48, pp. 87-92.

Khilnani, A. (1988) "Cleaning Semiconductor Surfaces: Facts and Foibles" Particles on Surfaces 1, Detection, Adhesion, and Removal, K.L. Mittal, Ed., Plenum Press, New York

Klinger, J. (1982). "Modeling of Cometary Nuclei". INAC ATP Planetologie, Grant No. 4731, Saint Martin d'Heres Cedex, France

Kochan H., et al. (1989a) "Laboratory Simulation of a Comet Nucleus Experimental Setup and First Results", LPI Conference, 19th Lunar and Planetary Science Conference, Houston, Texas, pp. 487-492

Kochan, H., et al. (1990) "Particle Emission from Artificial Cometary Surfaces: Material Science Aspects" LPI Conference, 20th Lunar and Planetary Science Conference Proceedings, pp. 401-144

REFERENCES

Kochan, H., et al. (1989b) "Comet Simulation Experiments in the DFVLR Space Simulators." Adv. Space Res., Vol. 9. No. 3. pp. (3)113-(3)122

Kordecki, M.C. and Orr, C. (1960) "Adhesion of Solid Particles to Solid Surfaces" AMA Archives of Environmental Health, Vol. 1, pp. 13-21

Krishnan, S., Busnaina, A.A., Rimai, D.S., and Demejo, L.P. (1994) "The Adhesion-Induced Deformation and The Removal of Submicrometer Particles" Journal of Adhesion Science and Technology, Vol. 8, No. 11, pp. 1357-1370

Lammerzahl, P. (1995) "Ice/Dust Mixtures in Simulated Space Environment: A Study of Sublimation and of Related Phenomena" Adv. Space Res., Vol 15, No. 10, pp. (10)19-(10)28

Landis, G.A. (1996) "Dust Obscuration of Mars Solar Arrays" Acta Astronautica, Vol. 38, No. 11, pp. 885-891.

Landis, G.A. and Jenkins, P.P. (1997) "Dust on Mars: Materials Adherance Experiment Results from Mars Pathfinder" Proceedings of the 26th IEEE Photovoltaic Specialists Conference, Anaheim, CA, pp. 865-869

Landis, G.A., et al. (1996) "Development of a Mars Dust Characterization Instrument" Planetary and Space Science, Vol. 44, No. 11, pp. 1425-1433.

Larsen, R.I. (1958) "The Adhesion and Removal of Particles Attached to Air Filter Surfaces" Industrial Hygiene Journal, 19, p. 265-270

Leach, R.N. (1991) "Saltation Threashold Reduction due to the Electrostatic Agglomeration of Fine Particles" Sand and Dust on Mars, NASA Conference Publication CP-10074, p. 38

Levin, B.Y. (1943) "Gas Evolution from the Nucleus of a Comet as Related to the Variations in its Absolute Brightness" Compt. Rend. Acad. Sci. URSS, No. 38, pp. 72-74

Li, T.X., et al. (1999) "Dry Triboelectric Separation of Mineral Particles: A Potential Application in Space Exploration" Journal of Electrostatics, No. 47, pp. 133-142

Lifshitz, E.M. (1956) Soviet Physics, JETP (English Translation), No. 2, pp. 73-83

REFERENCES

Lorenz, R.D. (1998) "Preliminary Measurements of the Cryogenic Dielectric Properties of Water-Ammonia Ices: Implications for Radar Observations of Icy Satellites". Icarus, Vol. 136, Article No. IS986017, pp. 344-348

Lyttleton, R.A. (1953) *The Comets and Their Origin*, Cambridge University Press, London

Madsen, M. B., et al. (1999) "The Magnetic Properties Experiments on Mars Pathfinder" Journal of Geophysical Research, Niels Bohr Institute for Astronomy, Copenhagen, Denmark, Vol. 104, No. E4, pp. 8761-8779.

Maugis, D. (1992) "Adhesion of Spheres: The JKR-DMT Transition Using a Dugdale Model" Journal of Colloid and Interface Science, Vol. 150, No. 1, pp. 243-269.

Maugis and Pullock (1995?) see chapter 3, pg. 30and 31

Metzger, S.M., et al. (1999) "Dust Devil Vortices Seen by the Mars Pathfinder Camera." Geophys. Res. Letters

Mitchell, J.K. (1993) *Fundamentals of Soil Behavior*, John Wiley & Sons, Inc., New York

Mizes, H., et al. (2000) "Small Particle Adhesion: Measurement and Control" Colloids and Surfaces A-Physicochemical and Engineering Aspects, 165, pp. 11-23.

Mizes, H.A. (1995) "Surface Roughness and Particle Adhesion" Journal of Adhesion, Vol. 51, pp. 155-165.

Moeller, C.E. and Noland, M.C. (1967) "Cold Welding Tendencies and Frictional Studies of Clean Metals in Ultra-High Vacuum" ASLE Transactions, Vol. 10, No. 2, pp. 146-157

Muller, V.M., Yushchenko, V.S., and Derjarguin, B.V. (1983) "General Theoretical Consideration of the Influence of Surface Forces on Contact Deformations and the Reciprocal Adhesion of Elastic Spherical Particles" J. Col. Int. Sci., 92, pp. 92-101.

Mullins, M.E., et al. (1992) "Effect of Geometry on Particle Adhesion" Aerosol Science and Technology, Vol. 17, No. 2, pp. 105-118.

REFERENCES

Oort, J.H. (1950) "The Structure of the Cloud of Comets Surrounding the Solar System, and a Hypothesis Concerning Its Origin" Bull. Astron. Inst. Neth., No. 11, pp. 91-110

Opik, E. (1966) "The Stray Bodies in the Solar System II: The Cometary Origin of Meteorites" Adv. Astron. Astrophys., No. 4, pp. 302-336

Orr, F.M., Scriven, L.E. and Rivas, A.P. (1975) "Pendular Rings Between Solids: Meniscus Properties and Capillary Force", Journal of Fluid Mech., No. 67, pp. 723-742

Perko, H.A. (1998) "Surface Cleanliness Based Dust Adhesion Model", Proceedings of th 6th International Conference and Exposition on Engineering, Construction, and Operations in Space, ASCE Press, Richmond, VA, pp. 495-505.

Perko, H.A. (1996) "Surface Cleanliness Effect on Lunar Soil Shear Strength" Masters Thesis, Colorado State University, Fort Collins, Colorado

Perko, H.A., Nelson, J.D., and Sadeh, W.Z. (1996). "Surface Cleanliness Effect on Lunar Soil Mechanics", Proc. of the 4th Int. Conf. on Construction, Operations and Sciences in Space, Albuquerque, NM, ASCE Press, Reston, VA, pp. 689-698.

Perko, H.A., Nelson, J.D., and Sadeh, W.Z. (2001) "Surface Cleanliness Effect on Lunar Soil Shear Strength" April 2001, Journal of Geotechnical and Geoenvironmental Engineering, ASCE Press, Reston, VA

Phares, D.J., Smedley, G.T., and Flagan, R.C. (2000) "Effect of Particle Size and Material Properties on Aerodynamic Resuspension from Surfaces" Journal of Aerosol Science, Vol. 31, No. 11, pp. 1335-1353.

Pitman, K.M., et al. (2000) "On The Shape of Martian Dust and Water Ice Aerosols" Loose-Leaf Handout, Poster Session, 32nd Meeting of the Division of Planetary Scientists, American Astronomical Society, Pasadena, CA

Podczeck, F. (1999) "Investigations into the Reduction of Powder Adhesion to Stainless Steel Surfaces by Surface Modification to Aid Capsule Filling" International Journal of Pharmaceutics, 178, (1), pp. 93-100.

Podczeck, F., Newton, J.M., and James, M.B. (1997) "Influence of Relative Humidity of Storage Air on the Adhesion and Autoadhesion of Mictronized Particles to Particulate and Compacted Powder Surfaces" J. of Col. InT. Sci., 187, (2), pp. 484-491.

Polk, R. (1971) Dissertation, Universitat Karlsruhe

REFERENCES

Poppe, T., Blum, J., and Henning, T. (2000) "Analogous Experiments on the Stickiness of Micron-Sized Preplanetary Dust" Astrophysical Journal, 533, (1), pp. 454-471.

Qi, Q. and Brereton, G.J. (1995) "Mechanisms of Removal of Mictron-Sized Particles by High-Frequency Ultrasonic-Waves" IEEE Transactions on Ultrasonics Ferroelectrics and Frequency Control, 42, (4), pp. 619-629.

Rabinovich, et al. (2000) "Adhesion between Nanoscale Rough Surfaces" J. Colloid Int. Sci., No. 232, pp. 10-16

Ratke, L., Kochan H., and Thomas H. (1991) "Laboratory Studies on Cometary Crust Formation: The Importance of Sintering". LPI Conference, Asteroids, Comets, Meterors, Houston, TX, pp. 497-500

Rimai, D.S. and Busnaina, A.A. (1995) "The Adhesion and Removal of Particles from Surfaces" Particulate Science and Technology, Vol. 13, pp. 249-270.

Roessler, K., et al. (1990) "A Model Comet Made from Mineral Dust and H2O-CO2 Ice: Sample Preparation Development" LPI Conference, 20th Lunar and Planetary Science Conference Proceedings, pp 379-388

Rudzinski, W. and Everett, D.H. (1992) *Adsorption of Gases on Heterogeneous Surfaces*, Academic Press, London

Seidensticker, K. J., and Kochan, H. (1992) "Experiments with cometary analogues at the DLR" Annales Geophysicae 10, pp. 198-205

Sentman, D.D. (1991) "Electrostatic Fields in a Dusty Martian Environment" Sand and Dust on Mars, NASA Conference Publication CP-10074, p. 53

Shao, Y.P., and Lu, H. (2000) "A Simple Experression for Wind Erosion Threshold Friction Velocity" Journal of Geophysical Research-Atmospheres, Vol. 105, No. D17, pp. 22437-22443.

Sickafoose, A.A., et al. (2000) "Experimental Investigations on Photoelectric and Triboelectric Charging of Dust" Journal of Geophysical Research, Space Physics (to be published)

Smith, H. I., and Gussenhoven, M. S. (1965) "Adhesion of Polished Quartz Crystals under Ultrahigh Vacuum" J. Appl. Phys., 36, pp. 2326-2327

REFERENCES

Soltani, M. and Ahmadi, G. (1994) "Particle Removal Mechanisms Under Substrate Acceleration" Journal of Adhesion, Vol. 44, (3), pp. 161-175.

Stetson (1999) Office of Space Science, Roadmap

Sullivan, R., et al. (2000) "Results of the Imager for Mars Pathfinder Windsock Experiment" Journal of Geophysical Research, Vol. 105, No. E10, pp. 24,547-24,562

Tabor, D. (1977) "Surface Forces and Surface Interactions" Journal of Colloid and Interface Science, Vol. 58, No. 1, p. 2

Thiel, K., et al. (1990) "Crustal Evolution and Dust Emission of Artificial Cometary Nuclei" LPI Conference, 20th Lunar and Planetary Science Conference Proceedings, Houston, TX, pp. 389-399

Tse-San, C. (1963) Vesn. Mosk. Gos. Univ., Ser. 4, Geologiya, No. 2:61

Verwey, E.J. and Overbeek, J.T.G. (1948) *Theory of Stability of Lyophobic Colloids*, Elsevier, Amsterdam

Visser, J. (1976) "Chapter 1, Adhesion of Colloid Particles" Surf. Colloid Sci., No. 8, pp. 3-79

Wall, S., et al. (1989) Particles on Surfaces 2: Detection, Adhesion, and Removal, K.L. Mittal, Ed., Plenum Press, New York

Warren, S.G. (1984) "Optical Constants of Ice from the Ultraviolet to the Microwave". Applied Optics, Vol. 23, No. 8, pp. 1206-1225

Weissman, P.R. (1986) "Are Cometary Nuclei Primordial Rubble Piles?" Nature, No. 320, pp. 242-244

Weissman, P.R. (1996) "If It Quacks Like a Comet..." Icarus, Vol. 121, Article No. 0085, pp. 275-280

REFERENCES

Whipple, F.L. (1950) "A Comet Model I. The Acceleration of Comet Encke" Astrophys. J., No. 111, pp. 375-394

Williams, R. and Nosker, R.W. (1988) "Strong Adhesion of Dust Particles" Particles on Surfaces 1, Detection, Adhesion, and Removal, K.L. Mittal, Ed., Plenum Press, New York

Wintercorn (1910) reference in Johnson and Grenier

Yong, R.N. and Warkentin, B.P. (1966) *Introduction to Soil Behavior*, Wiley, New York

Zimon, A.D. (1969) *Adhesion of Dust and Powder*, Plenum Press, New York.

Ziskind, G., Fichman, M., and Gutfinger, C. (1997) "Adhesion Moment Model for Estimating Particle Detachment from a Surface" Journal of Aerosol Science, Vol. 28, No. 4, pp. 623-634

APP. I SCHEMATICS OF EXPERIMENTAL APPARATUS

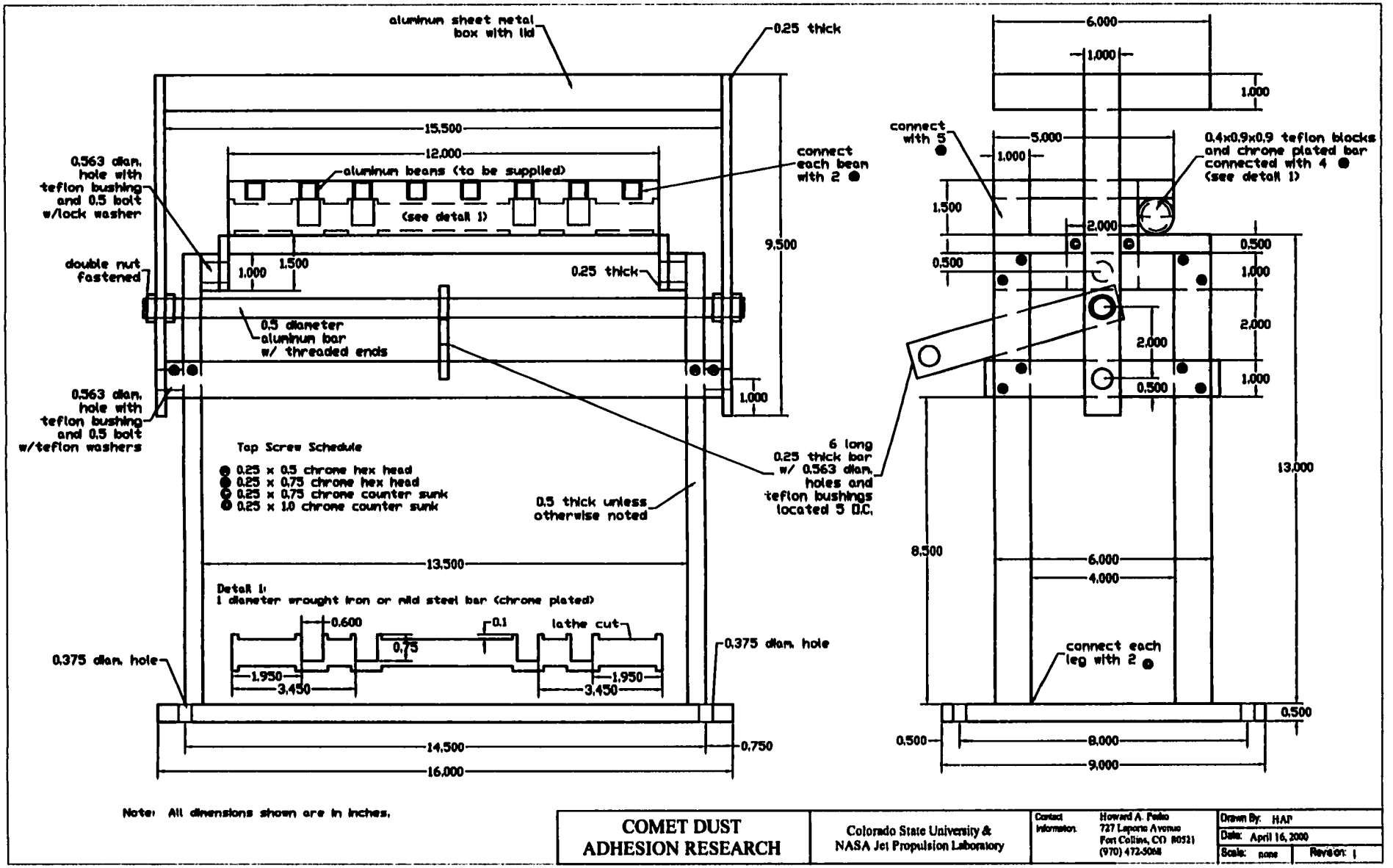

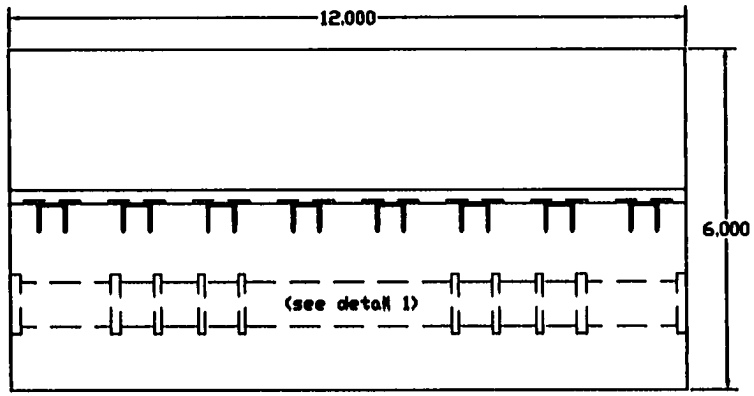

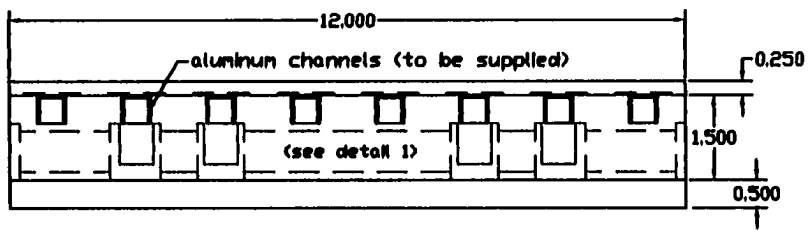

Note: All dimensions are inches.

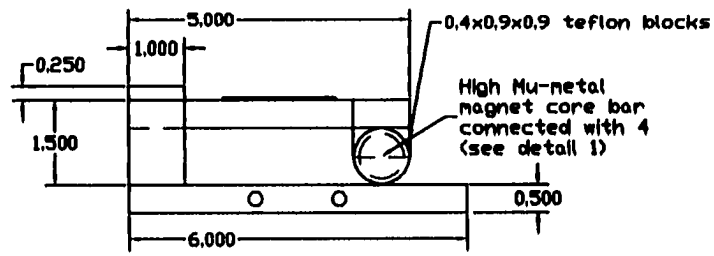

Note: All dimensions are inches.

Detail 1:
1 diameter High Mu-Metal magnet core

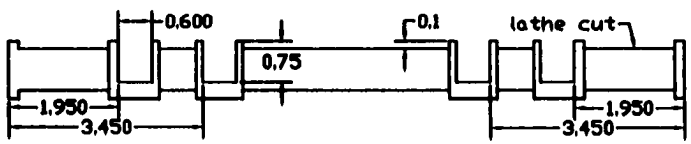

Note: All dimensions shown are in inches.

COMET DUST ADHESION RESEARCH	Colorado State University & NASA Jet Propulsion Laboratory	Contact Information	Howard A. Pasko 727 Laporte Avenue Fort Collins, CO 80521 (970) 472-3068	Drawn By: HAP Date: April 14, 2000 Scale: none Revision: 3

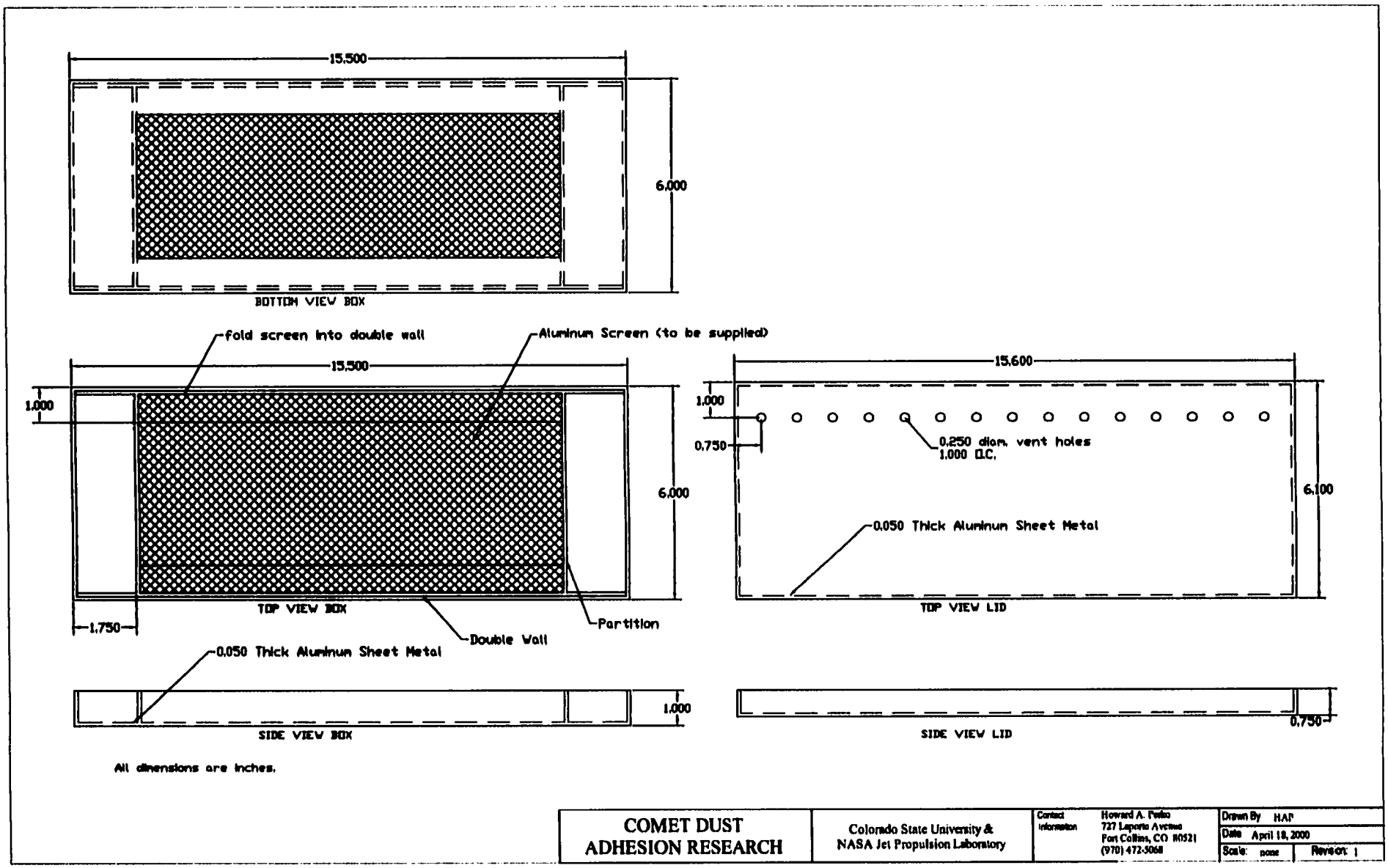

APP. II WIRING DIAGRAMS FOR EXPERIMENTAL APPARATUS

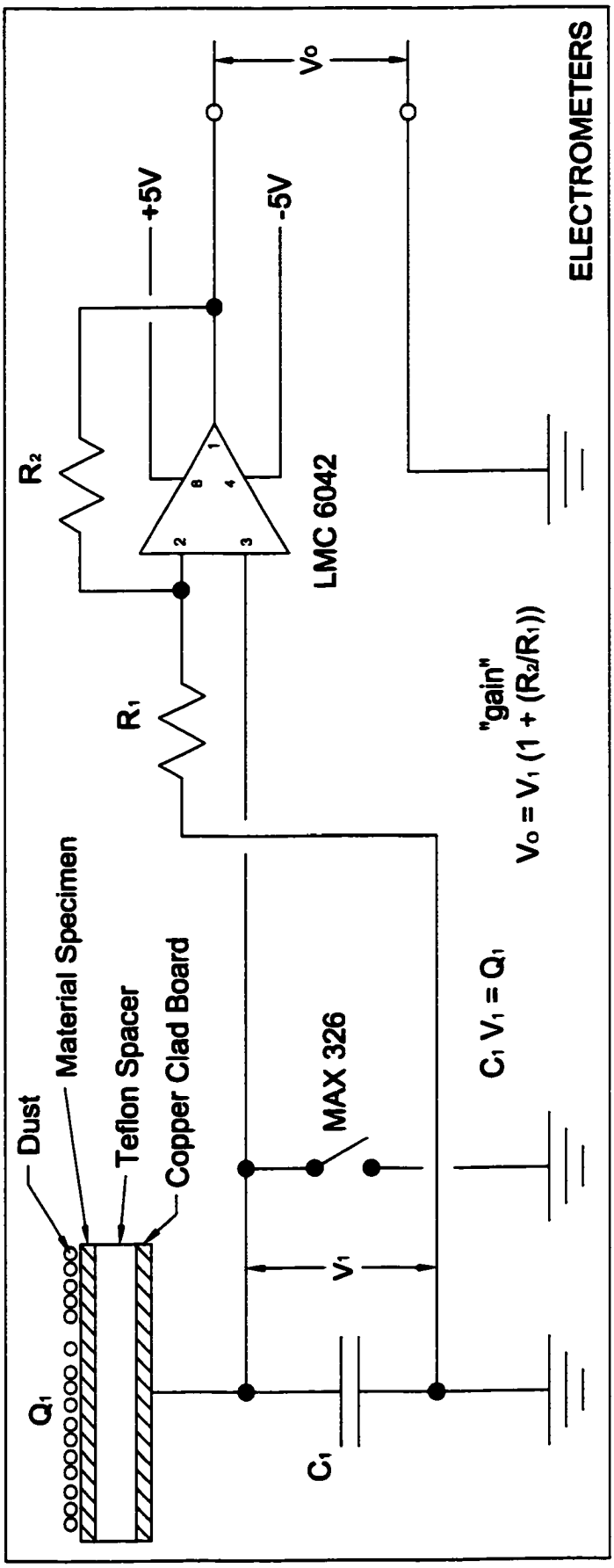

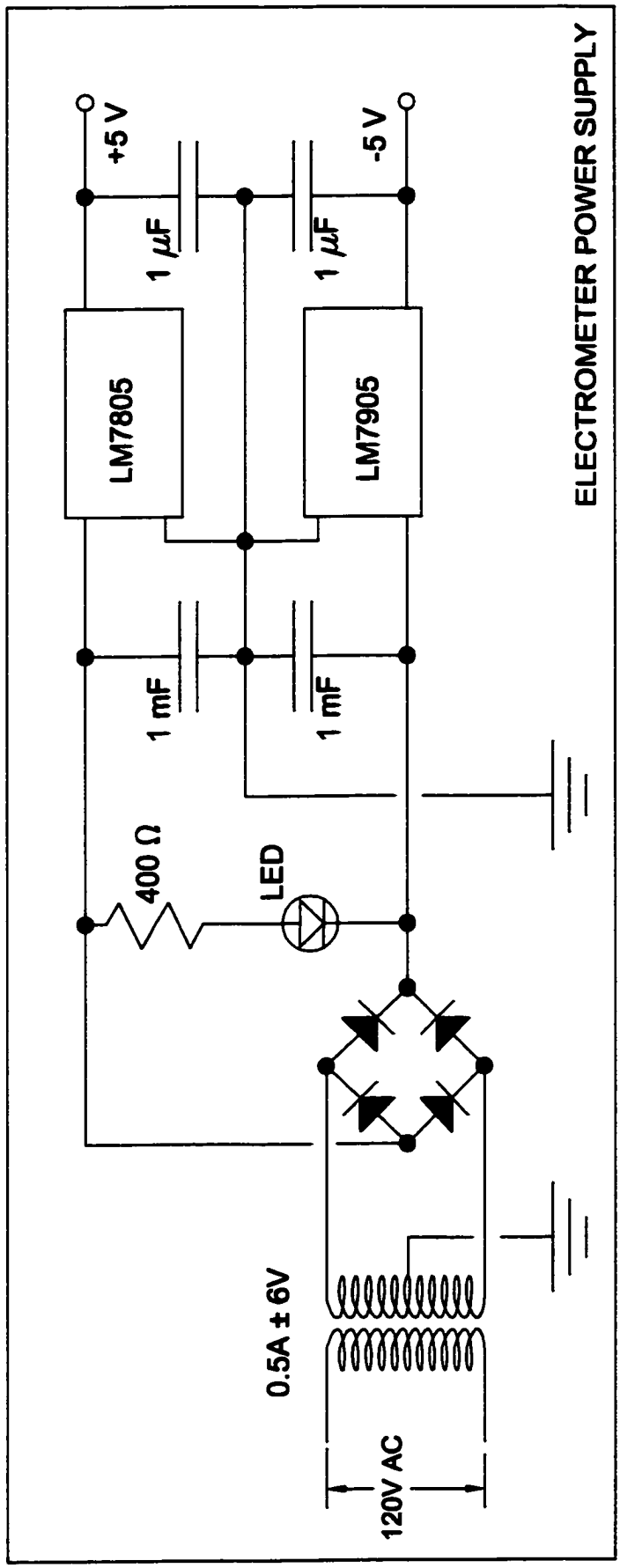

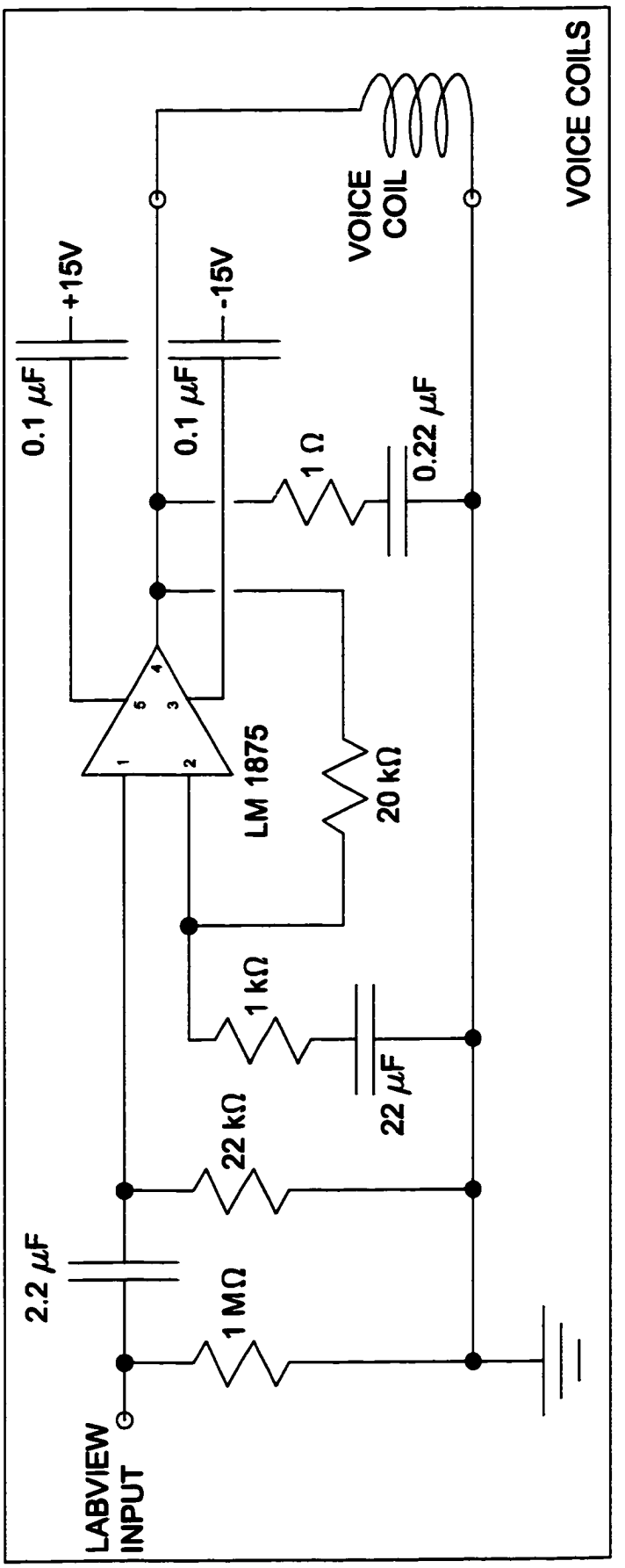

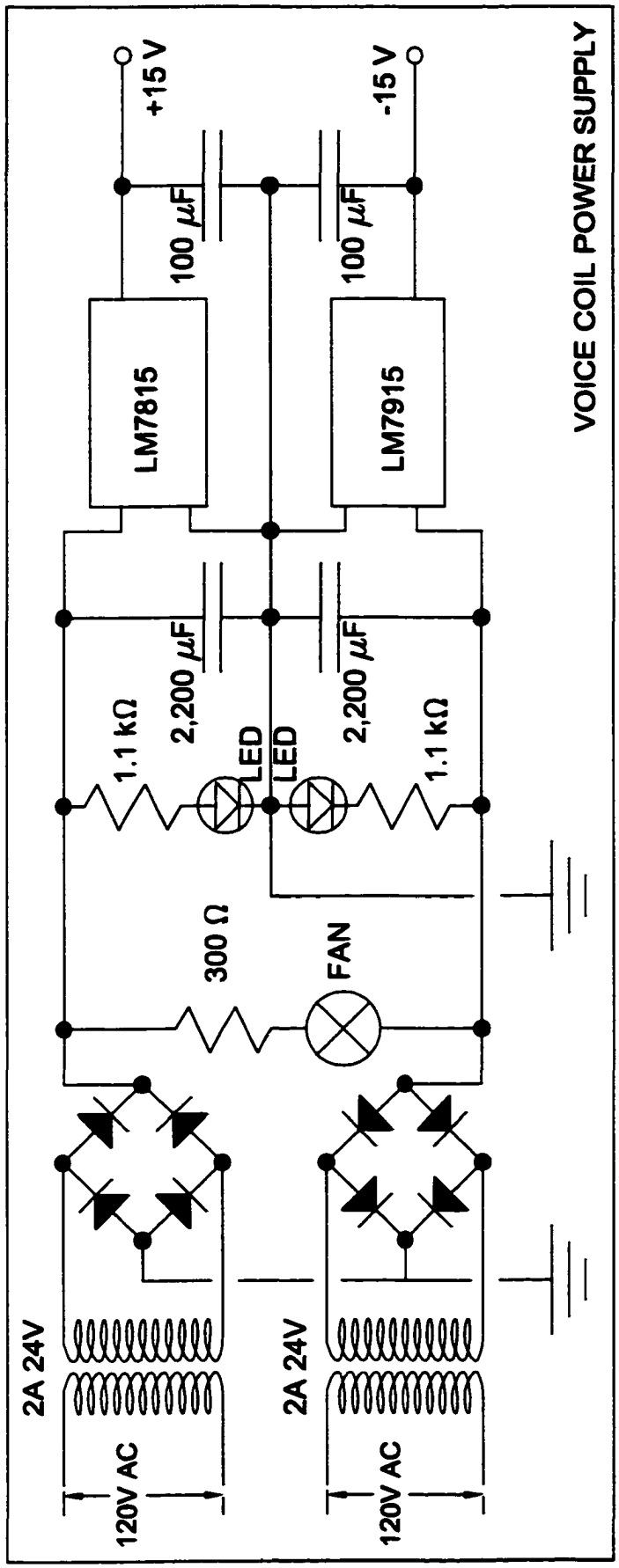

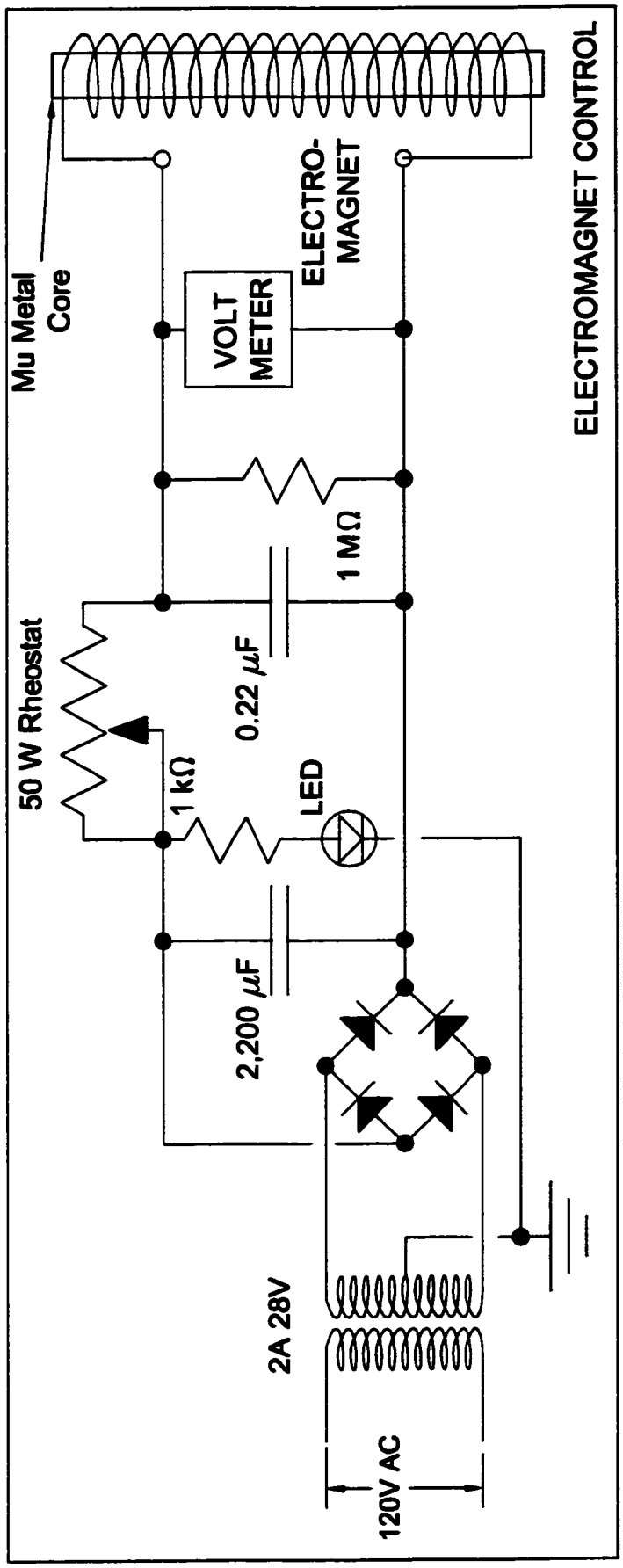

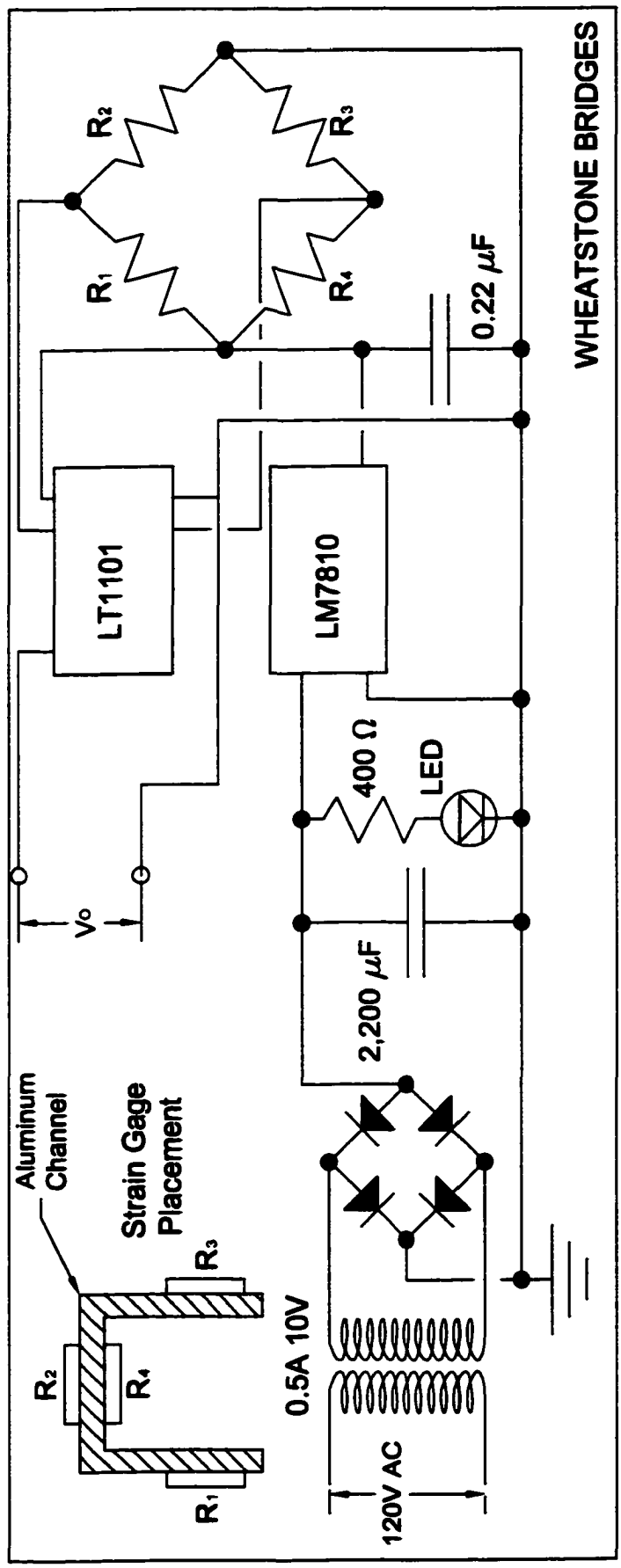

APP. III LABVIEW EXPERIMENT CONTROL PROGRAMS

ExperimentS.vi
C:\Howie\Space Research\doctors\Laboratory\ExperimentS.vi
Last modified on 3/20/01 at 10:14 PM
Printed on 4/2/02 at 4:42 PM

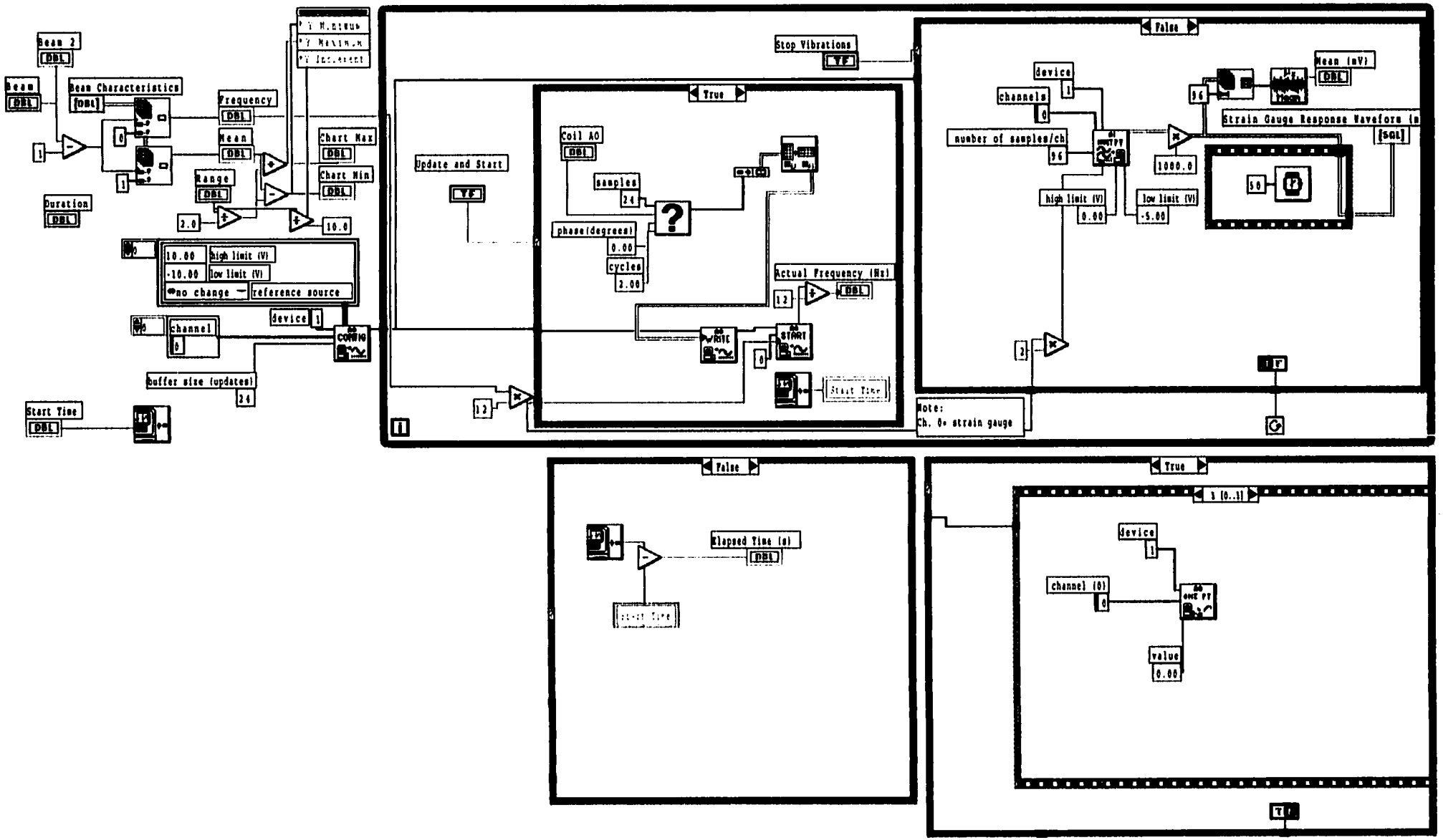

findresonant.VI
C:\Howie\Space Research\doctors\Laboratory\findresonant.VI
Last modified on 2/19/01 at 9:04 PM
Printed on 4/2/02 at 4:31 PM

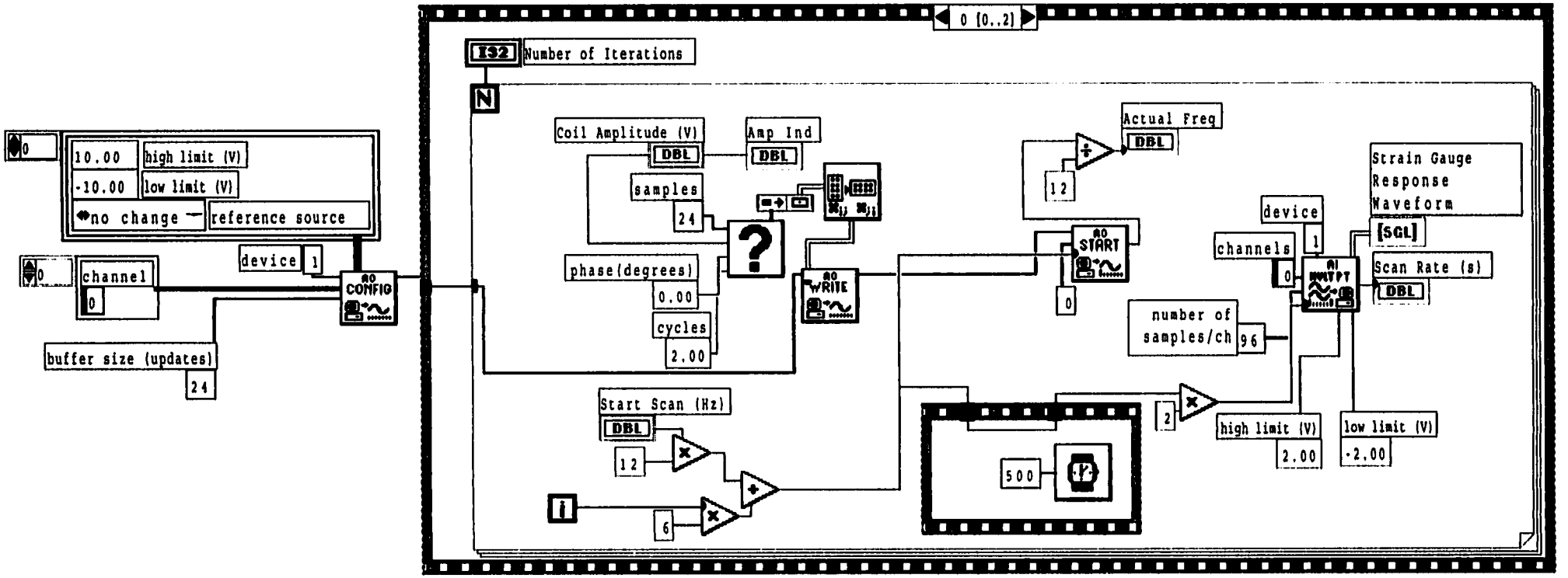

APP. IV VIBRATING CANTILEVER BEAM ANALYSIS AND CALIBRATION

Beam Deflections

The first mode of vibration of the cantilever beams in the experiment was modeled using the formula for simple bending given by

$$D = \frac{F}{6EI}(-j^3 + 3l^2j - 2l^3)$$

where j is the distance from the free end of the beam, D is deflection at point j, l is the length of the beam, E is the Modulus of Elasticity, F is the force applied to the end of the beam, and I is the area moment of inertia. The value of the first term in the above equation can be set equal to a constant, β_n, that depends on the elastic properties and shape of a given beam n times the voltage measured due to strain in the Wheatstone bridge, V_n, as given by

$$\beta_n V_n = \frac{F}{6EI}$$

Hence, an equation that models the amplitude of vibrations of a cantilever beam is given by

$$D = \beta_n V_n (-j^3 + 3l^2j - 2l^3)$$

This is the equation that was presented in Chapter 6.

The value of the parameter β_n was determined by calibrating each beam. The procedures for beam calibration consisted of mounting a digital displacement dial gage at an arbitrary distance j from the end of the beam. Measured displacement, D, at the dial gage position was plotted against the measured voltage across the Wheatstone bridge, as shown in the following figure. As can be seen in the figure, the deflection was approximately linear with respect to the voltage. The parameter βn was computed for each beam by multiplying

the slope of a linear regression line for the calibration data times the expression, $-j^3 + 3l^2j - 2l^3$. The variation in β_n used for computation of the error introduced by this method of calibration was found by taking the standard deviation of the calibration data.